12-17-2015

Mass Transport through Conical Nanopipettes and its Applications in Energy Conversion and Crystallization

Yan Li

MASS TRANSPORT THROUGH CONICAL NANOPIPETTES AND ITS APPLICATIONS IN ENERGY CONVERSION AND CRYSTALLIZATION

by

YAN LI

Under the Direction of Dr. Gangli Wang (PhD)

ABSTRACT

With the advancement of current nanotechnology and deeper understanding of mass transport through single solid state nanopores, more applications of nanopores are emerging have been inspired and brought up by biological nanopore. Steady state response has been widely studied and explored. However, dynamic ionic response has seldom been explored. Our group has studied ionic transport kinetics and reported unique time dependent ionic transport behavior through bench-top fabricated single glass nanopores. Compared to other solid state nanopore compartments, single nanopipettes have found applications in scanning ion conductance microscopy, controlled small volume delivery and biological imaging, due to their ease to fabricate and special geometry for precise tip spatial control. Other than generally considered radius and half cone angle, long shank geometry in nanopipettes is another parameter to affect ionic transport behaviors compared to other nanopores with shorter shank length. In this dissertation, the first research topic is dynamic ionic transport behaviors through single quartz nanopipettes from fundamental perspective. An important non-zero cross point separating normal and negative hysteresis current-potential (I-V) loops will be introduced and discussed by electroanalytical analysis. Strong time dependent I-V hysteresis at low frequency and interesting negative resistance behavior reveals the impacts of finite variation in nanogeometry specifically channel length effect. Next, dynamic ion transport through single nanopipettes is studied under a series of concentration gradient introduced. Ion transport dynamics through asymmetric nanogeometry contributed by migration and diffusion is deconvoluted and its implication in salinity gradient energy conversion is explained. In the third project, a new method to crystallize matter based on dynamic control of mass transport through single nanopipette is demonstrated using protein insulin.

INDEX WORDS: Nanopipette, Conical asymmetric nanogeometry, Ion transport, Crystallization, Salinity gradient energy harvesting, Energy conversion, Dynamic control, Mass transport, Memory effect

MASS TRANSPORT THROUGH CONICAL NANOPIPETTES AND ITS APPLICATIONS IN ENERGY CONVERSION AND CRYSTALLIZATION

by

YAN LI

A Dissertation Submitted in Partial Fulfillment of the Requirements for the Degree of

Doctor of Philosophy

in the College of Arts and Sciences

Georgia State University

2015

MASS TRANSPORT THROUGH CONICAL NANOPIPETTES AND ITS APPLICATIONS IN ENERGY CONVERSION AND CRYSTALLIZATION

by

YAN LI

Committee Chair: Gangli Wang

Committee: Gangli Wang

Ming Luo

Ivaylo Ivanov

Electronic Version Approved:

Office of Graduate Studies

College of Arts and Sciences

Georgia State University

December 2015

DEDICATION

I would like to dedicate this dissertation to my parents. It's their unconditional support and love that makes me who I am today.

ACKNOWLEDGEMENTS

First and most important, I would like to thank my advisor, Dr. Gangli Wang, for all his advices and guidance. His brilliant ideas always inspire me and guide me through the dark. He is very smart, hardworking and considerate. I have learned a lot from him, especially effective communication, critical scientific thinking and working efficiency.

I would like to thank all my committee members, Dr. Ming Luo, Dr. Ivaylo Ivanov and Dr. Zhen Huang for their valuable time to attend my annual committee meetings, give me very useful advices and help on my project.

I would like to give special thanks to Dr. Ming Luo again for his generous help on crystal growth and handling.

I would like to thank all the lab members for their help and accompany. They are all very nice, professional and considerate. We enjoy science and life together.

Finally, I would like to thank all my friends, especially Shuang Zhang and Dengchao Wang for their accompany through my ph.D life. We share happiness and sorrow together.

TABLE OF CONTENTS

LIST OF TABLES

LIST OF FIGURES

1 INTRODUCTION

1.1 Definition of Channel-type Single Nanopores

Nanochannels are generally defined as channels with at least one dimension smaller than 100 nm with either symmetric or asymmetric geometry. When it's down to nanoscale, many interesting ion transport behaviors have been observed due to large surface volume ratio, when the channel dimension approaches Debye length dimension and resulting partial overlapping of electric double layer. Those unique and interesting ion transport behaviors have found many applications in DNA sequencing, stochastic sensing, controlled delivery, energy harvesting and storage and other biological and energy related areas. Compared to biological nanopores/nanochannels, solid state nanochannels and nanopores show more advantages in thermal stability, versatile fabrication strategy, flexibility for geometry design and variation, mass production and robustness for repeated and broader usage.

Among all versatile nanochannel fabrication methods, nanolithography serves as a very important indispensable method. It is mainly composed of lithography techniques with nanometer resolution and overcomes the limitation of low resolution of traditional photolithography induced by hundreds nanometers incident light wavelength. Electron beam lithography and focused ion beam are two techniques that can be used directly for channel writing and fabrication. Electron beam lithography uses a focused electron beam on electron beam sensitive resists film followed by selectively removal of either exposed or unexposed resist to fabricate nanochannels.[1] Compared to electron beam lithography, focused ion beam lithography directly shoots focused ion beam on hard substrates,

including silicon nitride,[2,3] silicon dioxide,[4] silicon,[4] PDMS[4] without extra need for photoresist. Ion track etching is another useful way to fabricate single channel nanopore on polymer membranes. The polymer membranes, mainly including polyethylene terephthalate,[5,6] polyimide[7,8] and polycarbonate,[9] are bombarded with high energy swift heavy ions to form a cylindrical nanopore, or an ion track across the membrane. Asymmetric etching methods can be adopted afterwards to obtain asymmetric geometries.

Nanopores and nanopipettes in glass/quartz SiO_2 membranes are attracting more and more attention due to their ease to fabricate and cost effectiveness. Glass nanopores are conical pores with nanometer opening embedded in thin glass membrane through which the two solution reservoirs are connected. The bench-top fabrication process was published by Bo. et al.[10] Generally, the electrochemically sharpened Pt or Au tips were imbedded inside a lead glass capillary and further polishing and removal of embedded metals can give a nanopore with radius as small as 10 nm embedded in 20~75 um thickness glass membrane.

Nanopipettes are needle-like pipettes with nanometer opening, normally range from 0~100 nm. In this dissertation, single quartz nanopipettes are used due to their ease of fabrication. Two quartz nanopipettes can be fabricated in seconds at the same time by CO_2 laser heat puller. The nanopipette opening and geometry can be programmed by adjusting five parameters: Heat, Filament, Velocity, Del, Pull. The nanopipette is composed of a taper shank and a long stem. Note that due to special geometry of nanopipette, ions diffusion at nanopipette tip can be radial diffusion outside of the nanopipette tip and also linear diffusion inside the stem. The sturdy long stem,

programmable geometry and thin tip wall (~ 20 nm) make it easy for nanopipette to realize precise tip spatial control.

1.2 Ion Transport Behaviors

1.2.1 Surface Charge Effect

The solution-substrate interface will have significant effects on the ionic transport behaviors through nanopores due to electrostatic interactions. Ions of different valence and charge polarity will be affected differently during their transport through these nanopores. It is therefore important to understand the surface charges for the long range electrostatics in addition to nanogeometry that impose spatial confinements. When the solid state substrate is placed in aqueous solution, the deprotonation of surface functional groups will result in negatively charged substrate. Qualitatively, both polarity and density of nanopore surface charge can be modified by chemicals with different functional groups or changing solution pH.[11] However, to quantitatively characterize the surface charge density at the nanopore orifice is very challenging experimentally, especially the technical difficulty down to nanoscale. In a combined experimental and simulation approach, by solving Poisson and Nernst-Planck equation to fit the measured i-V curves in simulation, our group is able to noninvasively quantify the steady state flux distribution inside the nanopore and the surface charge density of individual nanopores[12-14]. Unlike the common perception of stochastic/uniform surface charge density, our fitting suggested a non-uniform surface charge gradient at the single nanopore orifice.

1.2.2 Electrokinetic Process

When a substrate is immersed in a solution, electric double layer forms. This double layer is composed of a stern layer due to chemical absorption of counter ions on the surface and a diffuse layer. The thickness of double layer is characterized by Debye length, $\lambda_D \sim 1/\sqrt{C_i}$, here C_i represents the solution concentration. From this equation we can see, when the solution concentration is infinitely high, Debye length will be equal to zero. When the solution is very much diluted, this length will be infinite long. For example, the Debye length at the solution substrate interface is around 10 nm for glass substrate in 1 mM KCl solution.[15] Note that this number is in proximity to nanochannel's size in nanometer range and the double layer will partially overlap at the smallest dimension and affect ion transport behaviors. Two most dominant electrokinetic processes of ionic transport through single channel type nanodevice, electroosmotic flow and electrophoresis, are relevant to this substrate solution double layer.

Electroosmotic flow (EOF) is the movement of fluids under applied potential due to the interaction between the applied electric field and surface charge. It is caused due to the surface mobile layer dragged by surface charge counter ion along the electric field direction. Generally, EOF velocity is dependent on the electric field applied. In microchannels the EOF is plug like while in nanochannel it shows parabolic like behavior and reduces the flow speed at lower salt concentration.[16,17] Electrophoresis is the movement of charges under applied potential. The movement of ions is dependent on the mobility of ions, mainly including charges and hydrodynamic volume. EOF direction, shape of electric double layer and valences will also have effects on the ions' movement in nanochannel.[18] When there is a pressure gradient, another electrokinetic process-streaming potential, the resulting potential from the movement of fluid through nanopore, will occur. It is neglected here since in my dissertation no external pressure is applied.

1.2.3 Ion Current Rectification

One interesting phenomenon observed for ion transport through nanopores is ion current rectification behavior (ICR). Ion current rectification is the deviation of the current-voltage response from linear ohmic behavior, or experimentally the current at one potential polarity is higher than the opposite potential polarity. ICR ratio is a quantitative characterization of this behavior with the current at one potential polarity over the current at the opposite with same magnitude, often at 1 V. This behavior was first observed and reported by Wei and Bard using quartz nanopipettes and was demonstrated to be related to the ionic concentration, pore size and surface charge.[19] As we know, taking conical glass nanopore as an example, the signal limiting region will be inside the conical close to the nanoorifice and the silanol group at nanopore surface will deprotonate in water and

have negative surface charges at ambient pH. Due to the long range electrostatics, or partial overlapping of diffusive layer at small nanopore orifice, the nanopore will show permselectivity and the cation will be selectively transported. If the working electrode is outside in the bulk and a reference is place inside the conical nanopore, cations in the bulk solution will migrate toward inside of the conical nanopore while anions from the base side will migrate toward the nanopore. Note the surface electric field will oppose the movement toward opposite directions. Consequently, both cations and anions will be enriched at the signal limiting region right inside the nanopore orifice, while cation concentration and flux is significantly higher near the substrate interface. A larger current will be observed. A smaller current will be observed if a negative potential was applied due to the reduction of ion concentration as charge carriers in the signal limiting region. When the ionic concentration increases, the ionic screening effect is more significant that will reduce the surface charge effect and the current rectification ratio decreases. When the nanopipette orifice increases, the ICR ratio decreases due to the decrease of diffusive layer overlapping and resulting surface charge effect. When the surface charge decreases, the ICR ratio will decrease. When the surface charge is zero, there is no ICR. When the surface charge changes polarity, the ICR will reverse direction as well, as shown in Fig. 1-1. This ICR behavior is often observed in asymmetric nanopore with uniform surface charge distribution or symmetric nanopore with asymmetric surface charge distribution. Other than the surface charge, pore orifice and concentration effect, introduction of extra concentration gradient across the nanopore[20,21] or approaching external charged surface[15,21] can cause ICR change as well.

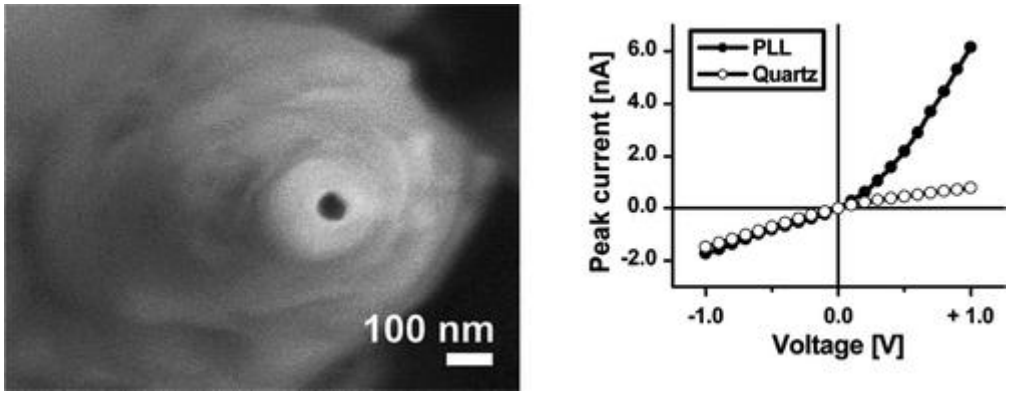

Fig. 1-1 A) Top-view SEM of a nanopipette tip. B) Ion current rectifications in bare negative glass and with positive charged poly-L-lysine coating. Note that the ICR reverses direction and ICR ratio increases with PLL coating. Graph is adapted from reference.[11]

1.2.4 Memory Effects

Memory effect, or history dependent effect, is the dependence of ionic transport behaviors on the previous condition due to finite mobility of ions to redistribute at the nanopore signal limiting orifice under applied bias. Most of recent ionic transport studies focus on steady state responses. Our group studied the dynamic behaviors limited by of ionic transport kinetics through glass nanopore.[22-24] The IT dynamics reflect interesting memristive and memcapacitive effects. Unlike a normal I-V curve that displays overlapped forward and backward current at steady state, at higher scan rates, a fixed cross point was found in the pinched current potential curves of the ion transport through nanopore that separates the normal and negative hysteresis loops at different scan rates, as shown in Fig. 1-2. The quantitative correlation of this cross point potential with ionic concentration was established.[23] The cross point is proposed as a characteristics of each single conical nanopores and represents an effective surface potential across the nanopore. If the scan rate increases to a large extent, this cross point could shift toward

higher bias magnitudes due to the superimposed charging current from charging and discharging behavior of the exterior surfaces of nanopore glass substrate.[24] The IT dynamics is supported by a steady fixed cross point at different scan rates after subtraction of simulated capacitive components at each scan rate based on back calculated RC value. The impedance study of ion transport through single glass nanopore at different fixed DC potentials with different frequencies of AC perturbations indicate at high conductivity end an inductive behavior shows up at low frequencies, at low conductivity end a normal capacitor behavior shows up while these behaviors are separated by a pure resistor behavior at cross point potential, as shown in Fig.1-2 (B).[22,23]

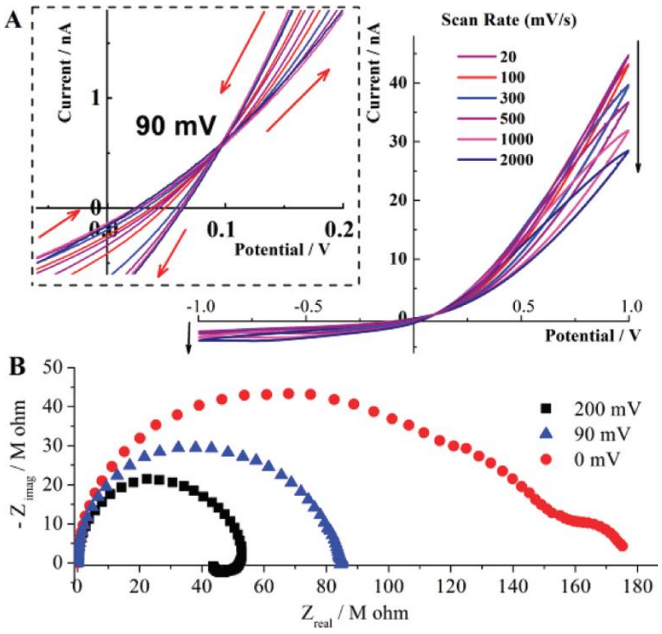

Fig. 1-2 (A) Overlaid i−V curves at different scan rates in 10 mM KCl. Cross-point potential remains at 90 mV at all scan rates. Black arrows next to the curves indicate changes in current with increase of scan rate. Red arrows in the inset illustrate direction of potential scan. (B) Impedance spectra taken above, below, and at the cross-point potential. Graph is adapted from the reference.[23]

1.3 Applications

Channel-type single nanopores have found many applications in bioanalytical chemistry areas, including DNA sensing and sequencing,[25-27] protein transport and property study,[28-30] stochastic sensing,[31] single molecule detection,[32] salinity energy conversion.[7] Here we mainly focus on the application of nanopipettes. In general, the surface of nanopipettes can be functionalized by electrostatic absorption, physical deposition or silanization. For instance, Schrlau and coworkers have introduced a method to coat the interior of a nanopipette with a layer of carbon, resulting in a ‘‘carbon nanopipette’’ (CNP), and this method has been widely used since the inner wall properties of nanopipette can be controlled by extra external applied potential on the deposited carbon layer and its flexibility to serve as a nanoelectrode to detect oxidation/reduction current as well as ionic current passing through the nanopore.[33] Other than carbon, Xu, X. etc. successfully modified the inner surface of conical glass nanopipette with ultrathin gold film by facile one-step photochemical approach using $HAuCl_4$ and ethanol as common reagents with the aid of UV irradiation.[34]

1.3.1 Nanoreactor

Due to their confined opening at nanometer range and ease to control tip position, nanopipette can serve as a perfect nanoreactor. For example, nanopipette can be used to fabricate freestanding conducting polymer nanowires. Basically the nanopipette is backfilled with monomer solution and retracted at a certain speed under control. When the monomers are exposed to air, they will be oxidized and form patterned polymer nanowire.[35] Dynamic control of nanoprecipitation can also be achieved by filling nanopipette barrel with zinc phosphate solution and the counter-ion that has low

solubility with zinc in the bulk. After application of potential, nanopipette serves as a nanoreactor. Zinc and counter ions meet, precipitate and form transient blockage.[36] Due to the ease of spatial tip control and good compatibility with microscope technique, nanopipette and surface enhanced Raman spectroscopy immunoassay has been integrated for the plasmonic detection of IgG.[37]

1.3.2 Controlled Small Volume Dispensing

Long sturdy quartz stem, conical shank with ~20 nm wall thickness and needle-like geometry make it very easy to control the precise nanopipette tip position in specific small substrate like single cell for controlled small volume dispensing, either by electric field or pressure. Laforge, F. O. et al. developed an attosyringe by filling a nanopipette with water immiscible organic solvent under applied potentials to withdraw or dispense attoliter to picoliter aqueous solution. Since electric field across the liquid/liquid interface changes the surface tension, the resulting force will be strong enough to withdraw or dispense aqueous solution. This attosyringe also successfully penetrated into single cells for controlled buffer delivery.[38] Adam Seger, R. et al. developed another single-cell injection platform based on double-barrel nanopipettes that uses scanning microscopy techniques to detect cell surfaces. They successfully adopted voltage pulses with different potential polarity to controllably deliver different charged fluorescent dye molecules in two barrels to individual cells with only one simple penetration while maintain high cell viability at the same time.[39] For pressure drive small volume dispensing. Saha-Shah etc. creatively utilized nanopipette for nanoliter volume pressure-driven dispensing and combine it with matrix-assisted laser desorption ionization-mass spectroscopy to collect and analyze sample from single Allium cepa cells and live Drosophila.[40]

1.3.3 Rectification Sensor

Since the ionic transport behavior is highly affected by the nanopipette surface charge, this character has been widely used for label-free biosensing, not only qualitatively but also quantitatively. Vilozny, B. et al. successfully immobilized the nanopipette tip surface with reversible cation-response calmodulin by using polyelectrolyte's multivalent electrostatic binding to the charged glass surface first and then amide reacts to bind protein. The tip surface charge will change due to the protein capturing divalent metal ions and has direct effect on the ionic current magnitude. They quantitatively calculated the binding affinity of calcium ions and found that it agreed well with reported value of solution protein.[41] Sa, N. et al modified the quartz nanopipette with imidazole functionalized silane and test the ionic current rectification ratios at different pHs. They found that at ambient pH the imidazole will bind to divalent cobalt ions while at low pH protons will replace divalent cobalt ions and regenerate the binding site. They suggested that reversible responses can be attained while choosing recognition elements with intermediate binding affinities.[42] Tiwari, P. B. et al used the change of surface charge effect to quantitatively study the protein-protein interactions.[43] They modified the nanopipette inner surface with negatively charged protein human neuroglobin and then immersed this nanopipette in a series concentration of positively charged cytochrome C solutions. Interaction of cytochrome c and human neuroglobin will result in the change of surface charge, which provides a quantitative way derive equilibrium dissociation constant of Cyt c-hNgb complex formation that matched well with the surface plasmon resonance measurements.

1.3.4 Resistive-pulse control /coulter counter sensor

Coulter counter sensor, or resistive-pulse control sensor, is a way for counting and sizing of particles in a solution by electrical resistance change when these particles pass through a channel.[44] For a lot of biological molecules and other macromolecules, the molecule size is similar to the nanopore opening and the transport of those charged macromolecule will cause electrical resistance change. For example, ionic transport behaviors of single DNA attached to 10 nm nanoparticles were observed by Karhanek, M. et al.[24,45] Three different states, baseline state, the oligo-tail blockage sublevels and nanoparticle head blockage levels were observed and analyzed. Fu, Y. et al. developed a DNA sensor based on dendrimer modified nanopipette. The hybridization of a specific DNA sequence was detected due to different extent of ionic current rectification[46]. Single nanoparticles can be controlled to deliver from a nanopipette by employing resistive pulse sensing approaches shown by Michael Mirkin's group.[47] Ivanov, A. P. et al demonstrated nanopipette based asymmetric pulses voltage control for label-free detection and precise delivery control of single DNA molecules.[48]

1.3.5 Scanning Ion Conductance Microscopy

Nanopipette serves as a good probe for scanning ion conductance microscopy (SICM) due to its sharp tip geometry to realize precise tip spatial control. When the nanopipette is backfilled with solution electrolyte and tip is scanned close to the substrate, due to the accessible ions blocked by the external substrate, the ionic current through the nanopipette will be smaller. Based on this, the distance between the nanopipette and the substrate can be estimated and the biological imaging can be realized.[49] Note that in SICM, to minimize the nanotip surface effect, high ionic concentrations are adopted.

1.3.6 Surface charge mapping

Slightly different from typical SICM, if the nanopipette tip diffuse layer partially overlapped in low ionic concentration, the further overlapping of the surface tip diffuse layer with the external substrate surface charge introduced diffuse layer will change the ion current rectification.[21] Based on this, simultaneous surface charge mapping and biographical mapping has been successfully developed.[50]

1.3.7 New Applications Development

Other than these widely studied applications, new applications are being developed based on nanopipette's interesting geometry and ion transport behavior through it. For example, Zhou, M. etc. developed a new nanoelectrochemical method by adopting nanopipette to detect charged short-lived intermediates of electrocatalytic oxygen reduction.[51] Basically a nanopipette is backfilled with external aqueous solution immiscible organic phase and scanned over Pt substrate. Generation rate and lifetime of short life intermediate superoxide was detected. Li, T. et al also used the ionic conductivity change of light-tuned complex of charge carriers to fabricate bio-inspired ionic switch based on nanopipettes.[52] UV-vis reversible tunable of spiropyran and Zinc ions complexion will result in reversal current change as ionic switch.

2 DYNAMIC ION TRANSPORT BEHAVIORS THROUGH SINGLE QUARTZ NANOPIPETTES

Nanopipettes have found many applications in bioanalytical chemistry and other related areas for spatially resolved measurements or controlled delivery. Compared to other channel-type single nanopores, its fabrication is simple and cost effective. Even though ionic transport through nanopipette displays typical transport behaviors through single channel-type nanopores such as ion current rectification, and those ionic transport properties through different nanopore platforms have been widely used in many applications, quantitative correlation between the transport phenomena and nanogeometry/nanosurface parameters has not been established. The dynamics of ionic transport through single quartz nanopipette is still needed for better applications. Here dynamic ionic transport behaviors through nanopipettes are studied by different electrochemical techniques at different time scales. First we report much stronger memory effect in nanopipettes resulted from its nanochannel geometry compared to the conical nanopores in our earlier report. A diffusional transport signature is resolved at low frequency range in impedance spectra. The difference from conical nanopores is postulated to the finite differences in nanochannel geometry. Further analysis of the charges in the dynamic redistribution at different scan rates was also conducted with either asymmetric concentration gradients or asymmetric end potential ranges. The charges in i-v hysteresis are correlated quantitatively with both durations and cross point potentials. The corresponding physical pictures were discussed from mechanistic perspectives.

2.1 Introduction

Nanofluidic devices have found many applications in broad areas, including water desalination,[53] energy conversion,[7] single molecule/particle sensing,[32,47] DNA sequencing etc. [25-27,54] Among a variety of nanodevices, quartz or glass pipettes with a nanosized tip are attractive due to their ease to fabricate and cost effectiveness. Many applications have been developed based on nanopipettes including serving as local sample probes[40,50,51,55] and single cell surgery.[49,56,57] A unique merit is the ease to realize precise tip location control since they have sharp long needle like geometry and nanometer thickness side wall. Since the first report of ion current rectification behavior by Wei and Bard using nanopipette,[19] many interesting behaviors of steady-state ion transport through nanochannels have been studied.[58] The fundamental understanding of dynamic ion transport behavior remains rarely explored.

Several electroanalytical methods are uniquely suitable to investigate the dynamic ion transport behaviors through nanopipettes. In classic cyclic voltammetry type measurements, electric current is collected when the potential on a working electrode is linearly and cyclically swept within a range at a fixed frequency, i.e. a triangular waveform. Time dependent transport behaviors can be analyzed through the ionic current collected at different scan rates. In addition to the rectified i-v features collected at either constant potential or at very slow potential scan rates, in the i-v curves at different scan rates, pinched i-v loops were observed in glass nanopores by our group.[23] A fixed cross point separating two hysteresis i-v loops was attributed to the surface potential inside the nanopore. In impedance spectroscopy, a selected DC potential is kept constant to

establish steady-state transport while an AC with small amplitudes is applied at systematically varied frequencies. The disturbances in the measured impedance at different AC frequencies reveal both in-phase transport responses, i.e. resistive, and off-phase behaviors such as capacitive or inductive elements. Impedance spectroscopy has been widely employed in studying interfacial phenomena such as biosensors and ion selective membranes. Our group is the first to apply impedance spectroscopy to study nanoscale interfaces inside single nanochannels and reported novel impedance features of ion transport behaviors through single glass nanopores.[22] In high frequency range, a hemi circle as representative Randle circuit response suggests normal resistive-capacitive (RC loop) ion transport behaviors in substrate-solution interfaces. In low frequency range, additional capacitive behavior, another RC loop, was observed at low conductivity states established by the constant DC potential. An intriguing inductive behavior was discovered at high conductivity for the first time. The newly observed transport behaviors, especially the phase shift between the ion current with respect to the applied potential waveform, were explained by the surface electric field inside the nanopores.

Here in this chapter, dynamic ion transport behaviors through single nanopipette were investigated by CV at different scan rates and impedance spectroscopy. Unlike previous studies, asymmetric parameters, including concentration gradients across the nanotip and asymmetric end potential ranges were introduced for the first time. The goal is to superimpose diffusion at bulk level and vary the duration in the transport hysteresis, and thus to quantitate those dynamic ion transport phenomena and ultimately elucidate the physical meanings. The transport dynamics was explained based on the finite ion

mobility with respect to the variation in stimulus, external potential waveform, under the influence of the surface electric field that has a fixed direction but variable strength.

2.2 Experimental Session

Instruments**:**

P-2000 nanopipettes puller, Sutter Instrument s Co.

Quarts Glass, O.D.:1.0mm, I.D.:7.0, 7.5 cm length, Sutter Instruments Co.

Gamry Reference 3000, Gamry Co.Preparation of nanopipettes:

The pulling parameters of the nanopipettes are as follows: Heat: 70, Filament: 4, Velocity: 60, Del: 150, Pull: 120. The nanopipettes were loaded with acetonitrile and centrifuged for 20 min at 4600 rpm, after which the nanopipettes were washed with water. Different concentrations of KCl electrolyte solution were loaded both inside the naopipette and in the bulk.

Two Ag/AgCl wires were used as electrodes. One was immersed inside of the nanopipette and worked as counter electrode while the other one was in the bulk solution and worked as working electrode. All measurements were carried out by Gamry instrument.

2.3 Results and Discussion:

2.3.1 Strong memory effect at low potential scan rates or frequency

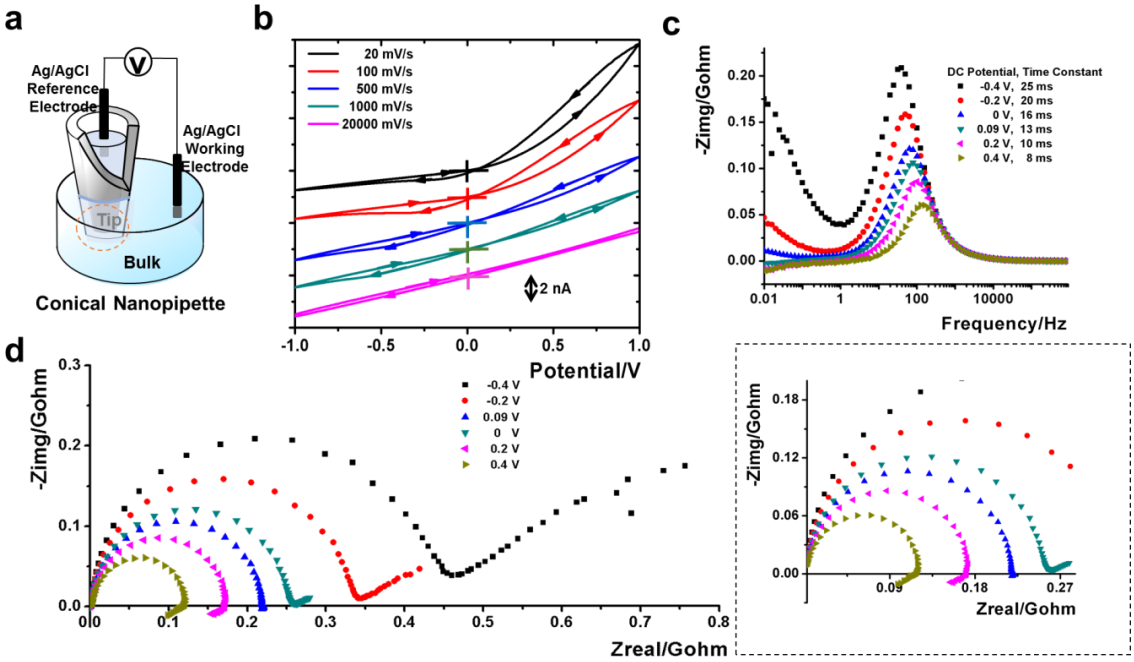

Fig. 2-1 a) Experimental setup with symmetric 50 mM KCl inside a 6 nm nanopipette and in the bulk. b) Overlaid i-v curves of the 6 nm nanopipette with 50 mM KCl at different scan rates. The scale bar is 2 nA. The cross shows the origin of each curve. c) Bode plots and d) Nyquist plots of impedance spectroscopy results. The applied waveform is composed of different DC potentials and an AC with 0.01 V amplitude in the frequency range from 100 kHz to 0.01 Hz. The bottom right (dashed square) shows the zoom-in view of panel d at high conductivity end.

In Fig. 2-1 b, current responses under different potential scan rates of a nanopipette in 50 mM KCl solution were shown. First we observed ionic current rectification behavior, which is the current higher at positive potential compared to the current at negative potentials. This is caused by results from a combination of asymmetric conical tip in nanometer range and the negative surface charges at the tip orifice region originating from deprotonation of silanol groups. Due to electrostatic effect, the nanopipette shows permselectivity towards cations, which are potassium ions in this case.

At positive potentials, cations will accumulate inside the conical tip signal limiting region, which will result in a concentration increase and correspondingly current increase. At negative potentials the nanopipette tip will develop a zone of depletion in mobile ions at the signal limiting region. Both are due to the overlapping of surface and applied electric field. Many simulations and theoretical studies have been performed to explain this phenomenon under steady-state.[11,15,19,59,60] Steady state is the state under which the system is fully stabilized or the changes in the response being measured are negligible or insignificant. A new phenomenon, besides ionic current rectification behavior, is that at low scan rates, a fixed cross point separating two hysteresis loops was found. Forward scan, defined as the potential scanned away from the cross point, doesn't overlap with backward scan, which is defined as the potential scanned towards the cross point. In negative potential range, or at low conductivity side from the cross point, normal capacitive behavior is observed. In other word, the forward current is more negative (i.e. larger) than the backward current. The feature is consistent at different scan rates and better seen in the bottom curve. At high conductivity side, negative capacitive behavior, which means the forward current is lower than the backward current, is observed at lower scan rates. At higher scan rates, rectification decreases as previously reported. The hysteresis effect, or the negative capacitive loop, decreases and transform into normal capacitive behaviors gradually (bottom curve). A non-zero cross point and the pinched i-v hysteresis were first observed in conical glass nanopore but at higher scan rates by our group and explained to be due to the finite mobility of ions to redistribute at the nanopore orifice.[23,24] The results here indicate strong memory or history dependent effects in nanopipettes. In glass nanopores, the overlapping of forward and backward current

curves means that ions has been fully redistributed before reaching next potential, while for nanopipette, even a rate of 20 mV/s is not slow enough for ions to fully redistribute before reaching next potential.

2.3.1.1 Impedance spectroscopy of the nanopipette with symmetric concentration gradient

The Nyquist plots in Fig. 2-1 further demonstrate the finite redistribution of ions under a small AC perturbation at varied frequency. First we observed a hemi circle as a typical Randle circuit response at high frequency in both high conductivity and low conductivity DC potentials. The time constants for the Randle circuit under each specific condition were listed in Fig. 2-1 c. At low frequencies, with DC potential at or very close to the cross point potential, no secondary feature showed up, as shown at 0.09 V. This is due to the cancellation of surface effective potential with applied DC potential. At DC potentials higher or lower than cross point potential, a diagonal line with a non 45 degree phase shift showed up. As a reminder, a 45 degree phase shift is Warburg diffusion element. The results indicate that diffusional component starts to play an important role in ionic transport through nanopipette at low frequencies. We don't observe this diffusional component at high frequencies because the displacement of ions under small AC perturbation will be small and have opposite directions. At lower frequencies, ion movement, migration under AC electric field and diffusion under concentration gradient affect each other. The conical nanopores and nanopipettes have common impedance features and differences. Notice that in glass nanopore, the Nyquist plots always show two RC components if the DC bias is not at the cross point potential. Both conical nanopores and nanopipettes have a faster transport process with shorter time constant,

which is the first semicircle component. The slower component from the complete second semicircle in conical nanopores indicates the mass transport governed by migration electric field effect. While for nanopipettes, diffusion is obviously no longer negligible and the overall transport under low frequency AC stimuli showed a mixture of electrokinetic and diffusional transport components. From these data we propose that a much longer time is needed in long stem thin wall nanopipettes for ions to redistribute thoroughly. The typical strong history dependent effect is attributed to a stronger surface electric field. Similar trends of a 6 nm nanopipette with 10 mM KCl were shown in Fig.2-2.

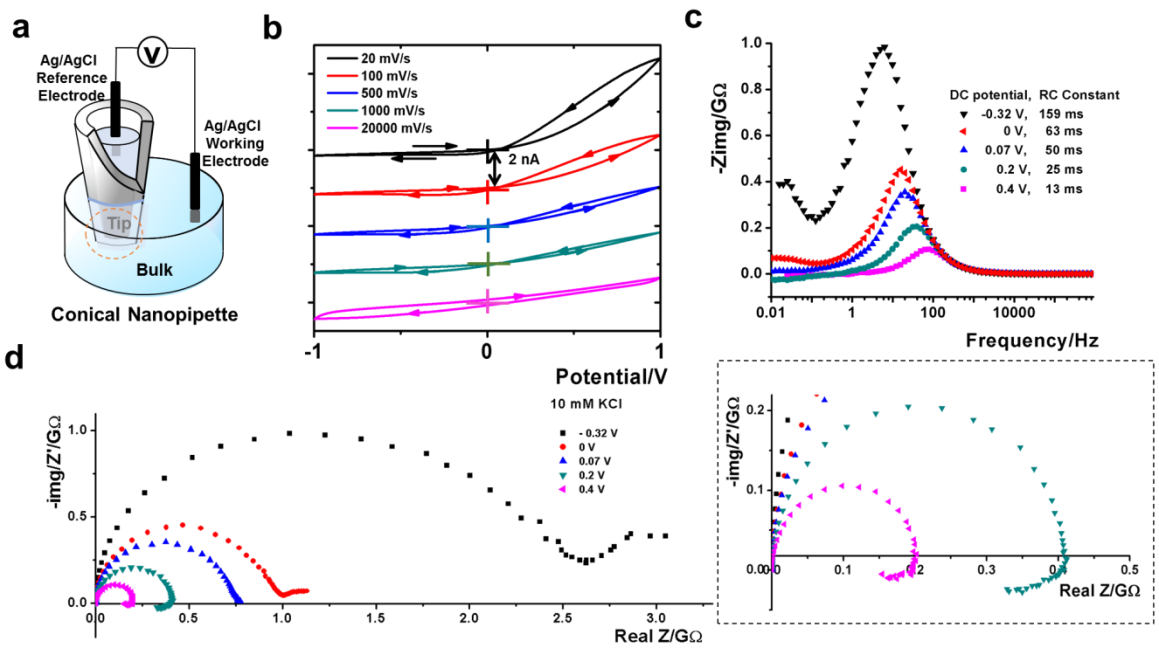

Fig. 2-2 a) Experimental setup with symmetric 10 mM KCl inside a 6 nm nanopipette and in the bulk. b) Overlaid i-v curves at different scan rates. The scale bar is 2 nA. The cross indicates the origin in each curve. The scan direction is shown by arrows. c) Bode plot and d)Nyquist plot under different DC potentials and 0.01 V AC voltage from 100 kHz to 0.01 Hz. The dashed square represents zoomed-in Nyquist plot of 0.2 V and 0.4 V.

Because the technical challenges to characterize and systematically vary the nanotip geometry experimentally, a series of simulations were performed. We start with a 5-nm-radius conical nanopore in glass membrane using previously reported geometry and simulation methods. Poisson and Nernst-Planck equations were solved numerically by Comsol Multiphysics. Known parameters such as high surface charge density and small opening were tested and ruled out that would induce such high hysteresis transport phenomena. The higher memory effect is postulated to be attributed to the finite geometry differences between the nanopipettes and nanopores that have not been resolved experimentally. A likely cause is the significant long stem with thin wall thickness (ca. 20 nm at the tip by SEM images) and/or the varying cone angles from the tip to the other end of the capillary. The nanopore geometry replicates a metal nanotip embedded in a glass membrane that is much thicker so that the exterior surface effect is anticipated less significant.

2.3.1.2 Impedance spectroscopy of nanopipettes with asymmetric ion concentration gradient

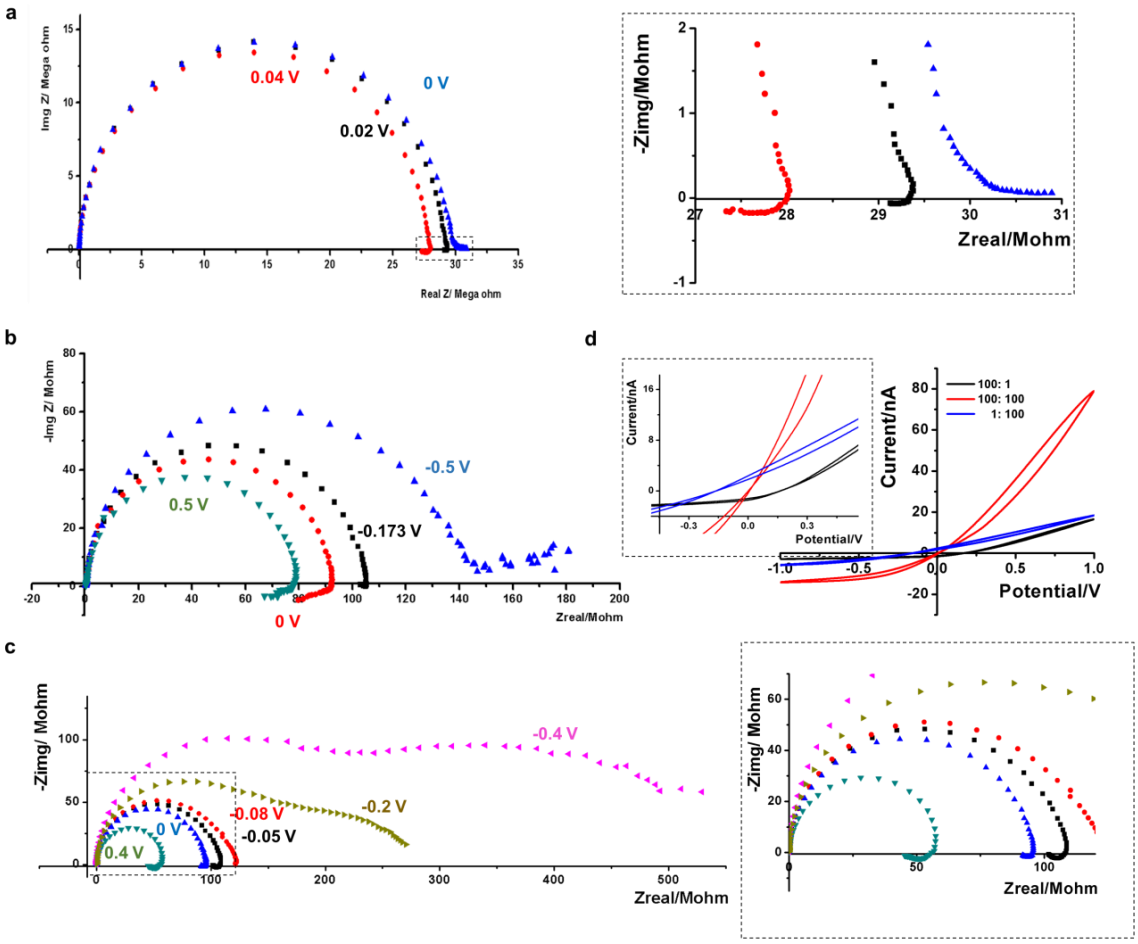

Fig. 2-3 Impedance spectroscopy of a 20 nm nanopipette with different salinity gradients across the nanotip. a) tip: bulk = 100 mM :100 mM. The dashed square represents zoomed-in Nyquist plot at low frequencies. b) tip : bulk= 100 mM :1 mM c) tip: bulk= 1 mM:100 mM The dashed square represents zoomed-in Nyquist plot at low frequencies d) Overlaid i-v curves with different asymmetric concentration gradients. The dashed square represents zoomed-in of cross points.

To investigate the hypothesis of diffusion being the root cause/physical origin of the difference in low frequency impedance responses, different concentration gradients were introduced in impedance measurements shown in Fig. 2-3. As shown in panel a, with symmetric ion concentration, at DC potential close to cross point potential

determined from i-v curves (panel d), the secondary feature is the smallest compared to the other two DC potentials that are slightly away. Note that in this nanopipette the secondary features at high and low conductivities are not the same with the secondary features for the 6 nm nanopipette before. At low conductivity it showed a diagonal line with almost 0 degree while at high conductivity it showed a deformed incomplete hemi-circle. Both these two features indicate a mixture of diffusion and electrokinetic components. The deviation from the 6 nm nanopipette might result from the fact that smaller nanopipette will have a more significant diffusion component compared to electrokinetic effect and is indicated by a pure diagonal line with a non-zero degree.

If the concentration inside the tip is higher (panel c), the impedance features at low frequency range of the nanopipettes are similar to glass nanopores and show a deformed capacitive hemi-circle at both low and high conductivity ends. With a higher bulk concentration (panel b), the diffusional component in impedance spectra will become dominant at low frequencies at both high and low conductivity sides, indicated by the diagonal line in Nyquist plots with non-zero degree.. When the constant DC potential is or near the cross point potential regardless of concentration gradient, the second feature in low frequency range, either deformed RC loop or diagonal line will diminish. This phenomenon can be explained by the balance in electric field arising from the applied potentials, surface effective potential of nanopipette and the concentration gradient. In the case of a concentration gradient is adopted between the tip and bulk solutions, a Donnan potential is established at the interfacial zone at the nanotip region that can be estimated from Nernst equation and the direction of this potential is from higher concentration to lower concentration. Due to nanopipette’s asymmetric conical

geometry, the surface effective potential direction is from the tip to the bulk. When the Donnan potential is opposite and higher than surface effective potential, the add-up direction of these two potentials is from bulk to tip, the diffusional component will be dominant and the diagonal line will show up at non-cross point DC potentials. When the concentration gradient is along the direction of surface effective potential and from tip to bulk, it will facilitate the formation of second hemi-circle loop. Typically, the nanopipette with no concentration gradient will show a mixture of a deformed semicircle and a 45 degree diagonal line, in other word a diagonal line with a smaller phase angle or a curvature, depending on the specific geometry of each pulled nanopipette. This might be due to the balance between the fixed surface effective potential and built-up concentration gradient under the applied DC potential.

Note that for the symmetric concentration and higher bulk concentration, the applied DC potential at cross point potential will result in the diminishing of the secondary feature. However, with higher tip concentration, there is a more significant inconsistency between cross point potential and the applied DC potential at which the secondary feature diminishes. The similar phenomenon can be observed in other nanopipettes too, as shown in Fig. 2-4. The reason might be due to nanopipette's asymmetric geometry and with higher tip concentration the gradient across the tip is not stable and deviates significantly from the bulk concentration gradient.

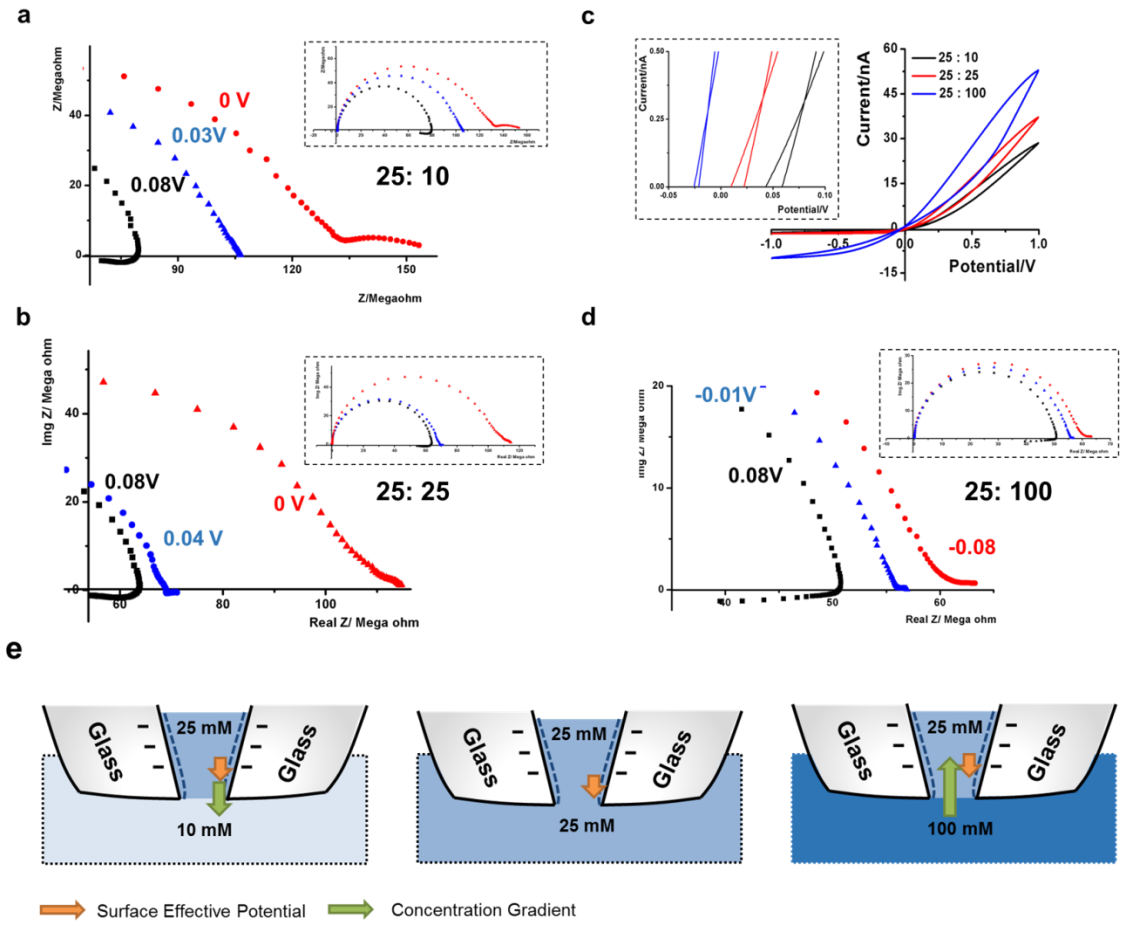

Fig. 2-4 Impedance spectroscopy of a 60 nm nanopipette with different salinity gradients across the nanotip. a) Zoomed-in Nyquist plot at low frequencies tip: bulk = 25 mM :10 mM. The dashed square represents the whole curve. b) Zoomed-in Nyquist plot at low frequencies tip: bulk = 25 mM :25 mM. The dashed square represents the whole curve. c) Overlaid i-v curves with different asymmetric concentration gradients. The dashed square represents zoomed-in of cross points. d) Zoomed-in Nyquist plot at low frequencies tip: bulk = 25 mM :100 mM. The dashed square represents the whole curve. e) Scheme representation of the direction of surface effective potential and concentration gradient under each specific concentration gradient.

2.3.2 Dynamic Enrichment and Depletion of Charges in I-V hysteresis

2.3.2.1 Dynamic Charge Enrichment and Depletion in I-V hysteresis at different scan rates with symmetric end potentials and concentration

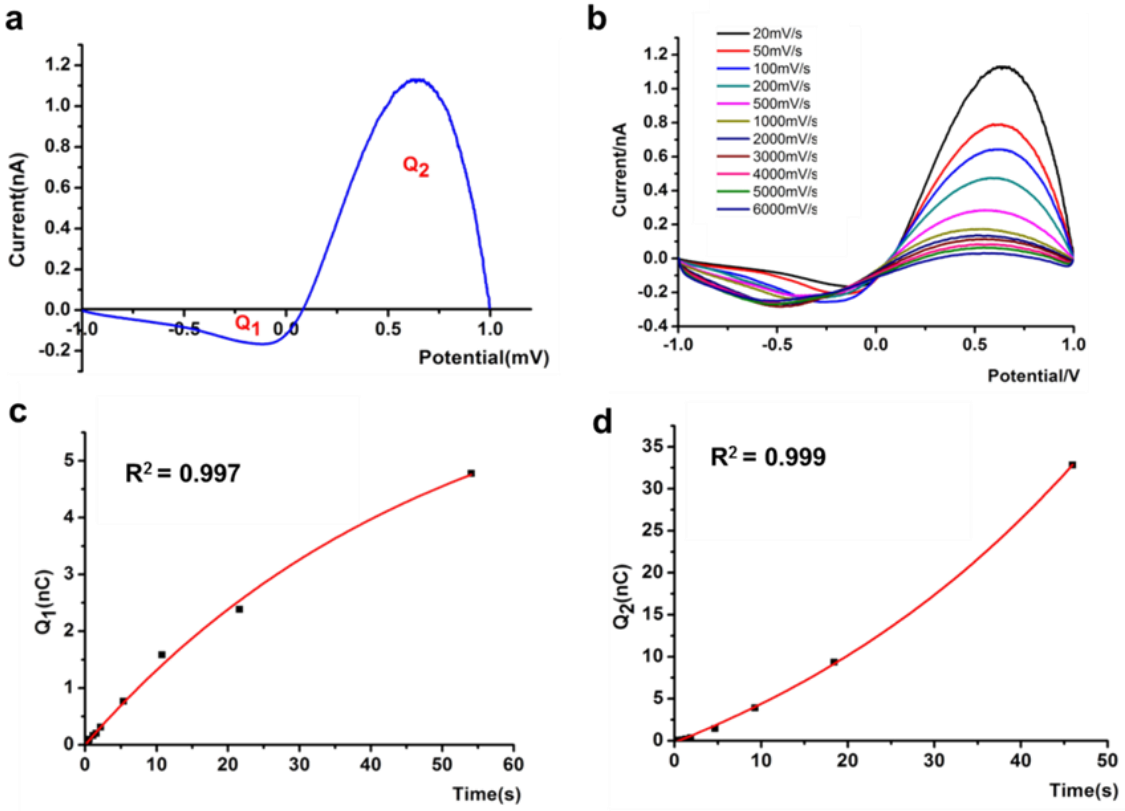

Fig. 2-5 a) A representative differential current analysis from one of the I-V curves shown in Fig. 2-1. Current data is from the subtraction of forward and backward current segments. Q_2 represents accumulated charges while Q_1 represents the depleted charges calculated from the area under the differential current divided by scan rate. b) Gap current of a 6 nm nanopipette in 10 mM KCl at different scan rates. c) Exponential dependence of Q_1 with duration. The duration is calculated from the time when the potential is scanned from the cross point potential to -1 V and then go back to cross point. d) Exponential dependence of Q_2 with duration. The duration is calculated from the time when the potential is scanned from the cross point potential to +1 V and then go back to cross point.

From Fig. 2-1 we know that at high conductivity side separated by the cross point, the forward current is smaller than backward current, the subtraction of forward current

with backward current will give us the accumulated charges that were ’trapped’ at the signal limiting nanopore region during the dynamic process driven by potential scans. Shown in Fig. 2-5 those accumulated charges are referred as Q_2 at high conductivity and similarly depleted charges as Q_1 at low conductivity end. Fig. 2-5 b showed the processed data at different scan rates. Q_1 and Q_2 are obtained by each specific integrated areas divided by scan rate, since Q = I*t = (I*V)/(V/s) = integrated area/scan rate. The lower the scan rate, the higher the charges enriched and depleted at both high and low conductivity ends. The charge Q_1 and Q_2 decrease exponentially with shorter duration (i.e. higher scan rates). Note that from these two exponential curves, for Q_1, with long enough time, the depleted charges will reach a plateau, while for Q_2， the accumulated charges will keep increasing rapidly with time, which is consistent with our finding of strong dynamic memory effect at low frequency. Charge analysis for different nanopipettes in different concentrations shows similar trend, as shown in Fig. 2-6.

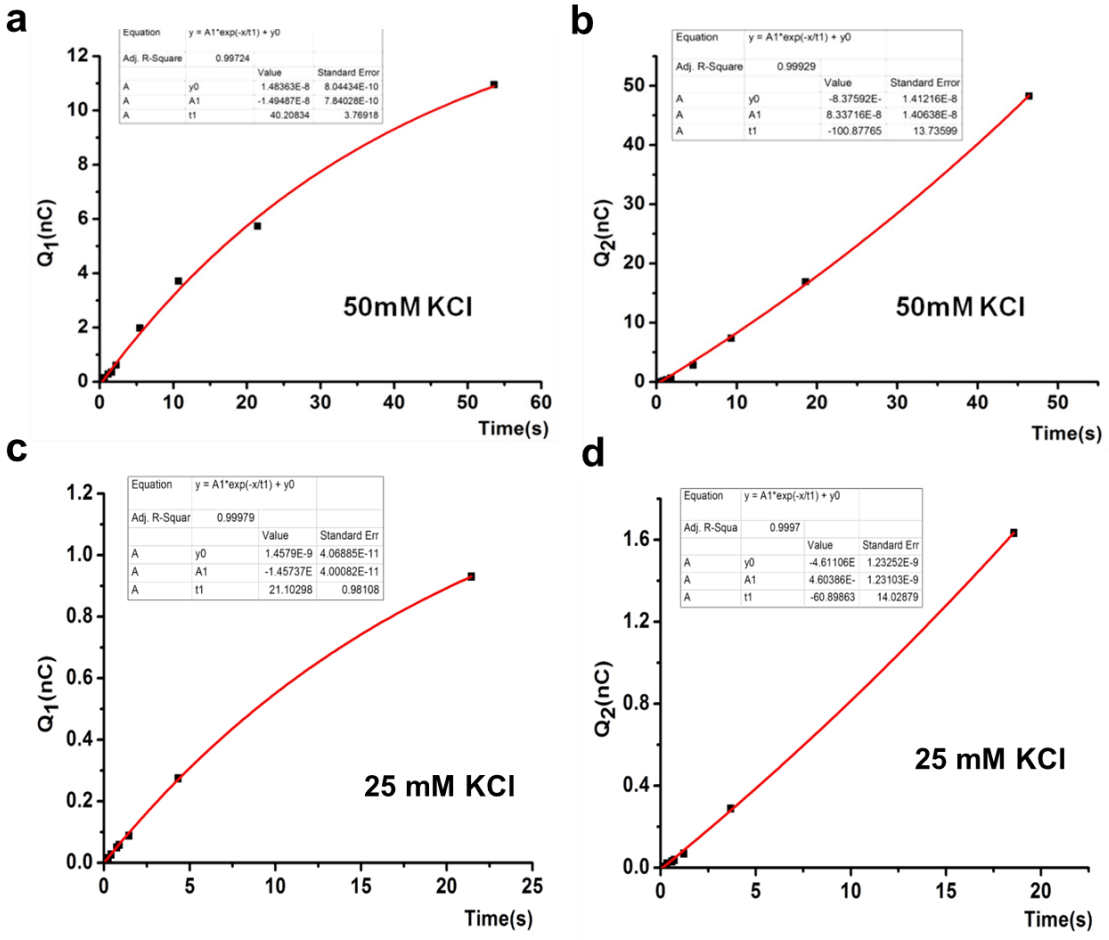

Fig. 2-6 Exponential dependence of trapped charges Q_1 and depleted charges Q_2 over durations for different nanopipettes with symmetric KCl concentration a) & b) 6 nm in 50 mM KCl; c) & d) 60 nm in 25 mM KCl.

2.3.2.2 Dynamic Charges Enrichment and Depletion in I-V hysteresis at different scan rates with symmetric end potentials but asymmetric tip to bulk concentration gradient

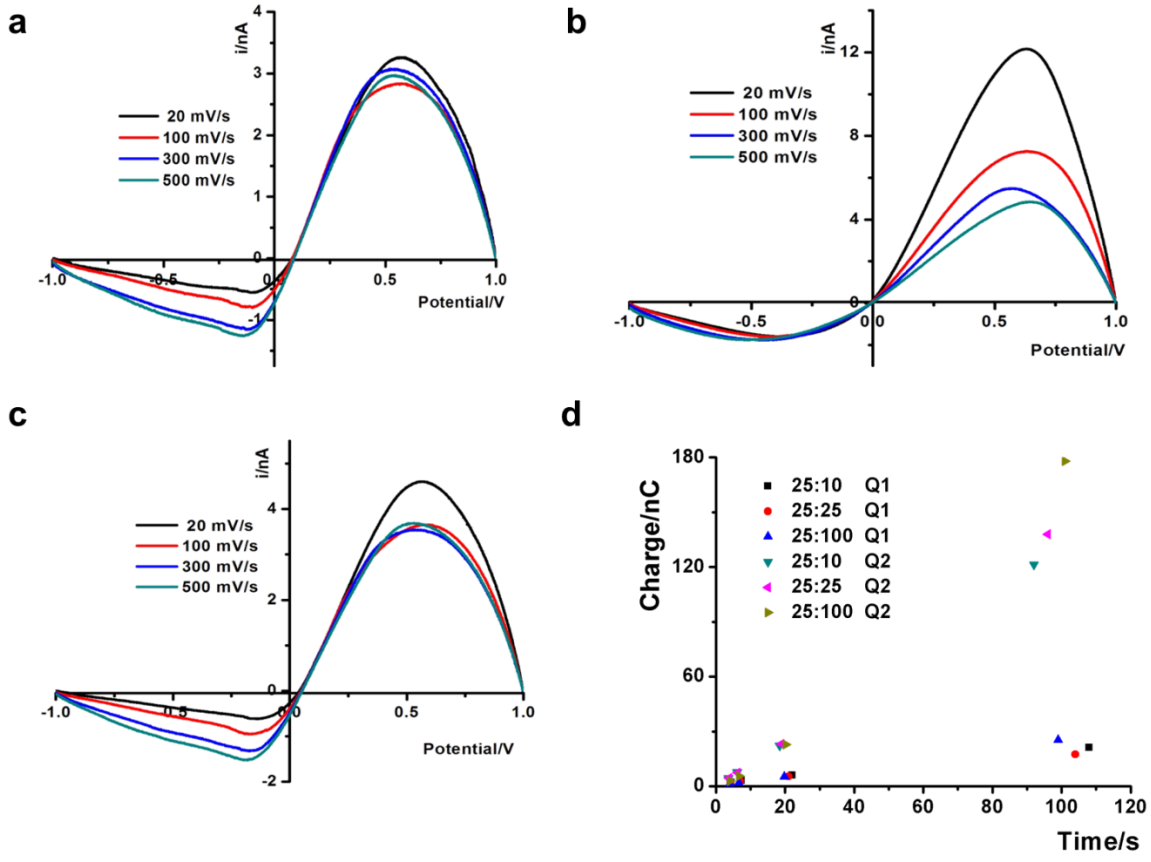

Fig. 2-7 a) Gap current with potential for the same 60 nm nanopipette at different scan rates with a) tip:bulk=25 mM:10 mM b) tip:bulk= 25 mM:100 mM c) tip:bulk=25 mM: 100 mM d) Q_1 and Q_2 over duration with asymmetric concentration gradients.

Fig. 2-7 showed representative changes in gap current with potential under asymmetric concentration gradients. With higher tip concentration, the gap current will be lower at low conductivity end for low scan rates while the gap current almost overlaps at high conductivity end. Note that cations are main charge carriers so only cations are considered in the following explanation. When the tip concentration is higher, the concentration gradient is from tip to bulk and it will facilitate the ion depletion process at

low conductivity end and hinder ion enrichment at high conductivity. With the opposite concentration gradient, the bulk to tip concentration gradient is the same with bias potential direction and facilitate cations to diffuse into the signal limiting regions at positive polarity and the gap current is higher at low scan rate at high conductivity end and gap current almost overlap at the low conductivity end. These two curves indicate clearly about the contribution of external concentration gradient to the dynamic charge trapping or depleting.

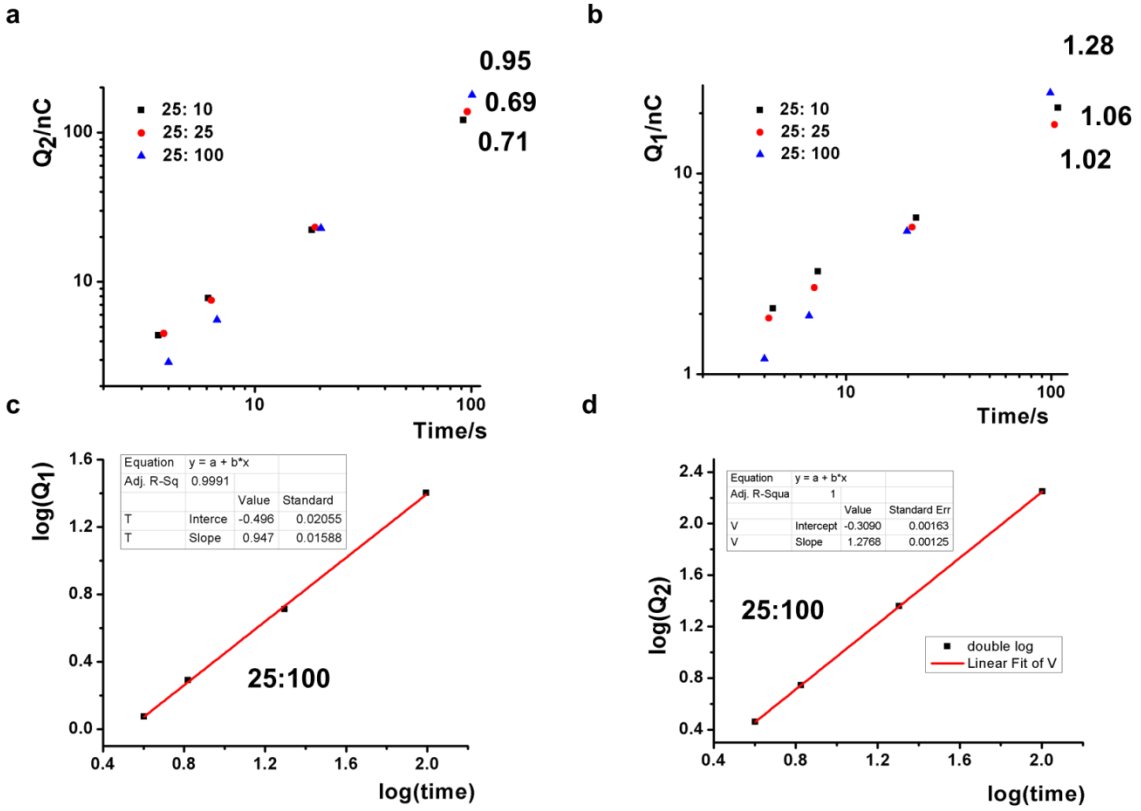

Fig. 2-8 a)Q_2 with duration for the 60 nm nanopipette with 25:10, 25:25 and 25:100 concentration gradient. The numbers in the plot show the slope of linear correlation between log Q_2 with log duration b) Q_1 with duration for the 60 nm nanopipette with 25:10, 25:25 and 25:100 concentration gradient. The numbers in the plot show the slope of linear correlation between log Q_2 with log duration c)A representative of linear correlation between log(Q_2) with log(duration) with 25:100 concentration gradient d) A representative of linear correlation between log(Q_1) with log(duration) with 25:100 concentration gradient.

Good linearity is found in the double logarithm plots between enriched or depleted charges over duration under different concentration gradients shown in Fig. 2-8. The slopes for Q_1 in the three linear fittings are close and approach to 1. The slopes for 25:10 and 25:25 are closer and the slopes for 25: 100 appear to be larger. For Q_2, at longer duration, 25:100 gives the largest charge value and 25:10 gives the smallest value. For Q_1, at longer duration, 25:100 gives the largest value while 25:25 gives the smallest value. 25:10 gives a larger value compared to 25:25. The fact that 25:100 gives the largest Q1 value might be due to the higher accumulated charges Q_2 under the 25:100 concentration gradient at high conductivity that might not be depleted to the same extent as other concentration gradients, which also contribute to Q_1 at low conductivity end. With shorter duration (faster scan rates), the surface charging effect of exterior membrane will be more significant and no long negligible as reported in our nanopore analysis. Quantitative deconvolution is required to interpret the data in future analysis.

2.3.2.3 Dynamic Charges Enrichment and Depletion in I-V hysteresis at different scan rates with asymmetric end potentials but symmetric concentration

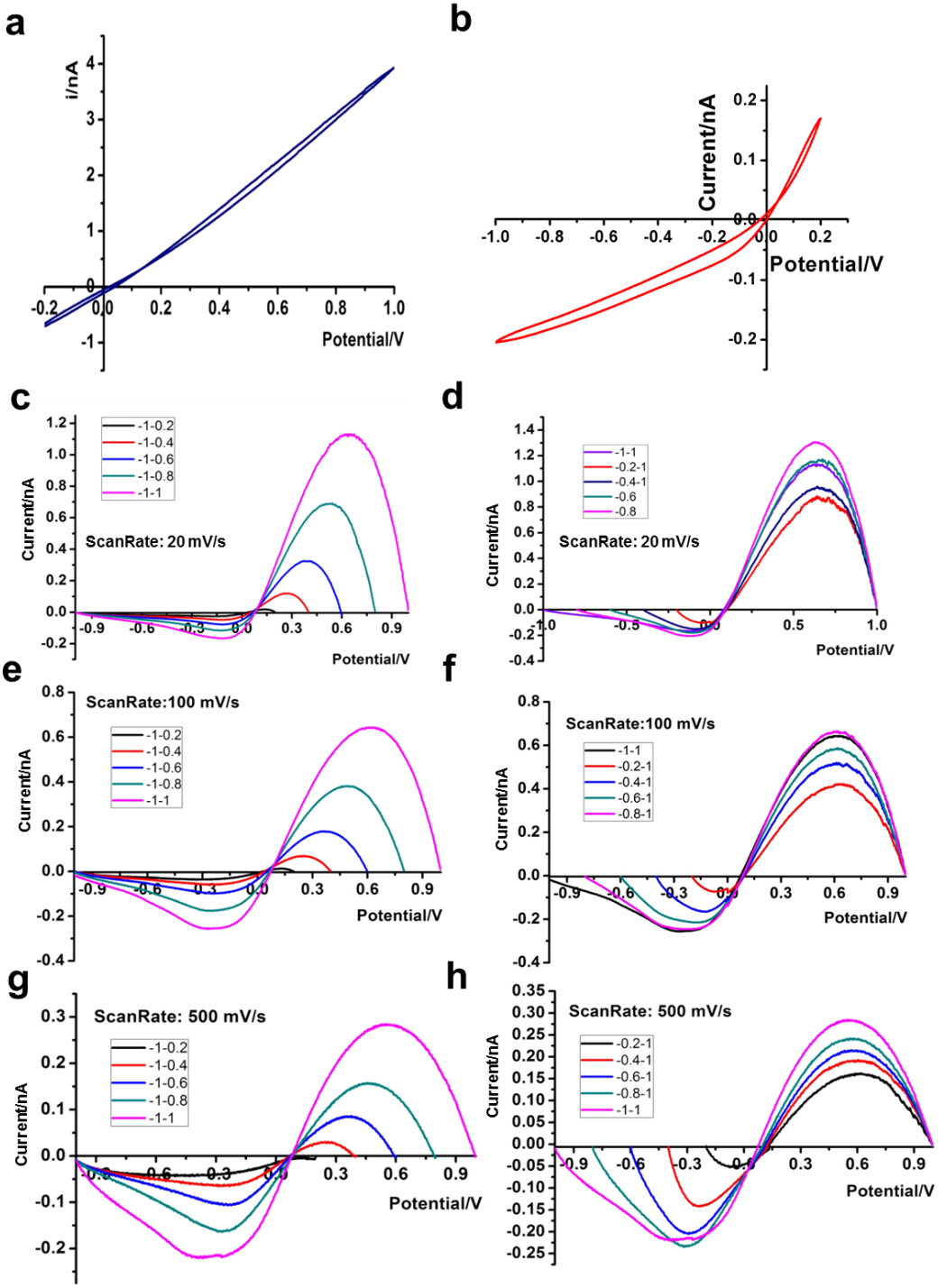

Fig. 2-9 Representation of i-v curve of a 6 nm nanopipette in 10 mM KCl at 20 mV/s with a) -0.2 V to 1 V end potential. b)-1 V to 0.2 V end potential. Gap current over potential of a 6 nm nanopipette with symmetric 10 mM KCl at different scan rates c)d) 20 mV/s e)f) 100 mV/s g)h) 500 mV/s with different end potentials.

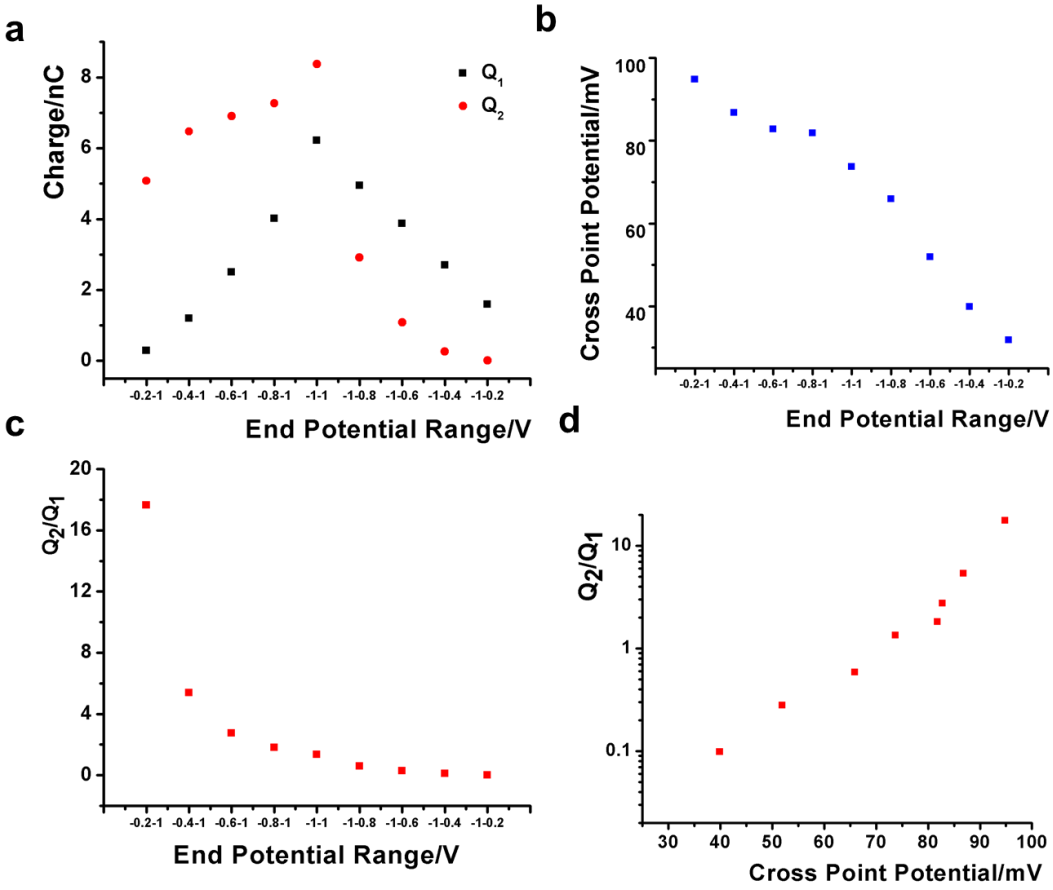

Fig. 2-10 A 6 nm nanopipette in 10 mM KCl at 100 mV/s with a)accumulated and depleted charges over different end potential ranges. b) Cross point potential change with respect to each specific end potential. c) Q_2/Q_1 over different end potentials d) Q_2/Q_1 over cross point potential.

Next we limited the end potential on one polarity to be constant, either from different negative potentials to +1 V or from different positive potentials to -1 V. The gap current at different scan rates is plotted over the respective potential range in Fig. 2-9. Two i-v curves are included in Fig. 2-9 a&b representing the original data. Note that the i-v curves were adopted after several scans until it stabilizes and there is almost no

difference from the previous scan. The cross point remains observable under those asymmetric potential ranges. The goal is to investigate the impacts of end potential (extent of concentration polarization or duration during the potential scan) on the cross point potential and the dynamics of charge redistribution. Because the variation of end potential at a constant scan rate will change the duration within each hysteresis loop, the end potential and scan rate were varied systematically.

The charges enriched and depleted and cross point potential under each end potential at 100 mV/s were shown in Fig. 2-10 a&b. From panel a we can see that both Q1 and Q2 increases when the end potential in the negative scan is decreased with common fixed +1 V in positive scans and decreases when the potential is scanned to less positive end with common -1 V. As shown in Fig.2-10 b, when the potential was scanned from different negative potentials to fixed 1 V end potential, the cross point potential decreases when negative end potential increases. And when the potential was scanned from fixed -1 V to different positive end potentials, the cross point potential will further decrease when positive end potential decreases. The similar trend was observed for this nanopipette in 10 mM KCl at 20 mV/s, as shown in Fig. 2-11 a&b. When the end potential in the positive scan is reduced, there is less time to accumulate charges at the tip signal limiting region. In other words, the ion distribution is less polarized or deviated from the native states (i.e. no bias applied), which will result in a lower concentration gradient built up inside the nanopipette tip after each complete scan. Accordingly, a smaller bias is needed to balance this small deviation, leading to a corresponding smaller cross point potential. Similarly, when the end potential in the negative scan is reduced, there will be less depletion in the charges at the nanotip region. As a result, a higher bias

is needed to balance this big concentration gradient, which will result in a higher corresponding cross point potential. That's why, for all the asymmetric end potential ranges, -1-0.2 V will give smallest cross point potential and -0.2 V-1 V will give biggest cross point potential.

The ratio of Q_2/Q_1 could indicate a 'normalized' charge built up after one complete scan at each asymmetric end potential range, which might serve as a signature to reveal the capability to select or enrich ions of a nanopipette under given conditions. As shown in Fig. 2-10 c, Q_2/Q_1 decrease with the increase of negative end potential scanned to fixed 1 V and further decrease with increase with positive end potential scanned from fixed -1 V. The correlation between Q_2/Q_1 and cross point potential is shown in Fig. 2-10 d. The linear relationship between cross point potential and $\log Q_2/Q_1$ is impressive for such challenging measurements that suggests the underpinning thermodynamics following Nernst correlations.

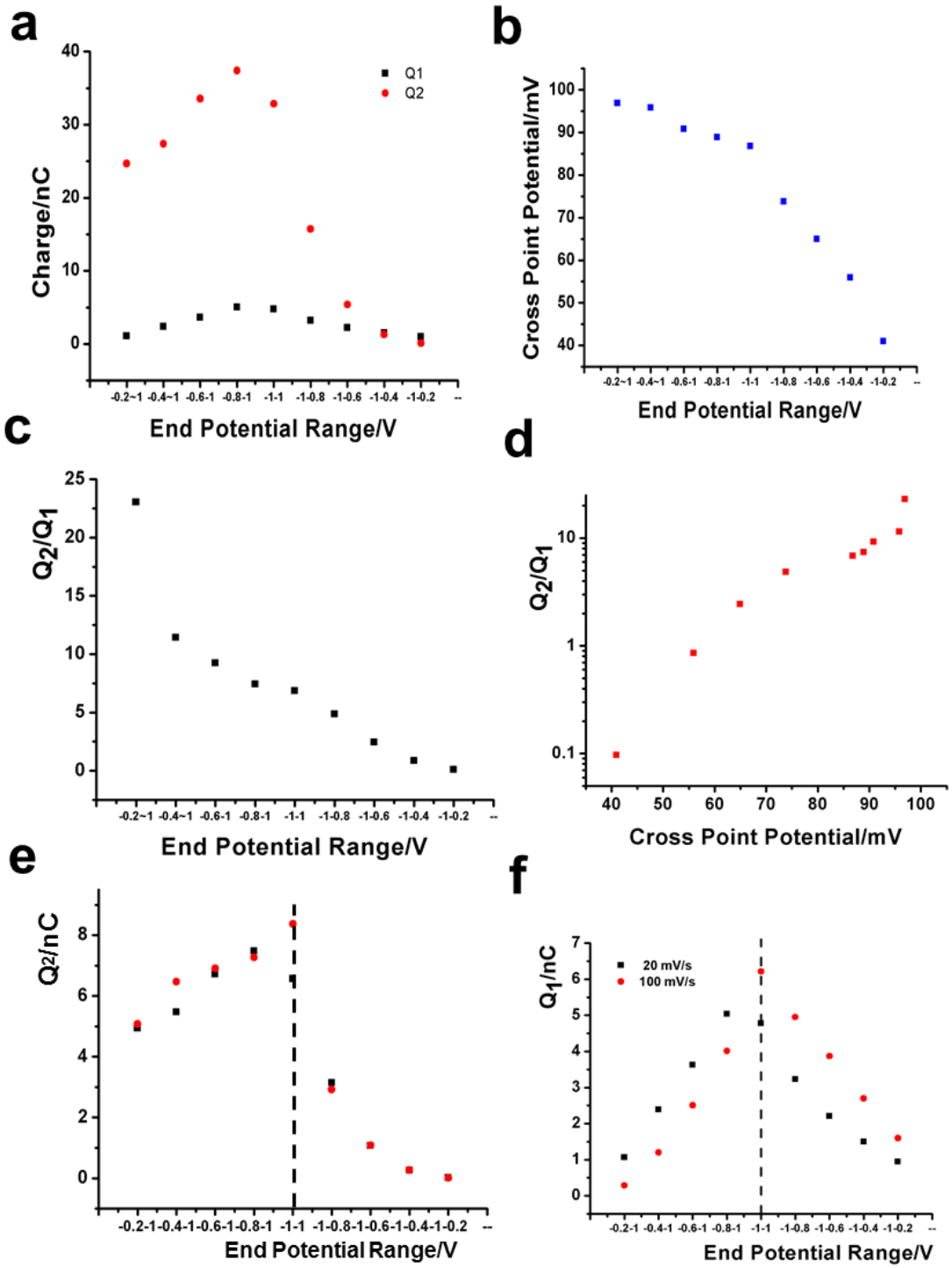

Fig. 2-11 a) Accumulated and depleted charges over different end potential ranges at 20 mV/s. b) Cross point potential with respect to each specific end potential. c) Q_2/Q_1 over different end potentials d) Q_2/Q_1 over cross point potential. e) Black dots represent Q_2 at 20 mV/s divided by 5. Red dots represent Q_2 at 100 mV/s with different end potential range. f) Q_1 at 20 mV/s and 100 mV/s with different end potential range.

To further investigate the origin of the charges enrichment and depletion under asymmetric end potential ranges under different scan rates, and to differentiate the duration effect from end potential effect, Q_2 at 20 mV/s were divided by 5, which is used to normalize the time difference with the Q_2 at 100 mV/s. The Q_2 profiles almost overlap for the two scan rates, as shown in Fig.2-11 e. It indicates the possible origin of the charges enrichment is highly time dependent. More time/duration will result in higher enrichment, which is consistent with the strong memory effect that we observed previously at low scan rates. For Q_1, as shown in Fig.2-11 f, they are very close at these two scan rates and no further division and normalization of time scale is needed. The dependence of Q_1 on time is not significant, probably indicating the intrinsic limit of each nanopipette device for ion depletion or ion selectivity.

2.3.3 Negative differential resistance

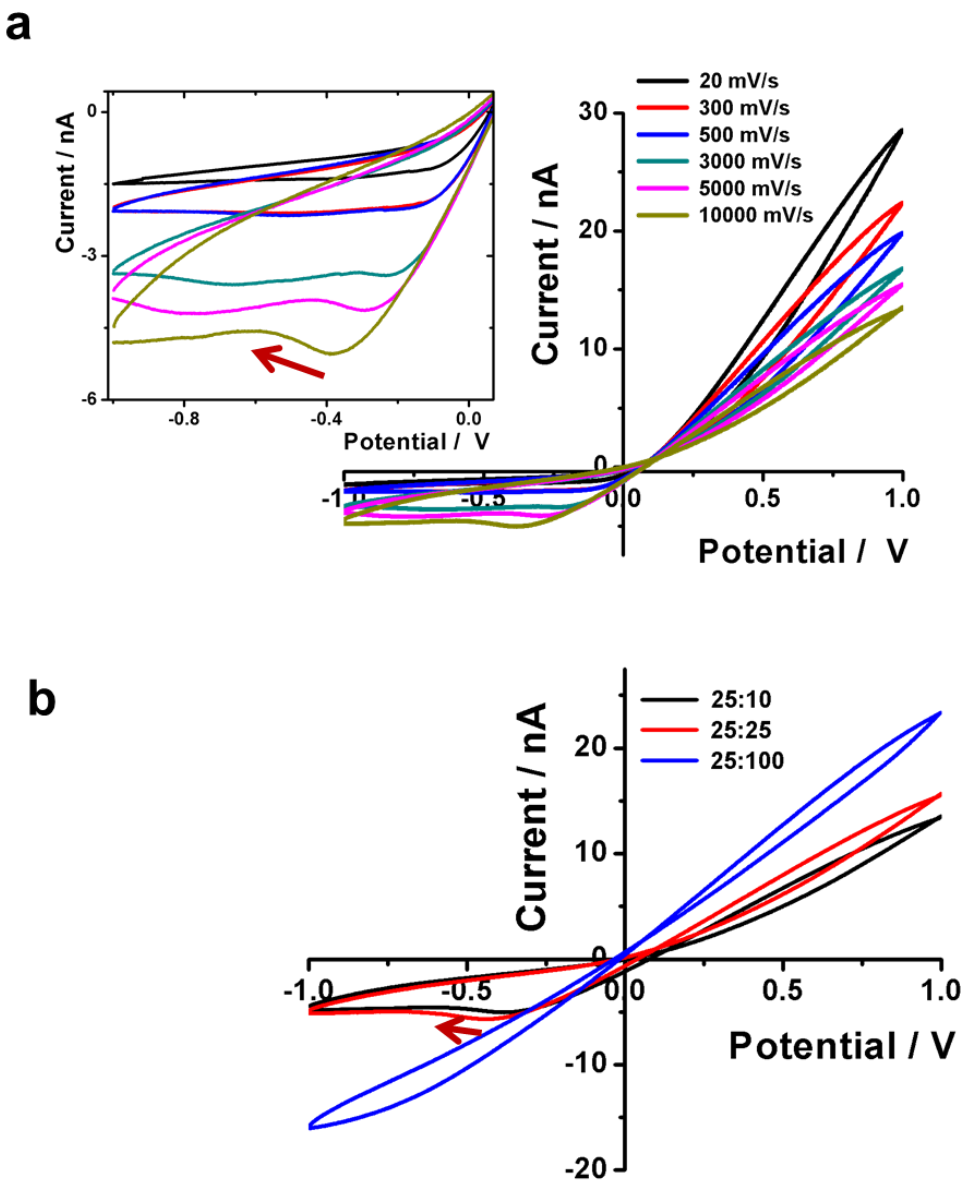

Fig. 2-12 a) Overlaid i-v curves of a 60 nm nanopipette with asymmetric concentration of 25:10 (tip:bulk) at different scan rates. Zoomed in graph shows the portions at negative potential b) Overlaid i-v curves of the same nanopipette with different asymmetric concentration gradients at 10000 mV/s.

In electronic circuits, negative differential resistance is defined as the decrease of current with bias increase. Unlike a normal or positive resistance following Ohm's law, negative resistance is characterized by $\Delta V/\Delta i<0$. White's group has reported the observation of negative resistance of ion transport behavior through nanopore with applied concentration gradient and external pressure.[25] They use a few hundred nanometer nanopore with asymmetric concentration gradient and apply pressure inside the nanopipette. Negative resistance was observed and explained to be a balance between external pressure driven flow and electroosmotic flow. Here we demonstrate that similar negative resistance can be observed directly in small opening nanopipette without any applied pressure or concentration gradient as shown in Fig.2-11 and Fig.2-12. As shown by the arrow in Fig.2-11 a, when scan rate increases at low conductivity side current magnitude starts to drop at around -0.4 V at 10000 mV/s with the increase of the applied potential. More interestingly, as shown in Fig. 2-12 b, this negative differential resistance behavior is observed in both 25:10 and 25:25 concentration gradients but not with the concentration gradient of 25:100.

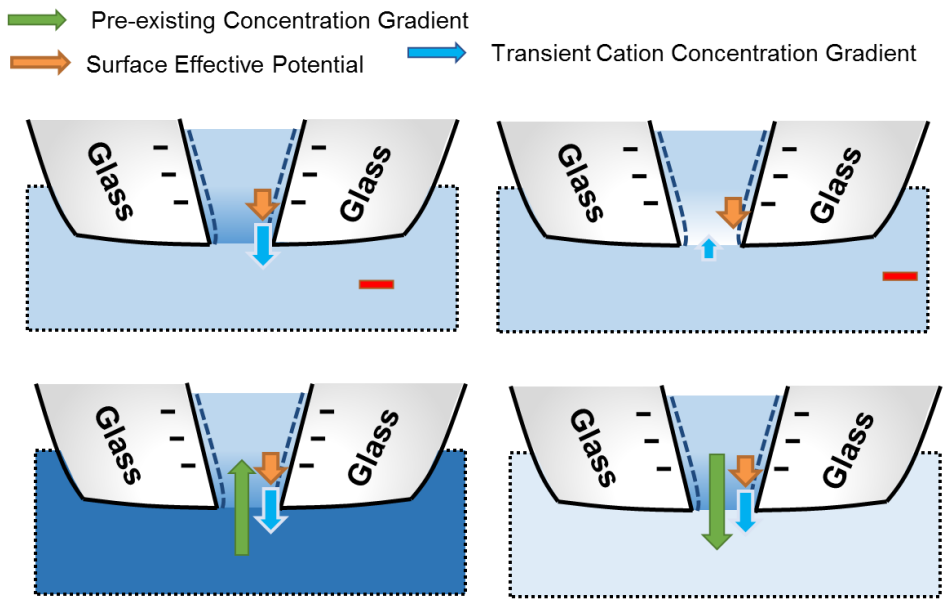

Fig. 2-13 A scheme representation of the possible physical process of negative resistance behavior formation in symmetric concentrations (top two panels) and asymmetric concentration gradient (bottom two panels)

In symmetric concentrations, due to ion trapping and enrichment after positive scan, there will be transient concentration gradient across the nanotip right after the potential is scanned toward negative, which also affects the ion transport. The direction of this transient concentration gradient is from tip to bulk and consistent with surface effective potential right pass the cross point potential. With the applied potential is scanned more negative than cross point potential continuously or gradually, this transient gradient of cations from tip to the bulk will first disappear and then even reverse the direction due to continuous depletion of ions at low conductivity end and against ion transport. This factor favors ion transport out of the tip at the beginning and decrease to a point that it might reverse the direction and hinder ions migrate outside of the tip, as shown in Fig.2-13. The interrelation of increasing bias and continuous changing of ion

concentration gradient potential lead to this negative differential resistance behavior at small opening nanopipette.

To further demonstrate the concept, after introduction of salinity gradient, with a higher bulk concentration, the enrichment of ions at the tip at high conductivity end might not be high enough so concentration gradient direction right after cross point potential is from bulk to tip and against the ion migration continuously over time, this negative resistive behavior diminishes.

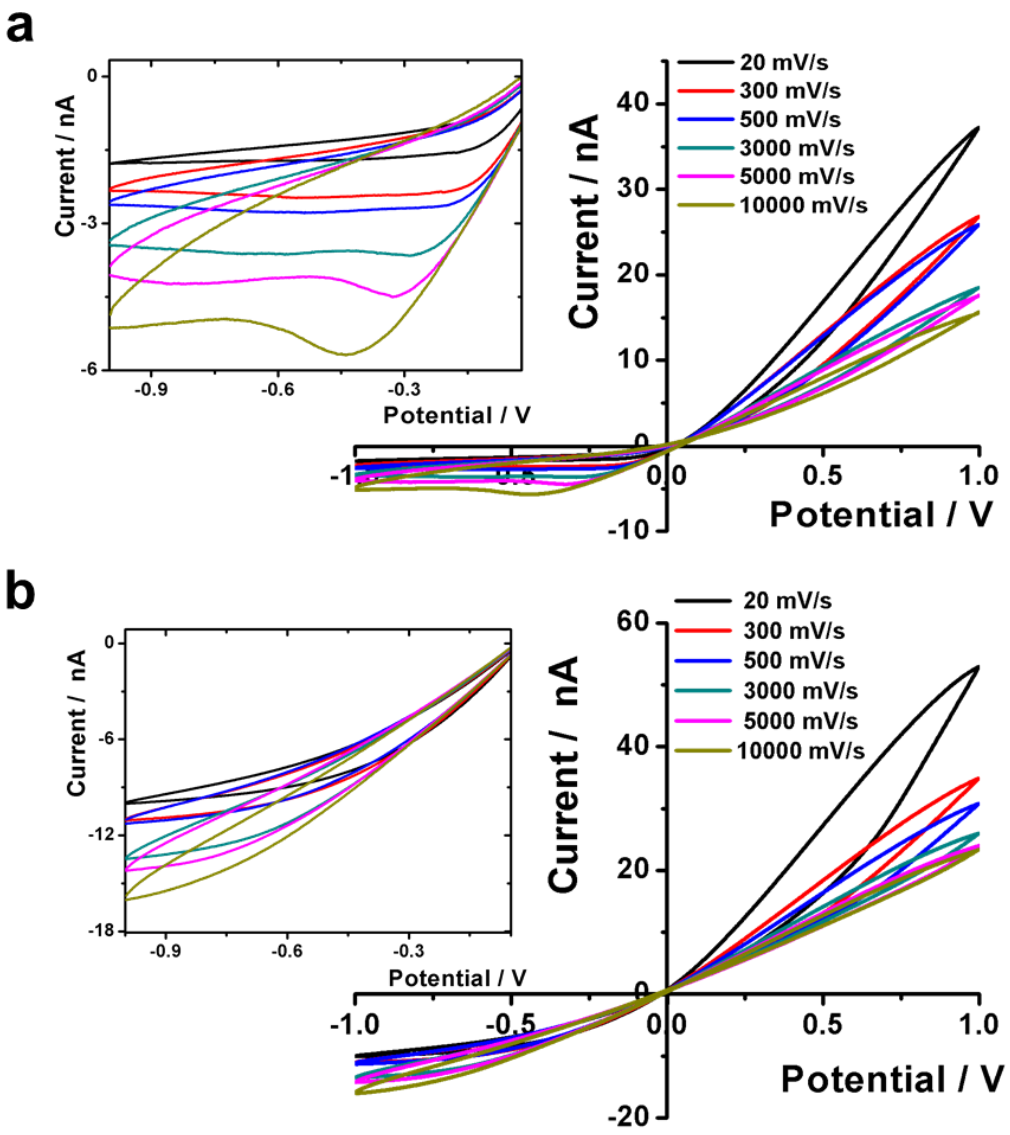

Fig. 2-14 a) Overlaid i-v curves of a 60 nm nanopipette with symmetric 25 mM KCl at different scan rates. The zoomed in graph showed the negative resistance shift with scan rate. b) Overlaid i-v curves of a nanopipette with 25 mM KCl tip and 100 mM KCl bulk at different scan rates. The zoomed-in graph showed no negative resistance.

2.4 Conclusion:

Dynamic ionic transport behaviors through nanopipettes have been investigated by different electrochemical techniques w/o concentration gradient. First, strong memory effect has been reported in nanopipette at low frequency. This strong history dependent effect is postulated to be attributed to the finite nanogeometry with long stem and thin quartz walls compared to glass membrane nanopore. More research is still needed to confirm the physical origin of this negative resistance. Second, dynamic charge enrichment and depletion analysis reveal high levels of charge enrichment at very low frequency, which is in consistent with the strong memory effect at low frequency. The shift of cross point at different end potentials was explained to be a result of dynamic charge enrichment and depletion. Third, interesting negative resistance has been observed with symmetric KCl concentration in nanopipette and postulated to be the result of transient ion enrichment at high conductivity pass cross point potential. This interesting phenomenon disappeared with the introduction of bulk to tip concentration gradient.

3 HISTORY DEPENDENT ION TRANSPORT BEHAVIOR THROUGH CONICAL NANOPIPETTES AND IMPLICATIONS IN ENERGY CONVERSION DYNAMICS AT NANOSCALE INTERFACES[62]

(This chapter has been published as "Li; Y.; Wang. D.C.; Brown, W.; Kvetny, M.; Liu, J.; Wang, G. L., History-dependent ion transport through conical nanopipettes and the implications in energy conversion dynamics at nanoscale interfaces. *Chem. Sci.*, 2015, **6**, 588–595." Reprinted with permission from Ref 62. Copyright 2015, Royal Society of Chemistry.)

The dynamics of the ion transport at nanostructured substrate-solution interfaces plays vital roles in high-density energy conversion, stochastic chemical and biosensing, membrane separation, nanofluidics and fundamental nanoelectrochemistry. Further advancements in those applications require fundamental understanding of the ion transport at nanoscale interfaces. Understanding in the dynamic or transient transport, the key physical process involved, is limited, which contrast sharply to the widely studied steady-state ion transport features at atomic and nanometer scale interfaces. Here we report striking time-dependent ion transport characteristics at nanoscale interfaces in current-potential (I-V) measurements and theoretical analysis. First, a unique non-zero I-V cross-point and pinched I-V curves are established as signatures to characterize the dynamics of ion transport through individual conical nanopipettes. Second, ion transport against a concentration gradient is regulated by applied and surface electrical fields. The concept of ion pump or separation is demonstrated via the selective ion transport against concentration gradients through individual nanopipettes. Third, this dynamic ion transport process under predefined salinity gradient is discussed in the context of nanoscale energy conversion in, i.e. supercapacitor type charging-discharging as well as chemical and electrical energy conversions. The analysis of the emerging current-

potential features establishes the urgently needed physical foundation for energy conversion employing ordered nanostructures. The elucidated mechanism and established methodology are generalizable to broadly-defined nanoporous materials and devices for improved energy, separation and sensing applications.

3.1 Introduction

The transport of charges at solid-solution interfaces is a key step in fundamental electrochemistry,[63,64] energy technology (i.e. charging and discharging of supercapacitors, fuel cells and batteries),[65-67] separation (i.e. desalination, filtration),[68] sensing (i.e. DNA sequencing and stochastic single molecule detection),[69-71] and natural processes in biology (i.e. ion channels and pumps) and geoscience.[72] Materials and devices with defined atomic and nanometer scale pore structures have great potentials to enhance the efficacy and/or efficiency of those applications.[73,74] At nanoscale interfaces, novel transport phenomena emerge that require further experimental and theoretical studies. Representative features include steady-state ion current rectification (ICR),[19,75,76] apparent inductive behaviors,[22] mem-capacitance,[77] and 'abnormal' hysteresis and capacitance responses under high-frequency electric field stimulation[23,78,79] observed in different channel-type nanodevices.

The ion transport process is associated with energy conversion and characterized by current *I*, potential *V* or power (*I*V*). Recent advances in steady-state studies pave the way for better understandings of the dynamic ion transport at nanoscale interfaces, which are urgently needed to advance three types of important applications. First, ion transport through porous electrodes is a physical process and rate-limiting step in the charging and discharging of electrochemical capacitors (supercapacitors). Supercapacitors are widely

used as energy device complementing or competing with batteries etc. One of the key merits of supercapacitors is that they deliver high power. The high power unfortunately leads to a major limitation: they don't last long before a recharge is needed. It is therefore highly desirable to control the power output, or the charging and discharging kinetics. Two other applications are inspired by natural processes of protein ion pumps in which chemical energy (i.e. ATP-ADP) is converted into electrochemical potential in terms of action potential, concentration gradient etc. In the second type applications, electrical energy is harvested i.e. from salinity gradient, pressure driven flow, etc. with classic ion selective membranes and recently using nanopores. Third, selective ion transport will enable ion enrichment/depletion or separation (i.e. desalination by consumption of electricity, light, etc.).[80-88] The main limiting factors for improvements reside in the lack of fundamental physical understanding of the transport dynamics and the needs of significant enhancements in methodology.

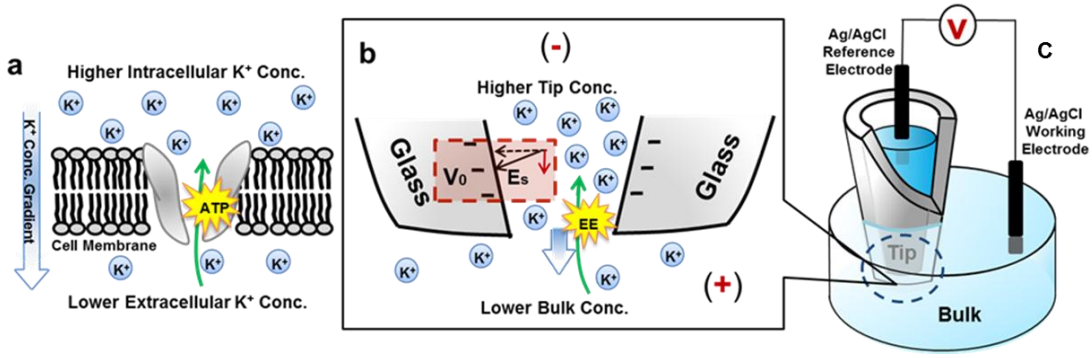

Fig. 3-1 Scheme of a nanopore in transmembrane protein and solid state nanopipette under ion concentration gradient**.**

a) A K^+ ion pump in lipid bilayer that transports K^+ against concentration gradient by ATP hydrolysis. **b)** Enlarged view of nanopipette tip under high-tip-low-bulk concentration gradient. Quartz/Glass serves as the counterpart of the insulating lipid bilayer. K^+ ions could migrate against concentration gradient driven by external electrical energy (**EE**). Cl^- ions are omitted due to lower contribution to the ion flux as a result of repulsion from negative surface charges. Surface potential V_0 and the direction of the

surface electric field E_s are highlighted. **c)** Experimental setup. The bias is defined as bulk versus tip.

Our approach to analyze dynamic transport through solid-state nanopores in comparison to protein ion pumps is illustrated in Fig. 3-1. A nanopore in quartz substrate allows the exchange of ions between the tip and bulk solutions. Unlike the energy from ATP hydrolysis being converted into concentration gradient, an alternating bias is applied to drive the dynamic ion transport. This corresponds to the charging and discharging of a nanometer sized capacitor, or an individual element in an ensemble porous membrane. The dynamic ion transport gains substantial contributions from the tip-localized surface electric field. Further, the salinity gradient on the two sides of the nanopore in bulk solutions is introduced. The predefined salinity gradient enables the analysis of the energy conversion between electric and chemical potential. The conversion efficiency is time dependent and characterized by power. Highlighted in panel b inset, surface electric field has a component E_s along the direction of ion flux (or applied field) that distinguishes this asymmetric nano-geometry platform from symmetric nanochannels, and from amorphous or ensemble porous membranes. The transport limiting tip region has an orifice radius a few tens of nanometers. Correspondingly, high efficiency energy conversion is achieved in terms of nanointerface enhanced ion transport.

The dynamic transport studies reveal two key aspects previously inaccessible in the commonly-adopted steady-state analysis. For clarification, a comparison between steady-state and dynamic/transient transport is analogous to that of uniform velocity versus acceleration/deceleration. The physical meaning of the power generation, i.e. energy conversion between (chemical and electrical energy), is revealed directly from the

dynamic ion transport with concentration gradient, and this conversion capacity is characterized by a non-zero point (*I(t)*V(t)*) from time-dependent I-V measurements. This is fundamentally different from a multiplication of open circuit potential (at I=0) and short circuit current (at V=0), which are measured separately and correspond to power (I*V) zero in either case. Albeit the analysis is routinely employed in the evaluation of conventional electronic circuits, its application to the ion transport through nanopores raises concerns because the resistance and/or capacitance of the nanopore system is not constant. Second, the energy conversion efficiency or power is found to depend on previous-conductivity-state. This history-dependent feature, not captured in previous studies, enables the elucidation of drastic enhancement by surface electric field. The findings are generalizable for different types of substrate-solution interfaces, therefore broadly impact the aforementioned applications.

We first lay the foundation by introducing time-dependent hysteresis I-V features in symmetric tip: bulk concentration conditions. A unique non-zero I-V cross-point and pinched I-V loops are then employed as characteristics to evaluate the efficacy of energy conversion and pumping ions against concentration gradient in asymmetric concentrations. Theoretical equations are developed by correlating the cross-point potential and current clamping in I-V and V-t studies respectively, through which significant surface impacts and the contributions by diffusion and migration to the overall measured current signal are elucidated.

3.2 Methods and Materials:

Quartz nanopipettes were fabricated with P-2000 puller (Sutter Instrument Co.) using quartz capillaries (O.D.:1.0 mm, I.D.: 0.7 mm). The pulling parameters of the

nanopipettes are as follows: Heat: 700, Filament: 4, Velocity: 60, Del: 150, Pull: 120. The experiments were performed with Gamry Reference 600 (Gamry Co.). Two Ag/AgCl wires were used as electrodes. One was immersed inside of the nanopipette as reference electrode while the other one in the bulk solution as working electrode. Bias is therefore defined as outside versus inside. The current was recorded under an applied triangular potential waveform at 100 mV/s scan rate. The reported stable I-V curves were recorded after discarding the first few I-V segments and confirmed by the overlap of last five scans. To ensure the designed concentration gradient, the nanopipette will be centrifuged ca. 20 min after replacing the tip solution. Reproducible I-V responses in symmetric setups were recorded between each asymmetric study to affirm the proper concentrations being used. After each set of I-V measurements with same tip concentration, additional I-V measurements under at least one asymmetric condition were conducted to demonstrate stability and reproducibility of the measurements.

3.3 Results and Discussion

3.3.1 Characterization of nanopipette geometry

The radius and half cone angle θ of pulled quartz nanopipettes are characterized by scanning electron microscope (SEM) imaging shown in Fig. 3-2, and the conductivity analysis is described below.

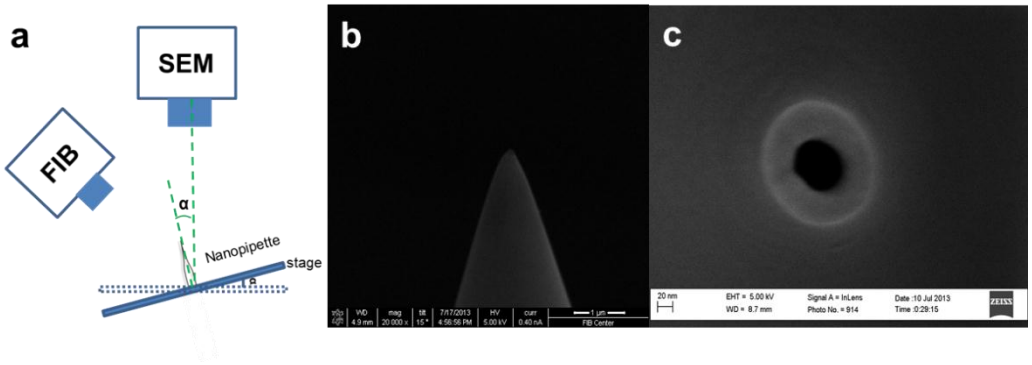

Figure 3-2 a) Schematic diagram of a FEI Nova Nanolab 200 workstation with Focused Ion Beam (FIB) and SEM modes. The sample stage was tilted at 15 ° during imaging. b) Side-view of a nanopipette at 15 ° tilt angle under FIB/SEM mode. Scale bar is 1 μm. c) SEM top-view of the same nanopipette by Zeiss Ultra60 FE-SEM. The quartz nanopipette was spatter coated with a thin layer of Au/Pt alloy prior imaging. Scale bar is 20 nm.

The cone angle in Fig. 3-7 is measured to be 37.5°. The half cone angle θ is determined to be 5.5 ° using equation: $\tan(2\theta) = \tan(37.5) \times \cos(90 - \alpha)$. Here, α is the tilt degree at 15 °.

Conductivity analysis:

The size of the nanopipettes is normally calculated from conductivity results in literature. The nanopipette size/s used in those i-V studies were analyzed following the same procedure in literature detailed below.

The total pipette resistance comprises two major components: R_{geo} and R_{acc}, where R_{geo} is geometric resistance and R_{acc} is access resistance. R_{acc} is determined by its radius and solution conductivity given that the pipette orifice is disk-shaped in approximation.

$$R_{geo} = \frac{\rho h}{\pi r(r + h\tan\theta)}, \quad R_{acc} = \frac{\rho}{4r}, \quad R = R_{geo} + R_{acc} = \frac{\rho h}{\pi r(r + h\tan\theta)} + \frac{\rho}{4r}$$

Here, R is the resistance of solution. ρ is resistivity of the medium. h is the effective length. θ is the half cone. Because of the long stem of the pulled nanopipettes and the small radius employed in this study, r+htanθ is approximated to htanθ. Then,

$$R = \frac{\rho}{\pi r \tan\theta} + \frac{\rho}{4r}, \qquad r = \frac{4\rho + \rho\pi\tan\theta}{4\pi R \tan\theta}$$

Here, θ is equal to 5.5^{o} and R can be calculated from the slope of i-V curves in high electrolyte concentration near zero bias that normally displays linear responses.

3.3.2 Dynamic I-V features from ion transport through a quartz nanopipette under symmetric tip-bulk concentrations

Representative ionic current responses of conical nanopipettes under a scanning triangular potential waveform are shown in Fig. 3-3. The nanogeometry is analyzed by scanning electron microscope and conductivity measurements (Fig.3-2). The immediate notable feature in each curve is that in the cyclic scans (scan direction shown in inset), two hysteresis loops are separated by a unique cross-point at a small positive bias rather than origin. The large hysteresis effects at such low frequency range indicate significant surface effects on pulled conical nanopipettes. Similar I-V features on a new device platform is in agreement with our recent report of pinched hysteresis loops and a non-zero cross-point in the ion transport through bench-top fabricated conical nanopores, and thus strongly supports the proposed analysis therein.[23] Such dynamic I-V features have not been observed in steady-state transport studies using broadly defined channel-type

nanodevices to the best of our knowledge. To compare with steady-state responses, the non-linear I-V curve of each scan segment, specifically the current amplitude being higher at one bias than that at the opposite bias polarity, corresponds to the well-known ICR behavior.[11,19,59,89-91] A key difference is that the I-V curve does not necessarily cross through the origin (0,0) as approximated in previous reports.

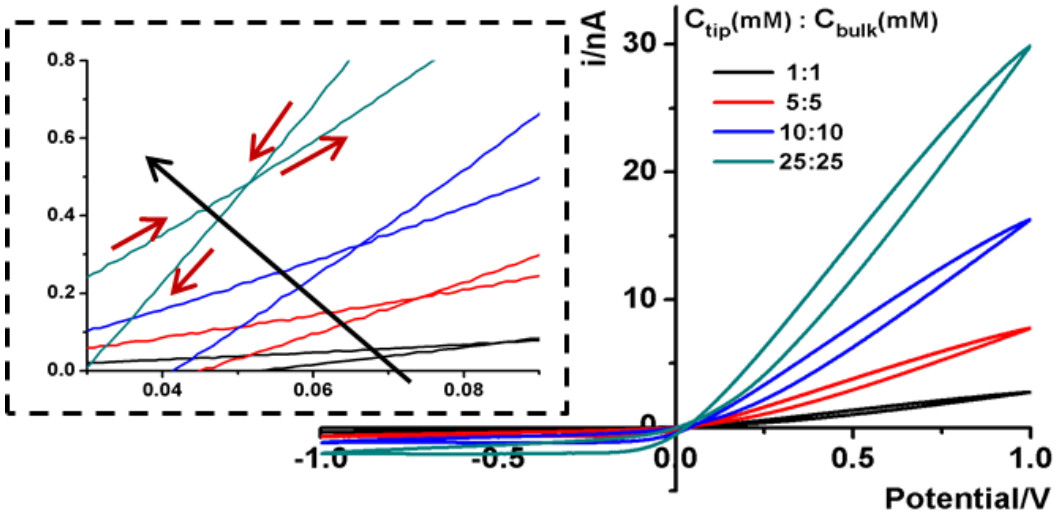

Fig. 3-3 Representative I-V features of a 60-nm-radius nanopipette in symmetric tip:bulk KCl concentrations.
Scan rate is 100 mV/s. Inset shows the scan directions and the cross-point position of all I-V curves. The shift in cross-point with the increase of concentration is indicated by the long arrow.

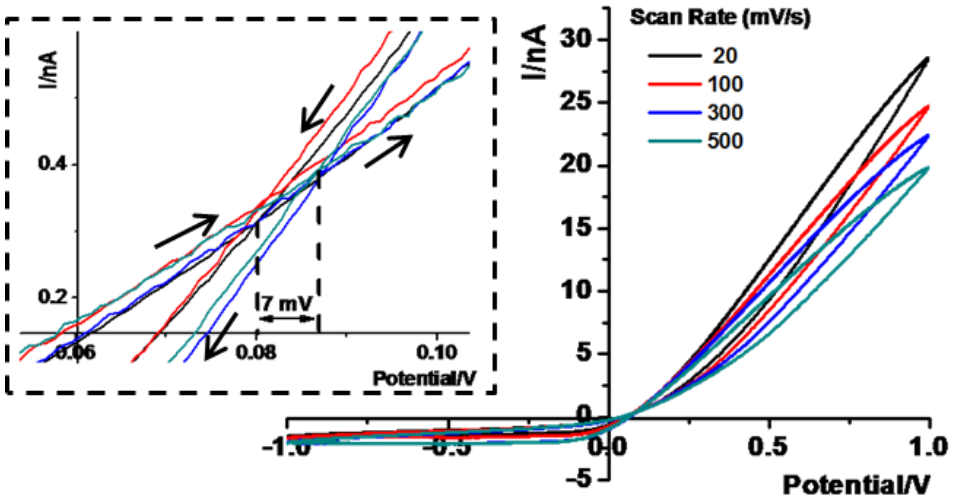

Figure 3-4 Overlaid i-V curves of the 60-nm nanopipette in symmetric 25:25 tip:bulk concentrations at different scan rates. The inset shows the zoom in around the cross point. The largest difference in cross point potential is around 7 mV. The arrows show scan direction.

The intriguing observation of a unique non-zero I-V cross-point separating opposite hysteresis loops reveal unknown fundamental ion transport dynamics at nanoscale interfaces. In solution I-V measurements, a hysteresis loop is normally interpreted as capacitive responses. On the low conductivity side (defined as more negative bias from cross-point), ionic current displays a hysteresis corresponding to normal capacitive behavior, or positive phase shift of current responses with respect to the applied scanning potential waveform. On the high conductivity side, however, the measured current shows a hysteresis corresponding to negative phase shift, or negative capacitive responses. This negative phase shift is in agreement with the 'apparent inductive' or 'negative capacitive' behaviors reported in impedance experiments and molecular dynamic simulations on different types of nanochannel platforms

respectively.[22,77] Rooted on the steady-state ICR studies, those dynamic ion transport features observed from different nanochannel platforms have been attributed to surface electric field effects. [22,23,77-79]

Solution ionic strength is systematically varied to unveil the impacts on the hysteresis I-V features by surface electric field shown in Fig.3-3. On SiO_2 substrate, surface electric field originates from the negative surface charges due to the deprotonation of surface silanol groups. With the increase in KCl concentration, electrostatic interactions between mobile ions and surface charges are more effectively screened. The cross-point potential V_{cpp} decreases accordingly. The current (in general and at cross-point) increase at higher KCl concentration because more charge carriers (mobile ions) are accessible to the current-limiting nanotip region.

The cross-point can be understood as corresponding to the applied field that balances the effective surface electric field E_s across the quartz membrane at the nanotip region in potential scanning experiments (Fig.1b) explained in our early reports.[23 92] For easy perception, we use the elongation/compression of a spring as an analogy here. A spring mimics the nanopipette, with the relaxed state (length L) corresponding to the intrinsic surface charges/potential and nanogeometry. Next we consider the surface effects in ionic solution as the weight added. The spring will elongate differently with different weights (L+W). This scenario mimics the cross-point that appears at non-zero position and depends on solution ionic strength. Without external bias, the ion distribution at the nanopipette tip region is established by the intrinsic surface electric field. The EDL at the nanointerface is at rest or unpolarized. The net ion flux or transport current is zero. Under an external bias, ion flux will alter the ion distribution, or polarize

the EDL structure at the nanotip region. Accordingly, surface effects emerge and affect the measured current because the surface electric field is no longer balanced. The true steady-state, with non-zero flux/current, is established when the applied bias is equal to the effective surface potential across the nanotip.

If the spring setup is further stretched by an external force to L+W+P, (P represents the impacts by an external bias in I-V measurements), regardless of further stretching or a release by the external force, the spring setup itself will tend to recover toward L+W. Similarly, regardless if the bias is scanned in the forward or backward directions, i.e. from +0.5 V away from or toward the cross point, within one of the hysteresis loops, the surface EDL tends to recover to the rest state. In other words, the surface effects will continue to enrich the ions in high conductivity loop and deplete ions in the low conductivity loop regardless of bias scan directions. Further, because the ion flux is not zero immediately before the bias is scanned to zero, non-zero current signals are detected 'memorizing' the previous conductivity states due to the still-polarized EDL. The true steady-state is established at the cross point when the extent of the EDL polarization leads to a match in the magnitude of the surface and applied electric fields along the ion transport direction.

Steady-state ICR (i-V branch from the backward scan as a better mimic due to longer accumulation) results from the overlapping effects of the intrinsic surface electric field with respect to a constant applied electric field. Accordingly, the hysteresis effects are attributed to the differences in the kinetics of the applied potential (determined by scan rate, or frequency) with respect to the responding ion transport through the nanopipette. It is worthy pointing out that the direction of E_s is solely determined by the

surface charge polarity, albeit its magnitude varies at different ionic strength and at different applied bias because it depends on the ionic distribution at the nanotip. Therefore, at a bias more positive than the cross-point, the surface field consistently facilitates ion transport driven by the applied field regardless of the respective magnitudes, thereby reducing resistance and cause negative capacitance, correspondingly the high conductivity states and negative I-V hysteresis.

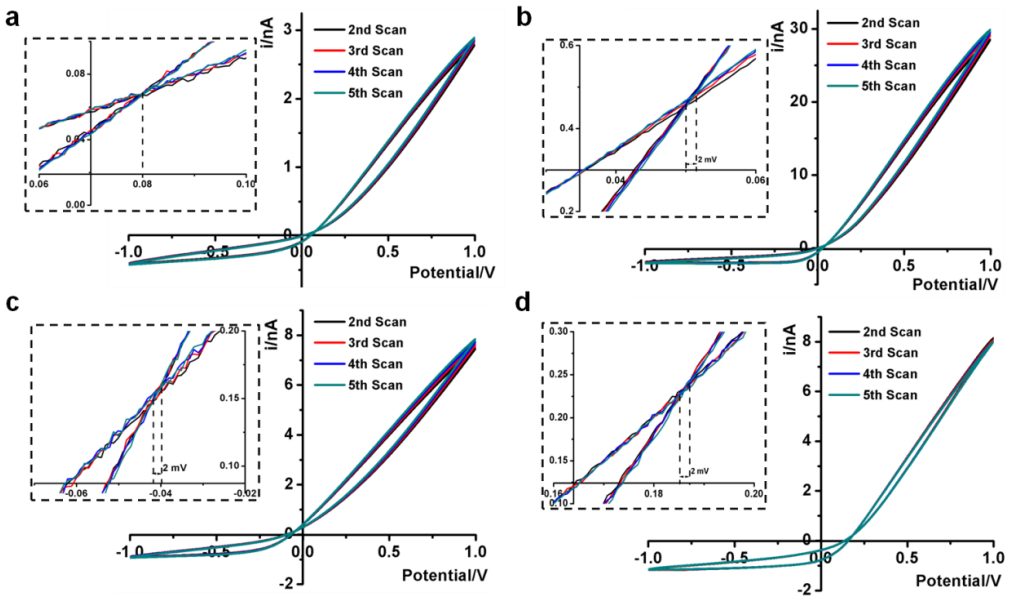

Figure 3-5 Overlaid i-V curves of the 60-nm nanopipette in a) 1:1 b) 25:25 c) 1:25 d) 25:1 tip:bulk concentrations. Four complete scans at 100 mV/s scan rates are included in each panel. The first segment was discarded because the signals are affected by unknown pre-existing solution conditions. The insets show the zoom in part around the cross point potential.

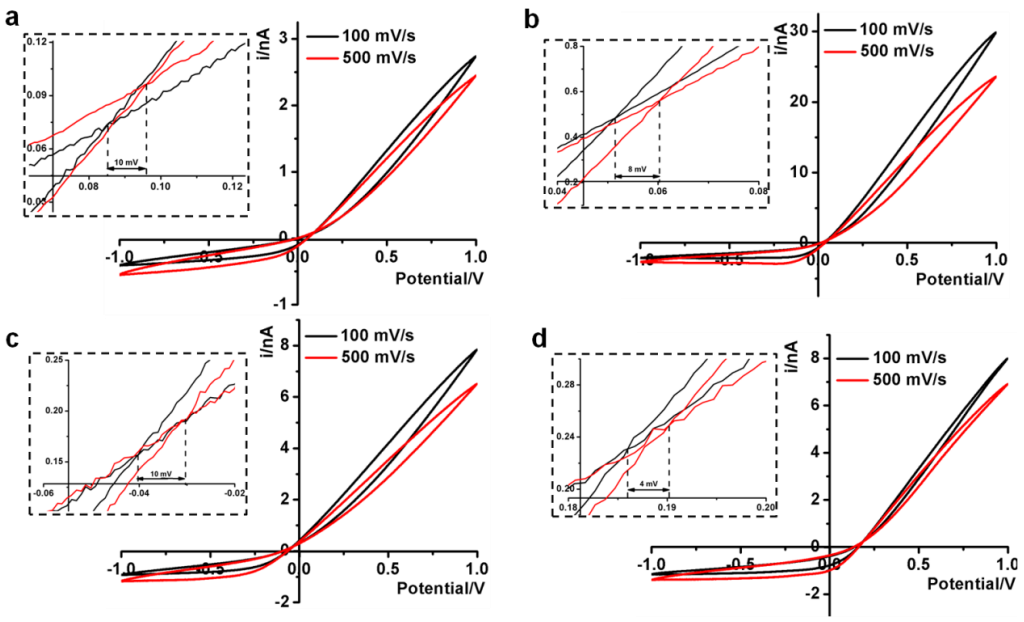

Fig. 3-6 Overlaid i-V curves of the 60-nm nanopipette in different tip:bulk concentration combinations at 100 mV/s and 500 mV/s scan rates. a) 1:1 b) 25:25 c) 1:25 d) 25:1. The insets show the zoom in around the cross point. The largest difference in cross point potential is around 10 mV.

This non-zero cross-point is employed as a signature in the following discussions because it is stable and unique for each measurement system (Figs.3-5-Fig.3-6). At each scan rate, the I-V curves from multiple scans overlap with the variation in cross-point within 5 mV (the first or few segment/s are discarded to better present stable I-V responses). This variation is acceptable within experimental errors such as imperfect Ag/AgCl electrodes preparation, thermo agitation and external interference etc. The I-V features are also found independent of initial potential or initial scan directions. A small variation in cross-point potential could be observed at less than 10 mV at different scan rates employed in this report. This variation intensified at higher scan rates, which has been attributed to the charging and discharging of quartz substrate (through exterior

interfaces).[92] The effect is ignored in the following discussion because it is insignificant with regards to the trend discussed in this report.

3.3.3 Dynamic ion transport through a quartz nanopipette under asymmetric tip:bulk concentrations

Next we analyze the dynamic ion transport under a concentration gradient across the nanopore driven by an external bias. A series of I-V curves using a single nanopipette in asymmetric tip:bulk KCl concentrations are presented in Fig.3-7. The feature near the cross-points can be seen in the insets. Similar trends were obtained from different nanopipettes (Fig.3-8). Systematic studies using the same nanopipette eliminate the impacts by possible imperfection in nanodevice geometry, particularly the transport-limiting nanotip interior portion that could not be directly characterized. Because the nanopipette geometry remains constant in those measurements, geometric impacts can be deconvoluted. The approach enables direct correlation of the transport features with surface charge effects, which has been a long standing challenge to study due to the heterogeneous nature of surface charge distribution, particularly at nanoscale interfaces. As a reminder, surface effects are known to be significant and even determinant factors in the ion transport processes through various channel-type nanodevices.

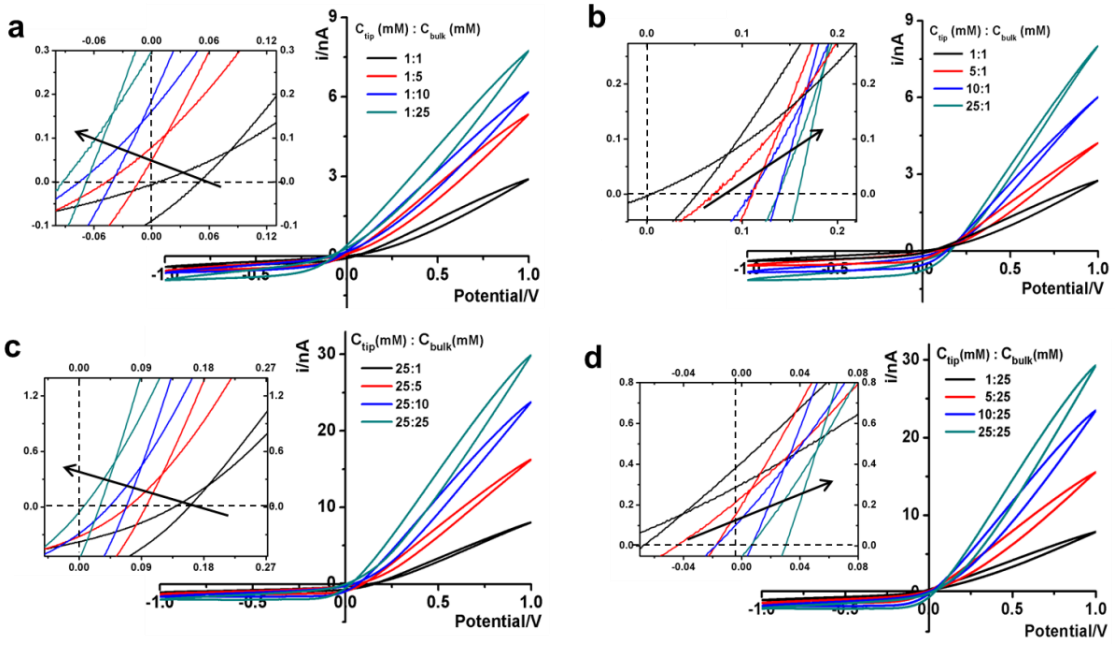

Fig. 3-7 Trends of I-V features in asymmetric tip:bulk KCl concentrations.
The I-V curves of the 60-nm-nanopipette in the denoted C_{tip}:C_{bulk} concentration combinations: **a)** common low tip conc. **b)** common low bulk conc. **c)** common high tip conc. **d)** common high tip conc. Scan rate at 100 mV/s. Inset shows the shift in the cross-point w.r.t. the origin (0,0). Each curve was collected after multiple scans until the last five repeated scans overlapped, affirming a stable concentration gradient being established.

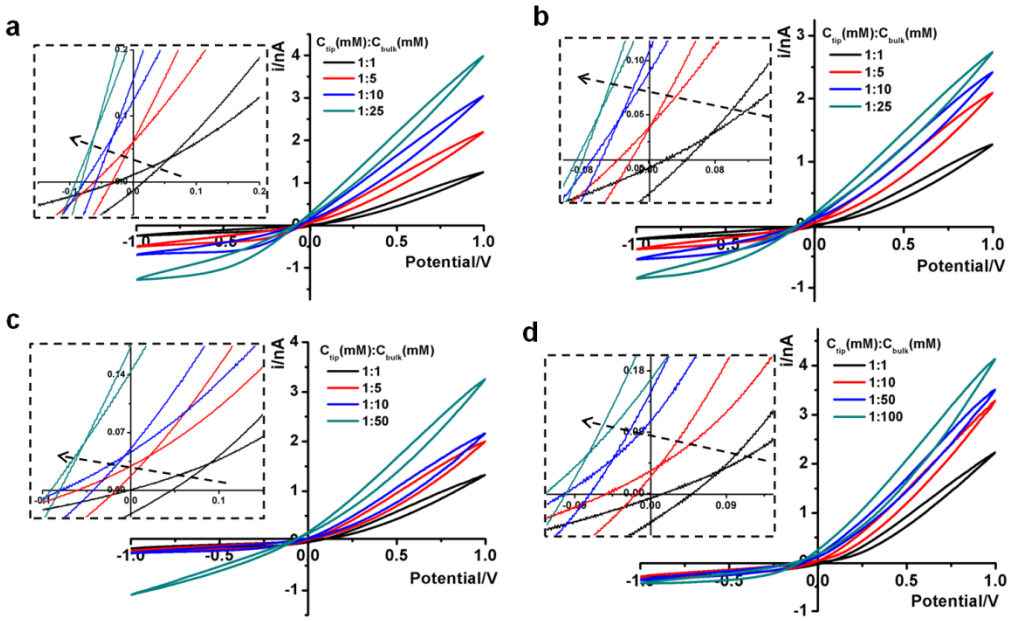

Fig. 3-8 The overlaid i-V curves of four different sized nanopipettes in asymmetric tip:bulk concentration combinations. a) 60 nm b) 80 nm c) 60 nm d) 30 nm-radius.

The cross-points of those systematic concentration combinations are summarized in Fig.3-9. Because the two Ag/AgCl wires are soaked in different KCl concentrations, unlike those in the same KCl solution, the potential drop at the two electrode–solution interfaces does not cancel each other and needs to be corrected. The net redox potential is described by Nernst expression (V_{redox}). The total bias at the cross-point ($V_{CPP(i\text{-}V)}$) therefore includes V_{redox} and V_{pore} (the potential drop across the nanopore) as expressed in Eq. 1. V_{pore} includes both surface field and concentration gradient effects discussed next.

$$V_{CPP\ (i-V)} = V_{pore} + V_{redox} = V_{pore} + \frac{RT}{F}\ln\frac{K_{sp\ AgCl}/a_{bulk\ KCl}}{K_{sp\ AgCl}/a_{tip\ KCl}} \quad (1)$$

in which the activity of Ag^+ (a_{Ag^+}) is approximated as concentration, which is inversely proportional to that of Cl^-. R is gas constant, T is temperature and F is Faraday's constant.

At each specific tip concentration, an increase in bulk concentration will cause V_{pore} (or the measured V_{cpp}) to shift toward more negative bias. At each specific bulk concentration, an increase of tip concentration will cause positive-shift of V_{pore}. The data also suggest that comparable concentration gradients induce similar shift magnitudes of V_{cpp}. At even higher concentration gradients, the cross-points could deviate from the trend presented in Fig.3-9 (Shown in Fig.3-10 a&b). The deviation might be associated with the challenges to establish stable and controllable concentration gradient, which is a prerequisite for this report.

With the increase of bulk or tip KCl concentrations, the current increase due to the increase of accessible charge carriers on either side of the transport-limiting nanotip region. The cross-point current is more sensitive to the tip concentration and to a lesser extent the bulk. This is because the measured current is primarily limited by a segment inside the nanopipette orifice. The current data at +/- 1V of each curve are listed in Table 1. Further current analysis requires surface charge parameters at the nanotip that are known to be heterogeneous and thus unavailable for individual nanodevices. This is being addressed in a combined experimental and simulation study underway.

Table 1 The current data at +/- 1V of each curve in Fig. 3 are listed in Table. The same color code represents the same combination.

C_{tip}/mM	C_{bulk}/mM	i_{+1V}/nA	i_{-1V}/nA	C_{bulk}/mM	C_{tip}/mM	i_{+1V}/nA	i_{-1V}/nA
1	1	2.9	-0.4	1	1	2.9	-0.4
	5	5.4	-0.6		5	4.2	-0.6
	10	6.3	-0.7		10	6.0	-0.8
	25	7.8	-0.9		25	8.0	-1.2
25	1	8.0	-1.2	25	1	7.8	-0.9
	5	16.2	-1.4		5	15.5	-1.3
	10	23.8	-1.7		10	23.5	-1.7
	25	29.9	-2.1		25	29.9	-2.1

3.3.4 Balance of diffusion and migration flux by zero current clamping

Under the low potential amplitude and other experimental conditions employed here, ion flux arises primarily from 1. diffusion determined by concentration gradient and 2. migration regulated by both applied and surface electric fields.[14,59,89] The measured current signals reflect the net ion flux limited by the nanotip region. Chronopotentiometry is employed next to elucidate the respective ion flux contributions by migration and diffusion. The applied potential is recorded over time till it reaches a stable value $V_{rev\ (i\text{-}t)}$, during which the measured current is clamped to zero. This corresponds to no net flux of charges through the pore. In other words, at zero current, the ion flux driven by the external bias balances that by the concentration gradient. As expected in symmetric tip-bulk concentration conditions, the diffusion potential V_{diff} is zero (within experimental error at few millivolts). Analogous to the cross-point potential analysis in I-V studies, the

reversal potential V_{rev} includes V_{redox} in addition to the diffusion potential as expressed in equation (2).

$$V_{rev\,(i-t)} = V_{diff} + V_{redox} = (t_+ - t_-)\frac{RT}{F}\ln\frac{a_{tip\,KCl}}{a_{bulk\,KCl}} + \frac{RT}{F}\ln\frac{a_{tip\,KCl}}{a_{bulk\,KCl}} = 2t_+V_{redox} \qquad (2)$$

This quantitative correlation is affirmed by the nice linear fitting of the measured V_{rev} versus theoretical V_{redox} shown in Fig. 3-12 (a). The V_{rev} values and representative V-t curves are included in Fig.3-11 and Table S2. From the slope, cation transference number is determined to be 0.69 for this nanopipette. Since ion selectivity is a significant parameter in membranes for i.e. desalinization, and broadly defined separation science and energy technologies, it is exciting for this analysis to directly characterize cation selectivity of a single nanopore experimentally. Because K^+ and Cl^- mobility is comparable, no diffusion potential is expected in bulk solution (transference number at 0.5 each). The large cation transference number reflects surface electric field effect, which induces asymmetric cation and anion diffusional flux and makes this nanodevice cation-selective. The correlation in equation (2) is further validated by the results from different nanopipettes analyzed in Fig.3-13. The variation in those t_+ values suggests heterogeneous surface charge effects of individual nanopipettes.

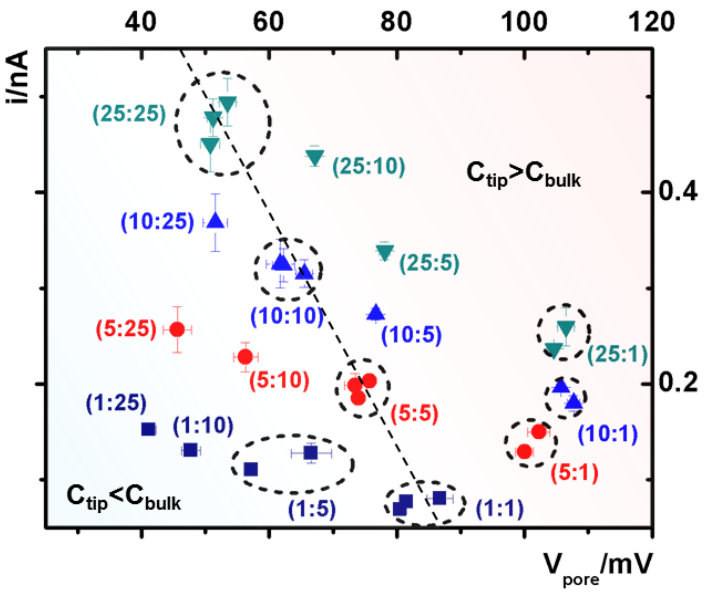

Fig. 3-9 Analysis of potential-corrected cross-point under designed tip:bulk concentration gradient combinations.

Error bars on each point show the standard deviations from five repeated scans under each condition. Between each asymmetric concentration measurement, symmetric ones with the same tip concentration were measured to validate the efficacy in loading and replacing the solutions, particularly inside the tip. Data from repeated measurements in the same concentration combinations (both symmetric and representative asymmetric) are circled to highlight the reproducibility of the measurements.

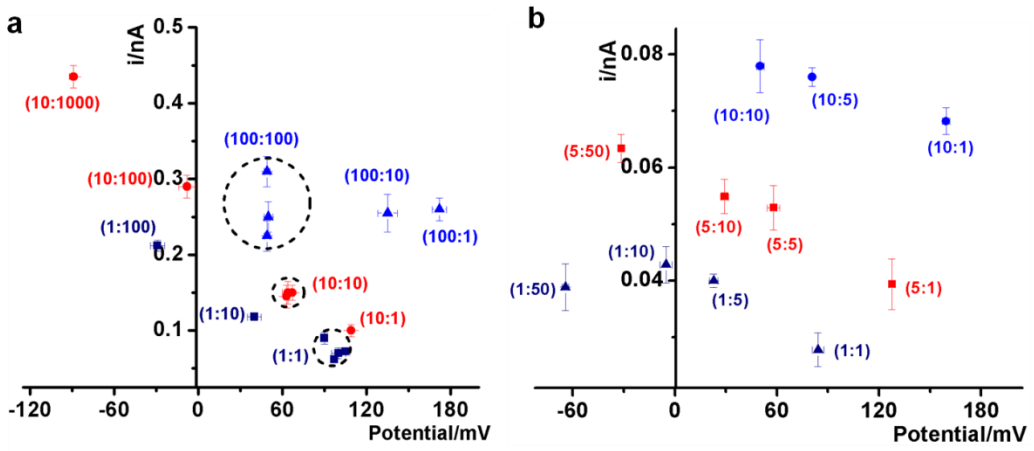

Fig. 3-10 Analysis of cross point positions of a) 40 nm and b) 60 nm-radius nanopipette in different tip:bulk concentrations. Redox potential has not been corrected. Note the (10:1000) data in panel a) follows the trend while the (1:50) data in panel b) deviate from the general trend. Both data points have greater concentration gradients then those employed in the main analysis.

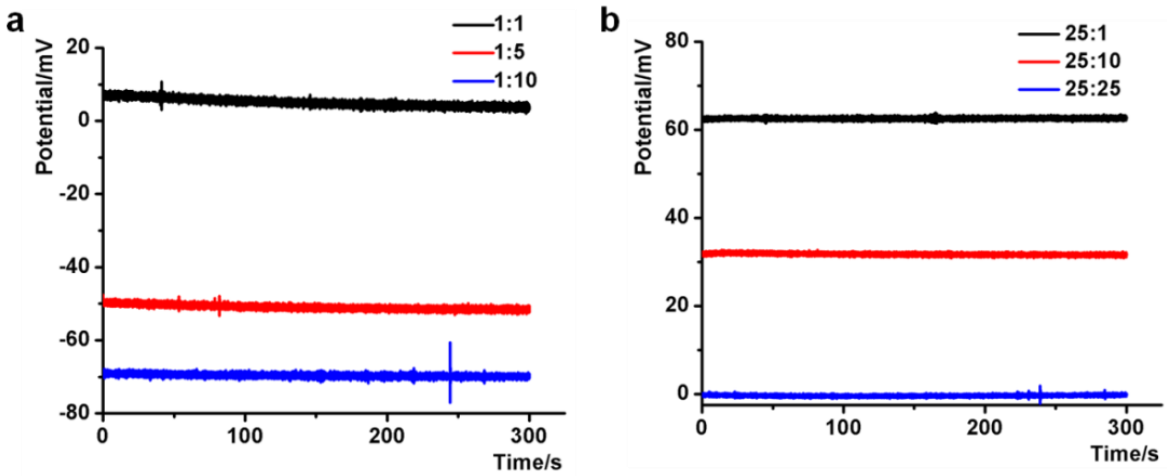

Figure 3-11 Chronopotentiometry measurement of the 60 nm nanopipette with a) 1 mM and b) 25 mM KCl tip concentration with different bulk concentration that show stable potential-time traces.

Table 2 Analysis of the cross point potential (V_{CPP}), measured zero-current potential (reversal potential V_{rev}) and calculated surface effective potential (V_M). The $V_M = V_{CPP} - V_{rev}$. At each tip concentration, the error is within 5 mV range at different bulk concentrations in general.

C_{tip}/mM	C_{bulk}/mM	V_{CPP}/mV	V_{rev}/mV	V_M/mV
1	1	59	5	54
	5	3	-52	55
	10	-17	-70	53
5	1	108	63	45
	5	51	1	50
	10	21	-22	43
10	1	129	88	41
	5	79	32	46
	10	49	4	45
25	5	95	63	32
	10	65	33	32
	25	31	0	31

In our earlier studies based on conical nanopore platform in symmetric concentrations, the effective transmembrane potential V_M was found to depend on the electrolyte concentrations by a square root function. In the expression shown as the last portion in equation (3), analogous to the Debye length description in classic double layer theory, V_0, A, V_e correspond to surface potential inside nanotip, a constant that is temperature dependent, and non-ideal factors associated with measurements respectively.[23]

$$V_{CPP\,(i-V)} - V_{rev\,(i-t)} = V_{pore} - V_{diff} = V_{M\,(i-V)} = V_0 \exp\left(-\frac{C_{KCl}^{1/2}}{A}\right) + V_e \quad (3)$$

A correlation of I-V and I-t measurements by equation (3) will reveal nanointerface parameters such as surface potential (V_0). Subtraction of V_{redox} from both types of measurements reveals the potential drop at the nanotip region (bulk-to-tip across the quartz membrane). At each tip concentration, V_M from symmetric tip:bulk concentrations matches that by the elimination of the diffusion potential in asymmetric concentrations (i.e. at 5 mM tip conc., 108 mV – 63 mV = 45 mV at 5:1 ratio matches the 50 mV at 5:5 ratio within ± 5 mV). The analysis suggests that the tip concentration plays more significant roles in the transport measurements (data listed in Table 2). The linear correlation in Fig. 3-12 strongly supports the correlation of equation (3). The scattering at different bulk concentrations is attributed to the variation of local concentration gradients in different measurements. The concentration range in this study is adopted to ensure stable and reproducible concentration gradients. With predefined salinity and salinity gradient, this analysis offers the full picture of dynamic ion transport across an asymmetric nanopore influenced by diffusion and migration.

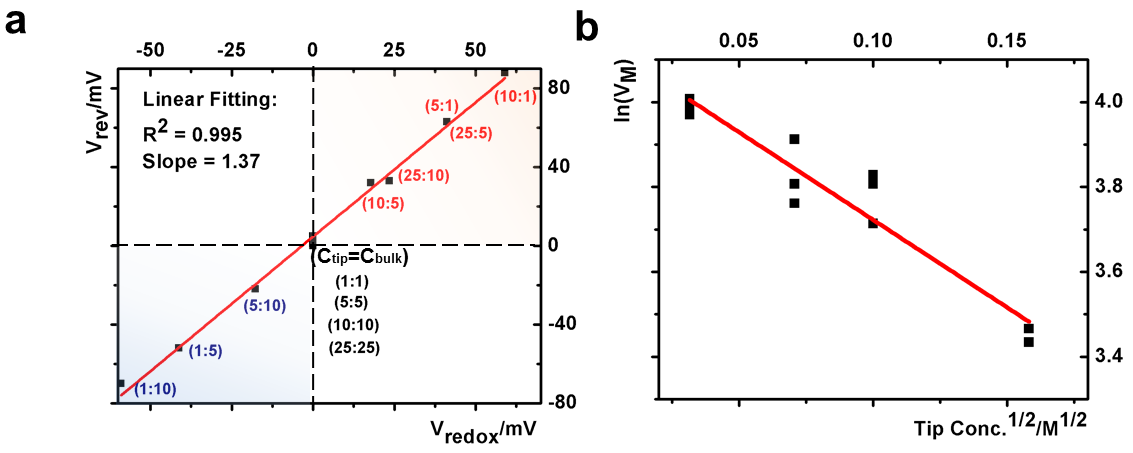

Fig. 3-12 a) Correlation between the measured reversal potential and the redox potential. b) Correlation between the corrected transmembrane potential with square root electrolyte concentration.

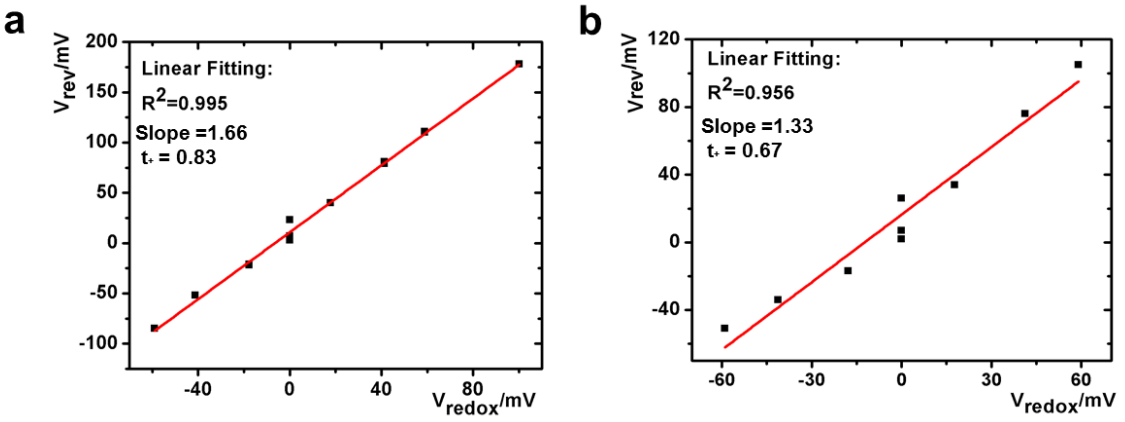

Figure 3-13 Linear correlation of measured reversal potential V_{rev} with calculated redox potential V_{redox} from two different nanopipettes. a) 40-nm radius b) 60-nm radius.

3.3.5 Implications on selective ion transport and history-dependent energy conversion at nanointerfaces

Three key factors have been correlated in this time-dependent ion transport analysis: the applied electric field, surface electric field, and salinity gradient. Each cross-point is at a unique balance of the three factors in the corresponding current-potential analysis.

3.3.5.1 Selective ion transport and ion pumping

The intrinsic ion selectivity (no bias applied) of a negatively charged nanopore can be characterized by the aforementioned analysis of cation transference number. At a bias more negative than the cross-point potential, low conductivity zone is established. The depletion of anion transport makes this zone highly cation selective due to negative surface charges. This is supported by cation transference number approaching unity in earlier simulation and experimental studies. [93-95] The high conductivity zone, at the bias more positive than the cross point, is associated with high ionic strength and thus a

decrease in ion selectivity. [93-95] Therefore, high conductivity region is more favorable for energy conversion applications (high power) rather than separation.

To relay to the ion pump concept, the cross-points in Fig.3-9 can be divided into three categories: $C_{tip} = C_{bulk}$, $C_{tip} < C_{bulk}$, and $C_{tip} > C_{bulk}$. The transport of cation is considered because it constitutes the majority of the measured current signal. For $C_{tip} < C_{bulk}$, cations are pumped against their concentration gradient at low conductivity side, driven by applied potential but inhibited by surface potential. On high conductivity side, cations move along the concentration gradient, and thus no pumping effect. For $C_{tip} > C_{bulk}$, cations are pumped against their concentration gradient at high conductivity side, driven by applied potential and facilitated by surface potential. At low conductivity side, no pumping effect is expected. Four representative scenarios illustrate the physical picture of the corresponding transport processes (Fig.3-15). For applications that require anion selectivity, positively charged surfaces can be created, by i.e. chemical modification, to enable favorable transport of anion over cation. The same principles apply to different salinity gradients.

3.3.5.2 History-dependent energy conversion at nanointerfaces

Cross-point signature At the cross-point, steady-state ion flux is established by the three factors: the current and potential at the cross-point indicate the external power/energy input required to balance the surface electrical field effects, plus the salinity gradient if adopted. Thus, the product of I*V at the cross-point represents the natural capacity of the employed nanointerface for the energy conversion process. The I(t)*V(t) at cross-point is referred as power P_{cpp}. To evaluate the energy conversion or

power in conventional electronic circuits, open-circuit-potential (OCP) and short-circuit-current (SCC) are routine analysis because the triangular area in the I-V plots represents the max power (for a simple resistor load, $P=I*V=I^2*R=V^2/R$). Similar analysis has been adopted to evaluate the maximum power of various nanochannels under salinity gradient.[66,81,83] It is important to realize that $P=I*V=0$ in either OCP or SCC conditions ($I_{V=0}$ times $V_{I=0}$ evaluation). Therefore, caution should be taken in the nanopore systems because their resistance and capacitance vary and depend on the transport dynamics. Therefore, we propose P_{cpp} as a parameter with more rigorously defined physical meaning in the evaluation of transport related energy conversions at nanointerfaces, especially in systems with prominent rectification and hysteresis.

Power analysis and comparison Importantly, P_{cpp} values are comparable in magnitudes with the products of $I_{V=0}$ times $V_{I=0}$ for different nanopipettes, and comparable in general with those in related literature for power generation under salinity gradients (Table 3). Unlike those literature studies performed in high pH conditions to induce higher surface effects, our measurements were performed in ambient pH to avoid the introduction of different types of ions that complicates the mechanism elucidation. Therefore, we expect further enhancement in the already-impressive power of our system at higher pH and/or high salinity gradient conditions.

Hysteresis in the charging-discharging kinetics History-dependent energy conversion is illustrated in Fig. 3-14. The following discussion is focused on high conductivity states that are better suited for energy applications. In reference to the volumetric conductance, drastic surface effects can be quantified at different time or bias domains. For example, at 0.60 V, $I(t_b)$ is larger than $I(t_f)$ due to the longer period during

which larger surface effects accumulate (sustained contribution by E_s). Similarly, both forward and backward currents are lower at higher scan rates due to less surface enhancement over shorter time at the same potentials. This surface enhancement functions regardless of salinity gradients. Given the P_{cpp} describes the intrinsic capacity of individual nanostructures for power generation under salinity gradient and establishes the physical meaning of such power generation under an external bias, further enhancement by the nanointerface in the power generation is anticipated if a positive bias were applied. The concept is analogous to the gain effect in field effect transistors. Further, the forward and backward scans correspond to charging and discharging of the nano-supercapacitor respectively. The hysteresis therefore suggests a delay in the charging (forward scan) as well as discharging (backward scan) driven by the external potentiostat. In other words, asymmetric nanopore structures and local surface electric field effects will alter the kinetics of energy conversion. Our analysis suggests that, theoretically, the time constants of the energy conversion could be tuned by engineering nanointerfaces to achieve desired power input-output for specific energy storage, power generation and other related applications.

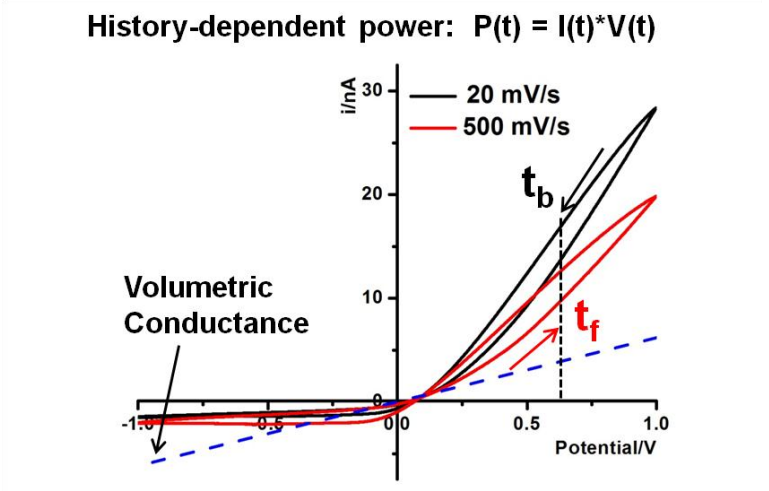

Fig. 3-14 History-dependent power generation of the 60-nm nanopipette in 25:10 tip:bulk concentrations at 20 mV/s and 500 mV/s.

Volumetric conductance is estimated from tip concentration volumetric ohmic behaviors (blue dash line). The arrows near the current curves indicate the direction of the sweeping bias. Forward and backward scans are defined as away and toward the cross-point respectively.

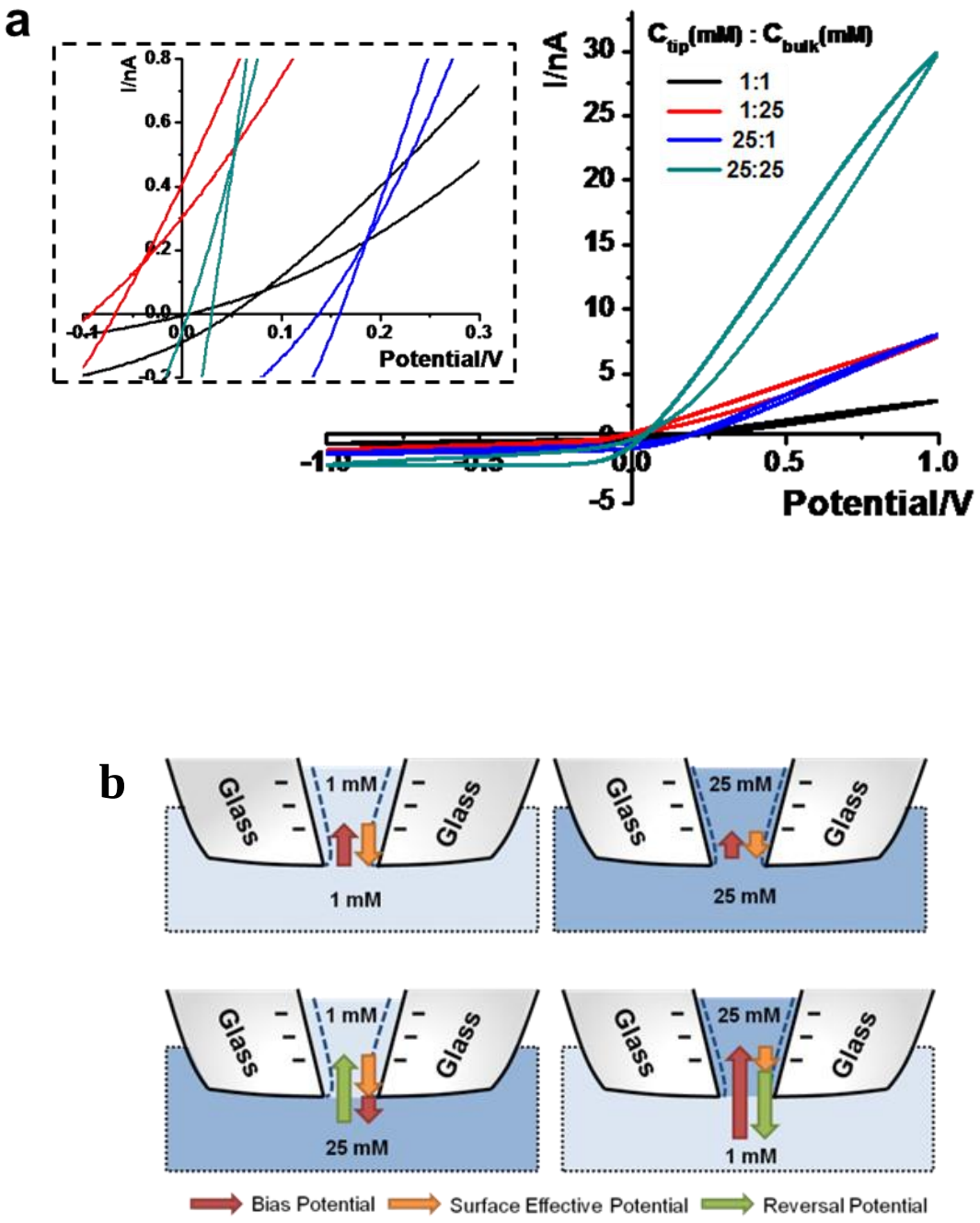

Figure 3-15 Illustration of the ion transport governed by the three key factors. a) I-V curves of the 60-nm nanopipette in four respresentative concentration combinations. Enlarged view was shown in the inset. b) Four representative schemes of nanopipette with asymmetric 1:1, 1:25, 25:1 and 25:25 tip-to-bulk concentration gradients were shown. The dashed lines around glass surface show the thickness of double layer. The arrows were drawn based on real experimental value.

With symmetric tip-to-bulk setups, no diffusion potential is established. At cross point potential, the applied electric field balances the surface field effects, which is larger in 1:1 than that in 25:25 mM due to less effective electrostatic screening. After the introduction of an additional concentration gradient across the nanopipette, the applied potential needs to balance both surface potential and diffusion potentials at the cross point. At 25:1, even though the transmembrane potential is lower because the tip concentration is higher (compared to 1 mM inside), the concentration gradient and surface electric field have cumulative impacts on the ion flux at the transport limiting region inside the nanopipette. A bias magnitude equal to the sum of diffusion potential and surface potential is required to establish the cross point. Therefore, the cross point shifts toward more negative polarity if $C_{tip} < C_{bulk}$ and shifts toward more positive polarity if $C_{tip} > C_{bulk}$. Similar rationale can be applied to other concentration combinations or the transport of cations as main charge carriers and anions separately.

Table 3 Comparison of power generation from different nanopipettes with related literature under comparable experimental conditions**.**

Our Results	**Nanodevice platform**	C_{tip}(mM): C_{bulk} (mM)	Power Estimation/pW				
			$P_{cpp} = V_{cpp} \times I_{cpp}$	$P = V_{i=0} \times I_{V=0}$	$P(t) = V(t) \times I(t)$		$P_{surface}$
1 (data reported in manuscript)	60-nm nanopipette	10:1	18.8	4.0	F(0.6 V)	2064	1200
					B(0.6 V)	2250	1400
2	60-nm nanopipette	10:1	7.0	3.2	F(0.6 V)	786	-67
					B(0.6 V)	930	77
3	40-nm nanopipette	10:1	12.2	8.4	F(0.6 V)	594	25
					B(0.6 V)	720	151
4	30-nm nanopipette	10:1	4.5	1.7	F(0.6 V)	1032	463
					B(0.6 V)	1092	523
Literature							
5	41-nm polyimide conical nanopore[66]	10:1 pH 10.5	N/A	10.9	N/A		
6	40-nm Boron-Nitride nanotude[96]	10:1 pH 11	N/A	15.2	N/A		
7	Less than 10 nm polymer (COO-terminated) nanopore[81]	100:10	N/A	15~20	N/A		

Here, P_{CPP} represents the cross point power generation. $P_{CPP} = V_{CPP} \times I_{CPP}$. P(t) represents the total transient power at a specific time. $P(t) = V(t) \times I(t)$.

VC refers to volumetric contributions (ohmic conductance by nanogeometry and solution resistivity). P_{VC} represents the power without contribution from surface charge, which is mainly determined by tip concentration. $P_{VC} = V(t)^2 \times G_{tip}$. G_{tip} is the tip solution conductance.

Note: the contribution from volume conductance to the overall conductance can be estimated from Fig.3-3 in main text. Ignoring it in the above analysis of P_{VC} does not affect the general outcome of our analysis and has been confirmed by the analysis with square root tip*bulk.

$$G_{tip} = \frac{1}{R_{tip}} = \frac{1}{\rho_{tip}/\pi r \tan\theta + \rho_{tip}/4r} \quad , \qquad P_{vc}(t) = V(t)^2 \times \frac{1}{\rho_{tip}/\pi r \tan\theta + \rho_{tip}/4r} \quad .$$

$P_{surface}(t)$ is the power generation contributed from the surface at a specific time t. $P_{surface}(t) = P(t) - P_{VC}(t)$. Forward (F) and backward (B) refer to the bias V(t) being scanned away and toward the cross point respectively. Therefore, at the same bias, two current values are listed as the consequence of the hysteresis effects.

#1~#4: Cross point power generation: $P_{CPP} = V_{CPP} \times I_{CPP}$. V_{CPP} has been calibrated by subtraction of electrode redox potential. For $P = V_{i=0} \times I_{V=0}$, here $V_{i=0} = V_{rev} - V_{redox}$. V_{rev} is obtained while holding current to be 0 A. $I_{V=0}$ is obtained while holding the potential to be 0 V. Original data of nanopipettes 2-4 were included in Fig.3-11 and Fig.3-12. All data were collection under ambient pH. It is important to point out that the reported

power in our system will be much higher at higher pH as reported in the references listed below.

#5: The data were copied directly from the literature Table.1 in ref. 1 with the same 10:1 asymmetric concentration. The solution pH was adjusted to 10.5 to increase surface charge effects, unlike ambient pH employed in other listed data.

#6: The current data $i_{V=0}$ and conductance data G were obtained directly from Supplementary Tab.I in ref. 2 with the same 10:1 asymmetric concentration. $V_{i=0} = I_{V=0}/G$ and was corrected from the electrode redox potential.

#7: The power data were read directly from Fig. 5 in ref. 3 while the asymmetric concentration is 100:10.

3.4 Conclusions

To summarize, time-dependent current potential features of individual conical nanopipettes are studied through which fundamental understanding in dynamic ion transport at nanoscale interfaces is established. Employing salinity gradient across a conical quartz nanopipette, hysteresis in the ion transport current with respect to a stimulating alternating electrical field is characterized by a non-zero I-V point and pinched I-V loops. The product of I-V, i.e. power at the unique cross-point is shown to be a more accurate and meaningful signature to characterize the dynamic ion transport or energy conversion at individual nanodevices. The hysteresis effect in I-V measurements has significant implications on the charging-discharging kinetics of energy devices such as supercapacitors. Further, the conversion of salinity gradient into electrical energy, or vice versa, on asymmetric conical nanopore platform is demonstrated to be enhanced

drastically by an intrinsic surface electrical field. The findings suggest exciting opportunities to advance energy, separation and other related applications using broadly-defined channel-type nanodevices. The theoretical foundation and analysis methodology are universal and generalizable to other structurally-defined nanoporous materials and nanodevices, and thus believed applicable in broad energy and separation applications.

4 INSULIN SINGLE CRYSTAL NUCLEATION AND GROWTH BY ACTIVE ELECTROCHEMICAL CONTROL OF MASS TRANSPORT THROUGH SINGLE NANOPIPETTES

4.1 Abstract:

Protein crystallography provides three-dimensional (3D) molecular structure information that is important to understand their functions. However, fundamental research on nucleation mechanism and technical developments to control crystal formation continue to attract extensive attention after centuries of progress in materials science and biology. Relying on very powerful technique X-ray crystallography, obtaining diffraction quality protein crystal is still a bottleneck and one of the most challenging aspects in protein crystallography. Conventional methods are empirical trial-and-error based which are intrinsically material consuming and labor and time extensive. New technology and smart materials are being developed to reduce the time needed via high-throughput approaches, to better control the solution mixing via micron-to-nanometer scale devices. Active control of the crystal formation process that is generalizable for different materials has not been established. Here we apply our fundamental understanding of the mass transport dynamics at nanometer scale to control the earliest stage crystal nucleation and continued crystal growth. We show by programming electric current-potential through single quartz nanopipettes, the formation of single insulin nuclei is spatially and temporally monitored and manipulated. Further crystal growth around a single nucleus is similarly controlled and monitored. The nucleation kinetics and crystal growth rate are demonstrated to be controlled by the applied potential and current. In situ optical imaging of crystal formation process reveals

different assembly morphologies near the nanotip that can be correlated with characteristic current disturbances as signatures to the crystal formation.

4.2 Introduction:

Protein crystallography plays a very important role in structure biology and drug discovery since it elucidates the macromolecule structure for a better understanding of biological functions. Protein crystallization has a long history back to the observation of hemoglobin crystals in blood preparation in 1840. The significance of protein X-ray crystallography was better recognized after the first X-ray photograph of protein pepsin[97]. However, protein crystallization has been regarded as a real black art rather than science for a long time due to a lack of fundamental understanding and poor control. There are general strategies, but the conditions to obtain macroscopic diffraction-quality protein crystals are variables for different analyte systems. The requirement of trial-error screening of a variety of empirical parameters has been the bottleneck for many research projects in requiring extra materials and person effort.

High-throughput methods have been developed and adopted in most structural biology research to expedite the protein crystal growth. Multiple parameters, albeit still trial-and-error screening, can be tested in parallel, i.e. using multi-well devices to save time. Compared to conventional methods, it is a significant improvement for each unit cell to function with smaller volume in current high throughput methods. Given it only takes one high quality crystal for the structure determination, a predictable theory or a generalizable method within a single unit cell would greatly reduce the amount of analyte molecules needed.

Besides the fundamental research in nucleation that remains a hot topic in materials science and biology, better design in equipment and technique development for more efficient high-throughput screening are in under constant progress. One way to use protein sample more efficiently is further device miniaturization by adopting micro/nanofluidic systems.[98-102] Instead of microliters in either substrates or dispensing volume, nanoliters of fluids can be dispensed. For example, microfluidic cartridges preloaded with nanoliter plugs of reagents have been designed to screen the parameters or conditions for crystallization using only nanoliter plugs of reagents per reaction.[99] A robust microfluidic method with scalable metering can setup144 parallel reactions with 10 nL protein samples each.[98] Compared to conventional screening techniques, microfluidic devices can screen more conditions using two orders of magnitude less protein samples.[98]

For a crystal to form, it usually goes through two sequential stages – initial nucleation (formation of a nucleus larger than a critical size) and further growth. An energy barrier has to be overcome to nucleate. Once the critical size is reached, normally at tens nanometers, further growth can be a downhill energy process under appropriate solution conditions. These two processes are generally coupled together and difficult to differentiate. A phase diagram is often necessary in protein crystallization to determine under saturated and supersaturated zones (not in spatial regime; in phase diagram defined by chemical and environmental parameters). The supersaturated zone can be further divided into the metastable zone, labile zone and precipitation zone based on ensemble kinetics and observations.[103] In the metastable zone, nucleation will not occur spontaneously but further growth of a preformed (or introduced) crystal embryo can be

maintained. The labile zone is the next supersaturated zone in which the seed will form spontaneously and grow. However, the labile zone is usually very narrow and hard to find. In precipitation zone, the kinetics of both nucleation and further growth will be fast that leads to the formation of amorphous precipitates or disordered structures.[103]

Heterogeneous nucleation can be initiated with the introduction of smart materials to facilitate crystal nucleation by overcoming energy barrier in the metastable zone. An array of lipid patches at micrometer dimensions has been printed into different shapes by nanolithography method. Due to adsorption of protein molecules on to the lipid layers in the array, these lipids will enrich the target protein locally to overcome the energy barrier for nucleation.[104] Analogous to traditional seeding methods such as using horse hair, molecular imprinted polymer thin films with nano/micron-patterns have been developed as novel seeding materials.[105] Another interesting seeding method for membrane protein is the lipidic cubic phase.[106] Due to the hydrophobic surface and anisotropic orientation, crystallization of vulnerable membrane protein is very difficult and involve extra step of detergent solubilization. Lipid polymorphism cubic phase forms diffusional space and allows membrane protein diffuse while keeping original conformation.[107] Porous nucleating agent materials, such as bioglass, have also been adopted to overcome the energy barrier for nucleation in metastable zones.[108] The mechanism of facilitated nucleation is similar for those smart materials/strategies, which is to enrich target protein concentration locally by either specific protein-template interaction or size selectivity via designing specified pore size suitable for the target protein. The energy barrier for nucleation is overcome at small domains within local space rather than the whole solution.

X-ray sources from synchrotron offer higher intensity over in-home sources that are better suited to analyze microcrystals or crystals with large unit cells. The advantages are highly favorable for protein complexes and membrane protein that is very difficult to crystallize. The potential drawbacks include higher beam intensity induced X-ray radiation damage and the requirements for sufficient micron sized crystal. To address this concern, nanocrystallography is developed after the first serial femtoseconds protein nanocrystallography experiment [109] that demonstrates the capability to solve multi-protein structures[110-112]. Femtosecond pulses of X-ray free electron laser were used to collect snapshots from a fully hydrated stream of nanocrystals instead of conventional one single crystal. The promising technique is at its infancy facing many challenging problems such as protein preparation due to the low hit rates and high protein consumption as a stream instead of a single crystal. Moreover, a high concentration of salt in nanocrystal solution might block the liquid jet nozzle as well.

The nucleation or growth of protein crystals under the influence of electric field[113-118], magnetic field[119], ultrasonic irradiation[120,121] and a combination of those factors[122,123] have been extensively studied. Given both nucleation and growth involve the transport and assembly of analyte molecules at individual sites of embryo formation, the solid state nanopore/nanopipettes are promising platforms with unique advantages. Those novel ion transport dynamics discovered at nanoscale discussed in the early chapters provide unprecedented capability to control and regulate the transport of ionic species for enrichment in concentration. The results in this chapter demonstrate that kinetically controlled nucleation and growth processes enable greater temporal and spatial control of protein crystallization previously inaccessible.

Experimentally, we adjust the pH of the insulin solution to form metastable solution and tune the transition between precipitation zone and metastable zone dynamically by a spatially confined nanotip with precipitant inside. In this metastable phase zone, no spontaneous nucleation will occur but crystal growth will be supported if nuclei were available. At bulk ensemble level, it is not favorable for nucleation but considered the ideal region for crystal growth after nuclei formation. The metastable region is selected to avoid spontaneous microcrystals/precipitates formation in precipitation zone or dissolution of synthesized nuclei in the under-saturated zone. The energy barrier for nucleation is overcome by the delivery of precipitating reagents actively controlled by external electric field: the in-situ regulated concentration enrichment or solubility gradient triggers nuclei formation at the nanopipette region. Electric current signal and optical imaging provide feedback to adjust the parameters of different potential waveforms for nuclei growth into macroscopic single crystals.

4.3 Experiment:

Instruments:

P-2000 nanopipettes puller, Sutter Instrument Co.

Quarts Glass Capillary with Filament, O.D.:1.0 mm, I.D.:0.7 mm, 7.5 cm length, Sutter Instruments Co.

Gamry Reference 3000, Gamry Co.

Axopatch 200B Amplifier，Molecular Devices

Olympus Microscope, Dino-line eye eyepiece 1.3 Mp Camera

Preparation of nanopipettes:

The pulling parameters of the nanopipettes are as follows: Heat: 70, Filament: 4, Velocity: 60, Del: 150, Pull: 120. The nanopipettes were loaded with 1 M HCl and centrifuged for 20 min at 4600 rpm.

Chemicals:

Bovine insulin was purchased from Akron Biotech and used directly without further purification. ($ZnCl_2$: Sigma-Aldrich, Anhydrous Citrate Acid: Sigma-Aldrich, Sodium hydroxide pellets: J.T.Baker, Hydrochloric Acid: Fisher Scientific)

Insulin solution:

10 mg Insulin was dissolved in 8 mL 0.02 M HCl. 1 mL 0.1 M $ZnCl_2$ and 1 mL 2 M Citric Acid was added to the solution. The solubility of insulin is pH dependent with a PI around pH 5. The pH of 5 mL solution was adjusted first by 8 M NaOH until the formation of a white cloud, and continues adding 8 M NaOH until the white cloud fully dissolves, at which point the solution pH is 7.9. This near-saturated solution is used as a stock that remains stable without precipitation over three months.

The pH to prepare protein solution in the metastable zone is screened next. The stock solution will become oversaturated if the pH is lower, i.e. become metastable. A series of the stock insulin solutions, each containing aliquot of 200 uL, were added in small PCR tubes. Different amounts of hydrochloride acid were added to decrease the pH at ca. 0.05 pH unit intervals. With too much acid added, the solution will form micro seeds faster in 2 hrs at ca. pH 7.2. At ambient amount, a solution remains clear in a few days that are best suited and used in the following studies (normally around pH 7.6). For abbreviation, we refer to them as saturated insulin solutions. In summary, the goal is to

screen out the solution in which 1. an embryo will form if the pH is lowered; 2. the seed will grow spontaneously over time; 3. the solution will not self-nucleate in a few days. Those conditions are desirable for method development rather than the requirements for applications after the method is established.

Experimental Setup:

Glass slides were glued on top of an ITO glass slide as sidewalls with a 1 mm slit channel for quartz pipette insertion. The wax was melted via heating and applied on top of the glass slides around the slit channel to contain the protein solution with scalable dimensions. The protein solution is in contact with the wax wall between the top cover glass and bottom ITO glass. A quartz nanopipette is inserted directly into protein solution either manually or with a micromanipulator. The evaporation is confirmed negligible based on the volume retention during these experiments.

4.4 Results and Discussion:

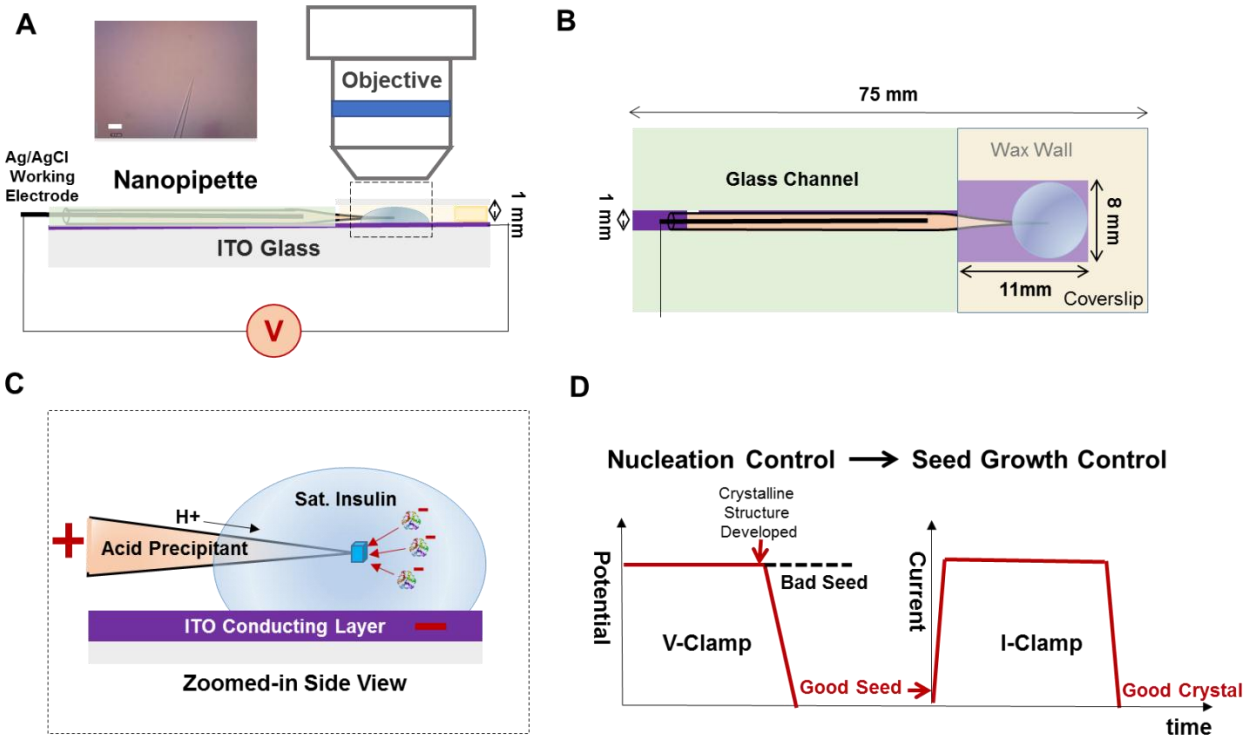

Fig. 4-1 A) Side-view of the experimental setup. A nanopipette is inserted in a sat. insulin solution droplet which is sealed in a wax reservoir on top of an ITO glass slide. The white scale bar in the optical microscope image is 10 microns. B) Top view of the slide setup with dimensions. Graphs are not drawn to scale. C) Side-view experimental design A. Note the bias is applied between a Ag/AgCl wire inside the quartz capillary and the conductive ITO layer. D) Sequential processes of the nucleation control and the growth control of a single crystal formation.

The experimental setup is shown in Fig.1 A. A nanopipette loaded with 1 M HCl acid as the precipitant was inserted into a sealed compartment with 50 uL saturated insulin solution. An Ag/AgCl electrode was inserted inside the long shaft of the nanopipette from the other end, serving as a working electrode while the ITO glass served as a counter electrode. The crystal formation process was monitored optically under an upright microscope continuously. Designed potential waveforms were applied across the nanopipette to actively tune the materials exchange between the interior acid

and exterior protein solutions. Without applying any potential externally, diffusion under the concentration gradients of different species will govern the mixing process, which is passive and cannot be adjusted once the two solutions are in place.

Since the isoelectric point of insulin is around 5, insulin molecules are negatively charged in pH 7.6 exterior solutions. To initiate nucleation process, as illustrated in Fig.1 C-scheme, a positive potential was applied. Protons will migrate toward the outside of the nanopipette tip while negatively charged insulin molecules are driven toward the nanopipette tip region under the applied electric field. A pH gradient will be established across the nanopipette tip region, primarily outside of the tip due to the higher mobility of protons compared to larger protein molecules. A solubility gradient, lowest near protein isoelectric point, would be established accordingly. The outside solution near the nanotip will make the transition from saturated/stable to metastable even precipitating zones depending on specific conditions. Accordingly, insulin molecules will aggregate, crystallize or precipitate at this spatially confined domain depending on the transport kinetics.

The process to obtain a good crystal is illustrated in Fig.4-1 panel D. A constant DC potential (bias) is applied, i.e. V-clamping, at the beginning to initiate the molecular assembly and nucleation. Once a characteristic electric current response or optical feature is observed indicating the formation of crystalline structures at the nanopipette tip, the applied potential is decreased immediately to reduce the rate of mass transport, or to avoid poor assembly/growth or amorphous precipitation. Afterward, a constant current is applied, i.e. i-clamping to control the grown rate and thus the crystal quality. In-situ

monitoring and active control of initial nucleation and subsequent growth are discussed separately in the following sections.

4.4.1 Nucleation Control

4.4.1.1 Constant Potential Nucleation Control

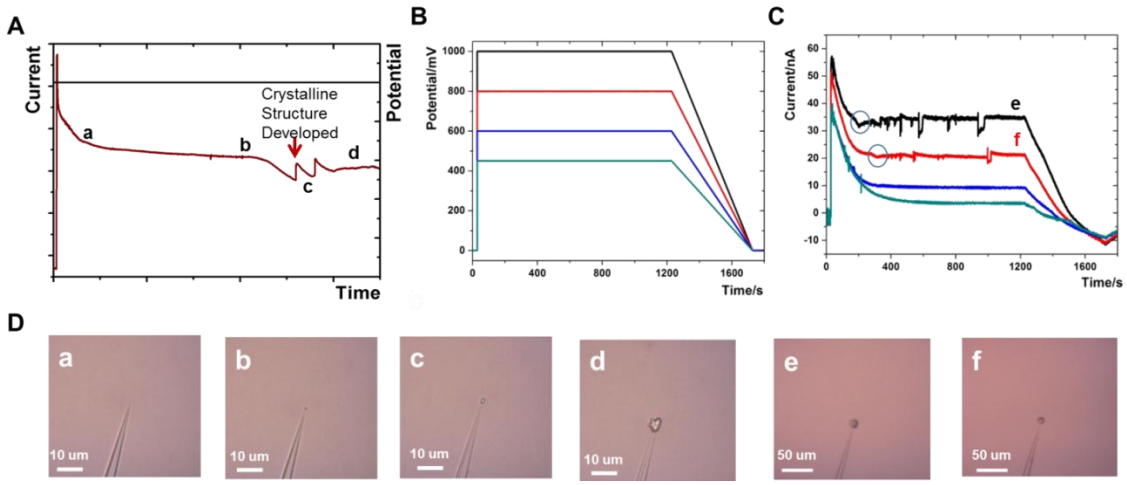

Fig. 4-2 A) Representative of current responses (red) over time under a constant applied potential (black) for nucleation control. B) Different profiles of applied potential. C) Corresponding current responses from a 4-nm-radius nanopipette. The circles indicate the transformation from the dark dot to a bright structure. D) In situ bright field imaging during nucleation process. The bright field images (a-d) were taken at the points labeled in panel A. The scale bar is 10 um. The images of e&f show the crystal seed formed at the nanopipette tip after the 1000 mV program and 800 mV in Panel C. The scale bar is 50 um.

Fig. 4-2 A shows representative i-t features during the initial period of crystallization under a constant applied potential. Four characteristic images are shown in Fig. 4-2 D. Stage a represents the establishment of pseudo-steady-state under a constant applied potential. The initial decrease in current is attributed to the consumption of protons with an exterior buffer solution that result in a significant decrease of charge carriers at the signal limiting nanotip region. The image shows the formation of a small dark spot right at the tip of the nanopipette. Unfortunately, our optical resolution is

insufficient to resolve any fine structures the black dot may have. Its dimension is estimated to be hundreds nanometer based on diffraction limit of visible light. It is important emphasizing that this dark sphere can form and disappear reversely by applying or removing/reversing the applied electric field. The reversibility of the dark spot formation suggests either loosely assembled protein aggregates or dense liquid domain formation. Stage b shows the size increase of the black dot into a dark sphere, indicating further growth by aggregated protein molecules over time. Note that at this stage, the dark sphere will not disappear by stopping the applied potential. Stage c features a gradual decrease in current amplitude. Optically, a transformation from dark sphere into bright or more transparent structures with vague facets suggests the formation of ordered assembly lattice, i.e. crystal embryo. Depending on the location, i.e. the distance from the nanotip, the ordered lattice structure, and subsequent crystal growth could partially block the mass transport through the nanopipette tip and cause the current to decrease. After stage c, the current curve displays more significant variations (elaborated in Fig.4-5 Growth control) due to the increased disturbance of ion transport over the course of further growth. As shown in the image d, the facets developed further. The overall morphology seems to reveal polycrystals instead of a single one. As explained next, a higher potential is required to initiate the crystal nucleation by providing kinetic energy to overcome the thermodynamic energy barrier. After nucleation and reaching the critical embryo size, the high materials flux provided by the same potential magnitude triggers multiple nuclei formation or poor molecular assembly around the initial nucleus, as shown in Fig.4-4. Either way, as discussed next, the applied potential magnitude needs to decrease immediately after the initial nucleation stage c.

The ‘V’-shape current curve at stage c corresponds to the optical transition of better visible light diffraction/transmission. Those current and visual features clearly reveal critical information during nucleation. Systematic analysis is summarized in Fig. 4-2 B and C. The dynamics of mass transport depends on many factors, including nanopipette size, surface charges, interior acid concentration, applied potential and exterior protein pH. To be consistent for quantitative comparison, the interior and exterior solution conditions were maintained constant during each series of measurements (i.e. using the same protein solution). By using the same or similar sized nanopipettes, the applied potential was varied to adjust the input energy systematically. The current features during the nucleation process are shown in Fig.4-2 C. As we can see, at potentials as low as 450 mV and 600 mV, we did not observe any current disturbance over 20 min. Optically, we did observe the formation of a dark sphere but didn't observe the subsequent transformation into brighter structures. At 800 mV and 1000 mV, both current disturbance and optical transformations were observed. The circles highlight the V-shape critical transformation corresponding to the optical transitions. Higher potential magnitude appears to induce the transformation at an earlier time compared to lower potentials. It is unequivocal that a sufficiently high potential will initiate the nucleation process. Quantitative correlations between the nucleation initiation and the potential magnitude will require further measurements. There are many factors that would affect such dynamic heterogeneous processes that require better fundamental understanding of mass transport that remain to be established.

The V-shape current feature is a robust signature to indicate nucleation transition. However, not every nucleation would generate a detectable V-shape in the current curve.

The reproducibility is evaluated using the same and similar sized nanopipettes with results shown in Fig. 4-3. Depending on how close the initial assembly/aggregation is from the signal limiting nanotip area, the extent of disturbance on the mass transport trajectory will vary. In another word, if the transformation occurs further away from the tip rather than close by, it will have less, possibly a negligible effect on the current signal.

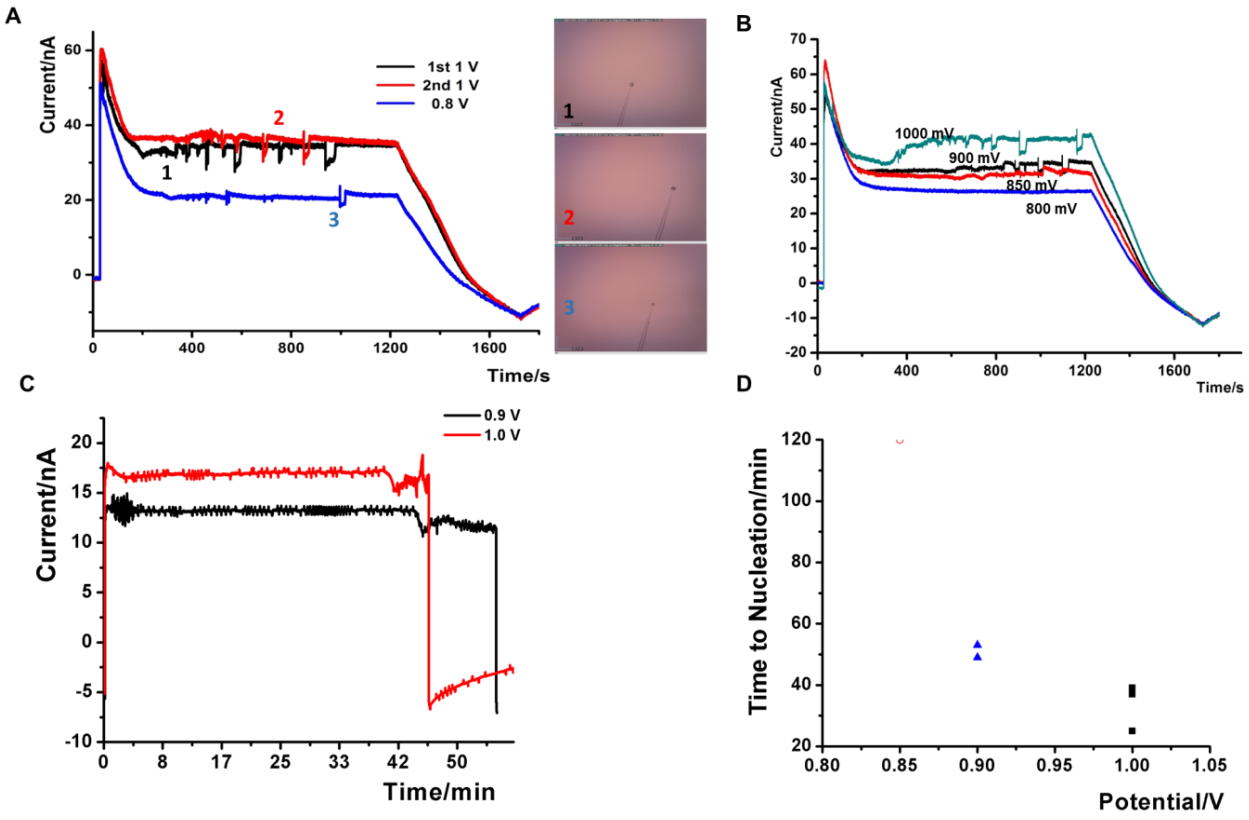

Fig.4-3 Reproducibility check of nucleation process from a 5 nm nanopipette A) Overlaid i-t curves under different applied potential and corresponding crystal seeds after each applied curve from the same nanopipette in the context B) Overlaid i-t curves under different applied potential from another 5 nm nanopipette. C) Current responses from a 2 nm radius nanopipette at 0.9 V and 1.0 V. Small oscillations in the curve might be due to external electrical noise or insulin transport. D) Time to nucleate reproducibility check for the nanopipette shown in C at 0.9 V and 1.0 V back and forth. At 0.85 V, no nuclei formed in 120 min, as shown in a hollow red dot. All the curves in each plot are from one specific nanopipette. To obtain reproducible data, first the nanopipette was pulled out of the solution and immersed in a pH 1 HCl solution for 10 s to dissolve the crystal formed

at the tip. And then immerse it in the water for 5 s to get rid of the absorbed acid at the exterior of the nanopipette. Then the nanopipette was reinserted in the solution.

4.4.1.2 Optimized approach for single seed formation

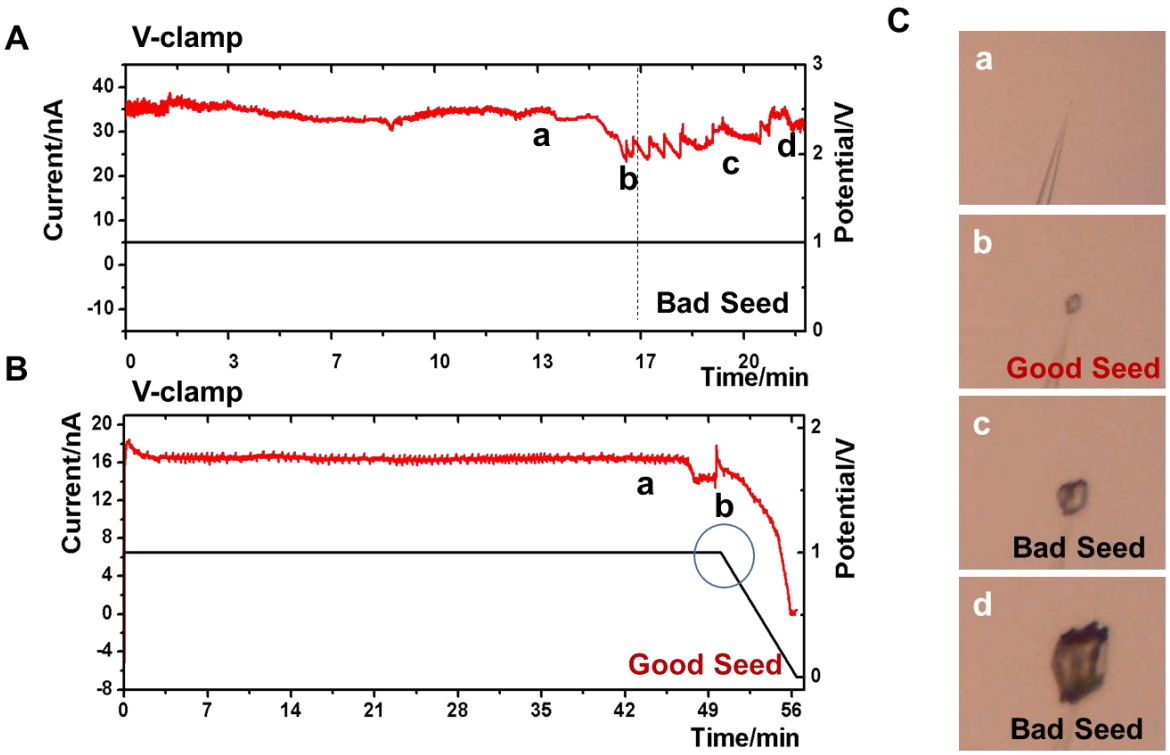

Fig. 4-4 i-t curve under applied potentials and in-situ optical images to show holding potential at nucleation potential for a long time will cause not only the seeds growth but also further development of extra seeds, polycrystals or even amorphous, as shown in the last graph. Note that the good seeds and bad seeds are differentiated based on optical image only.

To summarize, we propose to decrease the applied constant potential slowly right after the crystalline structure first developed, which was indicated by the smooth current decrease after the current stabilizes for some time and corresponding optical image monitor, as shown in Fig. 4-4 B. After the applied potential program as shown in the panel B, a stable good seed will remain at the nanopipette tip without significant size increase over times.

4.4.2 Growth Control:

4.4.2.1 Optimized seed growth under current clamping controls

The crystal growth is a spontaneous downhill energy process after the seed formation in a metastable solution. The growth rate is highly dependent on the solution condition. High growth rate could deteriorate the crystal quality/morphology. When using the nanotip to initiate the nucleus formation, further growth process can be very slow limited by the small tip opening through which mass transport is needed to maintain the metastable condition via passive diffusion (keep in mind that the bulk solution away from the nanotip is not in the metastable zone). In other words, the crystal cannot grow beyond the metastable zone established near the nanotip. Evaporation and other complications such as vibration of the solution could also interfere over a long period. The external potential is further designed to actively control mass transport rate to facilitate the embryo growth. From the earlier nucleation studies, it is clear that applying a high potential after nucleation is not appropriate for crystal growth because new nuclei and defects could develop under the high mass flux: those abrupt current change in Figure 4-2 c indicates transient blockage of mass transport around the nanotip or the seed.

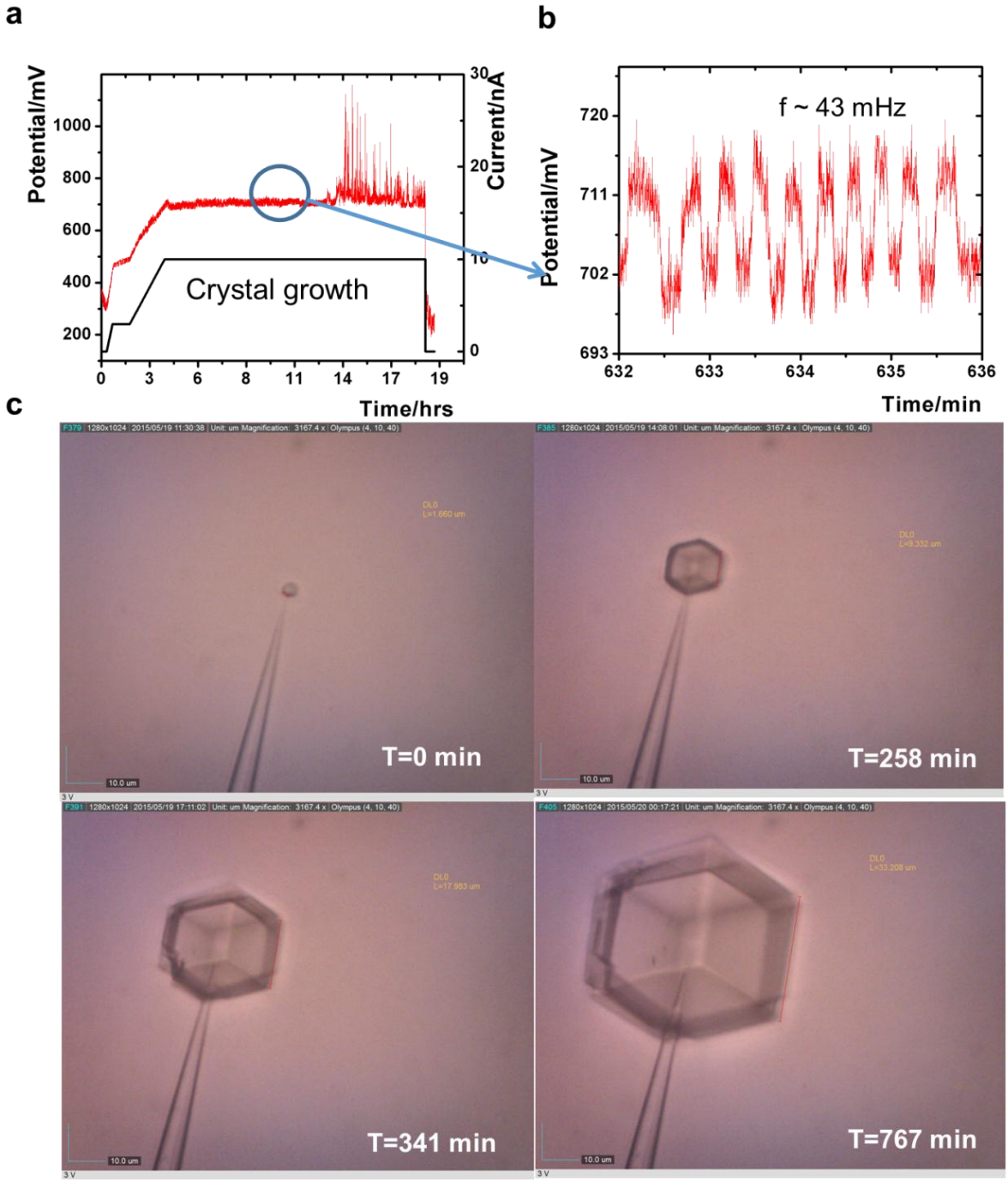

Fig. 4-5 a) Representative potential-time features (red curve, left axis) under programmed current (black, right axis) over time. b) Potential oscillation from a zoom-in view of the V-t plot. c) Representative corresponding time-lapse pictures of crystal growth over time. Note that the images and the potential oscillation data are not from the same experiment.

To better control the crystal growth, the current is fixed at a constant value (current-clamping) by varying the applied potential after the nucleation. The rationale is to provide a constant influx of matter to maintain stable growth. The results are shown in Fig.4-5. The applied potential is reduced to zero immediately after the V-shape transition is observed in current monitoring during the nucleation to avoid defect formation on the embryo, as shown in Fig. 4-4 panel B. Starting at time zero in Fig. 4-5, the instrument applies the current as programmed and records the potential shown as the red curve. Shown in the V-t curve, the potential, albeit remain at hundreds of millivolts to maintain the current, switches between a high and low state at small magnitudes, ca. ±10 mV. The oscillation behaviors suggest that the applied potential needs to make a transient adjustment to ensure steady mass transport. Apparently the growth of the embryo increasingly blocks the mass transport route across the tip region, which explains why a constant DC bias fails to produce crystals at high quality. The periodic potential oscillation recovers the steady-state mass flux either by reducing the influx or by pushing the seed further away from the tip. Further experiments are needed to provide conclusive evidence for the root cause. Crystal images collected during the current clamping process are shown in Fig.4-5. It is worth mentioning that the nanopipette tip is normally embedded in the formed crystal, which is a convenient feature to handle the final crystal by the careful maneuver of the long shaft from the other end of the quartz capillary.

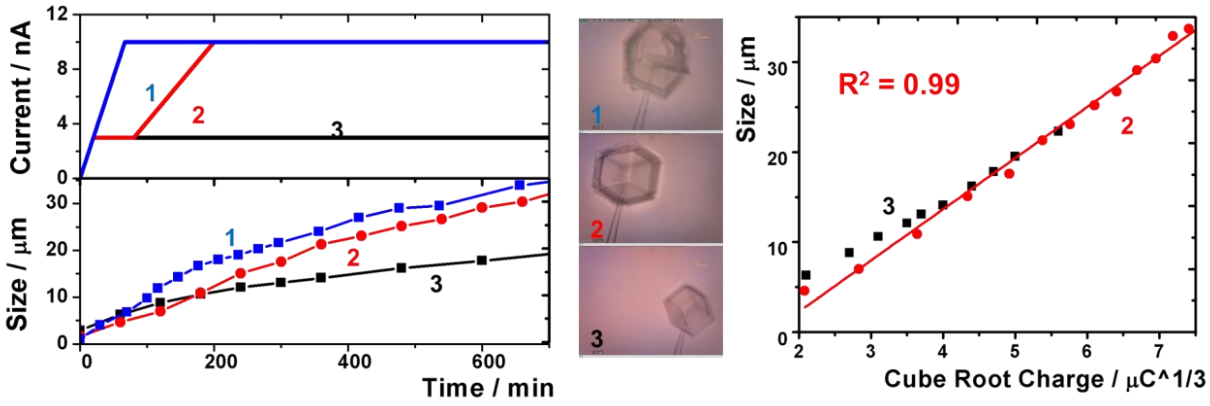

Fig. 4-6 A) Crystal growth under different programmed current profiles. B) Optical images of the final crystals from the corresponding growth curves. C) Analysis of crystal size and the volume of the charge influx. One edge of the crystal was measured as the size periodically during the growth without any movement. The corresponding charges are obtained from the area under the current curve at the time of size measurement.) The accumulated charges are directly proportional to the volume of the crystal, whose cubic root displays linear relationship with size.

Next we programmed different i-t curves and monitored the crystal growth process over time, as shown in Fig.4-6 A. The higher the current is clamped to, the faster the crystal will grow. However, it doesn't mean higher current will always be better. According to the microscope images, the highest current from program 1 causes the crystal to develop more facets and irregular packing inside the crystal during its growth process, as details shown in Fig.4-7. It means there is an upper limit for the clamped current. Besides, an excellent linear correlation between the crystal edge dimension and cube root of charges was found, which indicates the successful current clamping control in crystal growth rate. Additional results in the crystal growth rate over time under different clamped current are shown in Fig.4-8, Fig.4-9. and Fig.4-11.

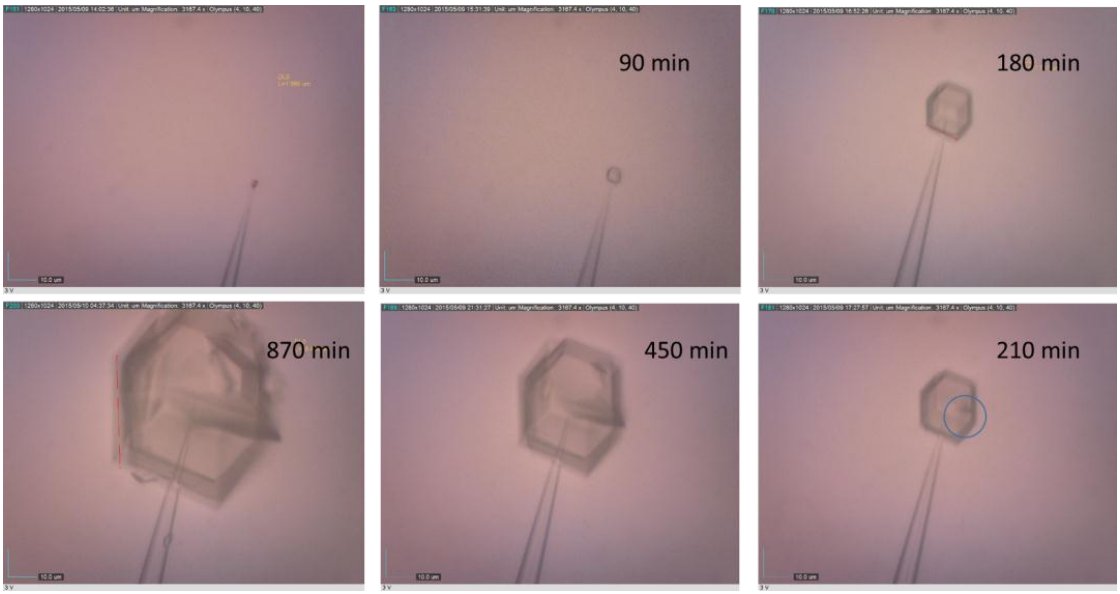

Fig. 4-7 Impacts of applied current at high amplitude: time lapse of crystal growth over time from Fig.4-6 program 1. An extra nucleus developed from the center of the crystal from 210 min. This extra crystal lattice further develops and forms very irregular multiple crystal structure. The scale bar is 10 um.

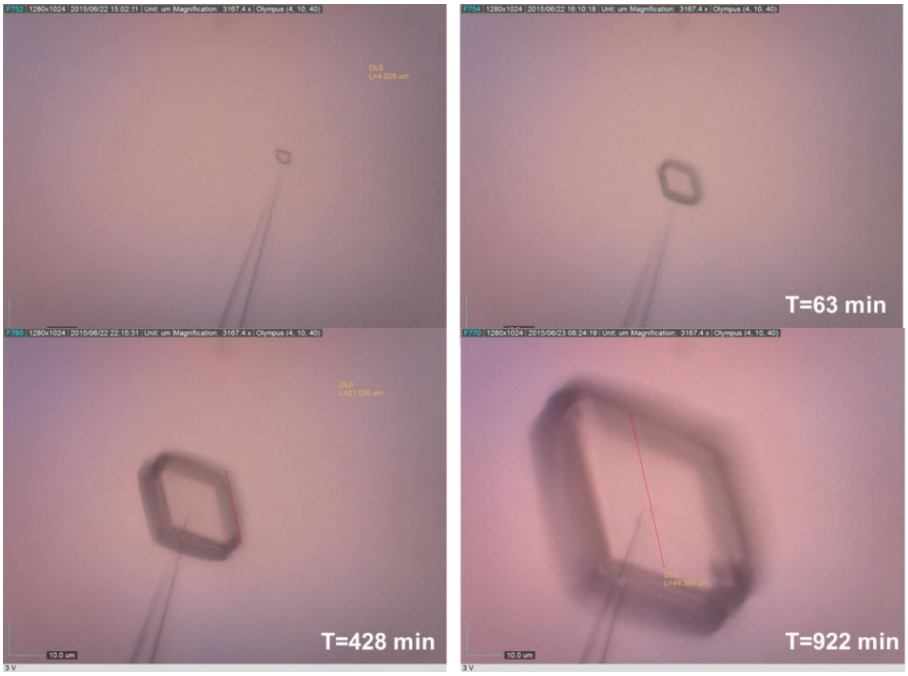

Fig. 4-8 Another set of time-lapse pictures of a crystal seed growth process under current clamping waveform. The scale bar is 10 um.

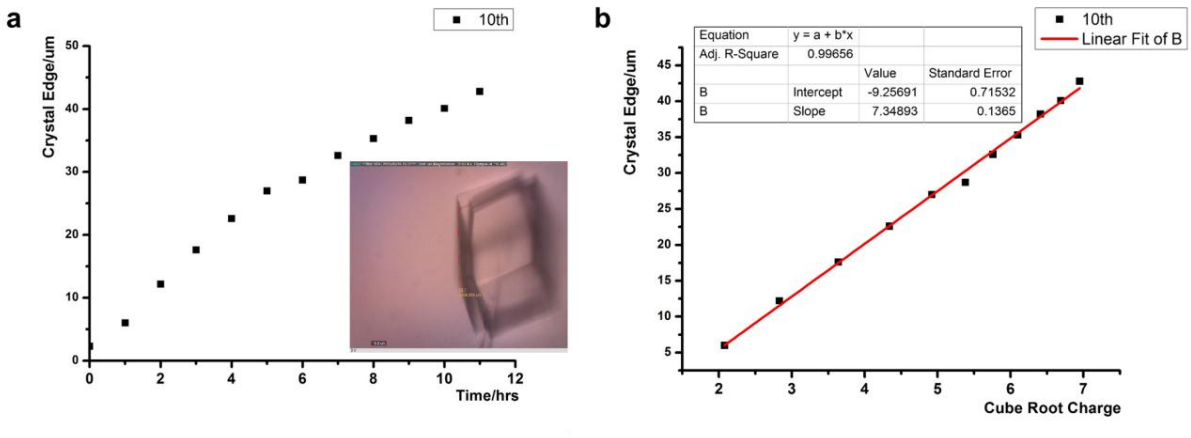

Fig. 4-9 Another representative view of a crystal growth over time and the linear relationship between the crystal edge with cube root charges. The scale bar is 10 um.

4.4.2.2 Visual Morphology of grown crystals on nanopipette tips

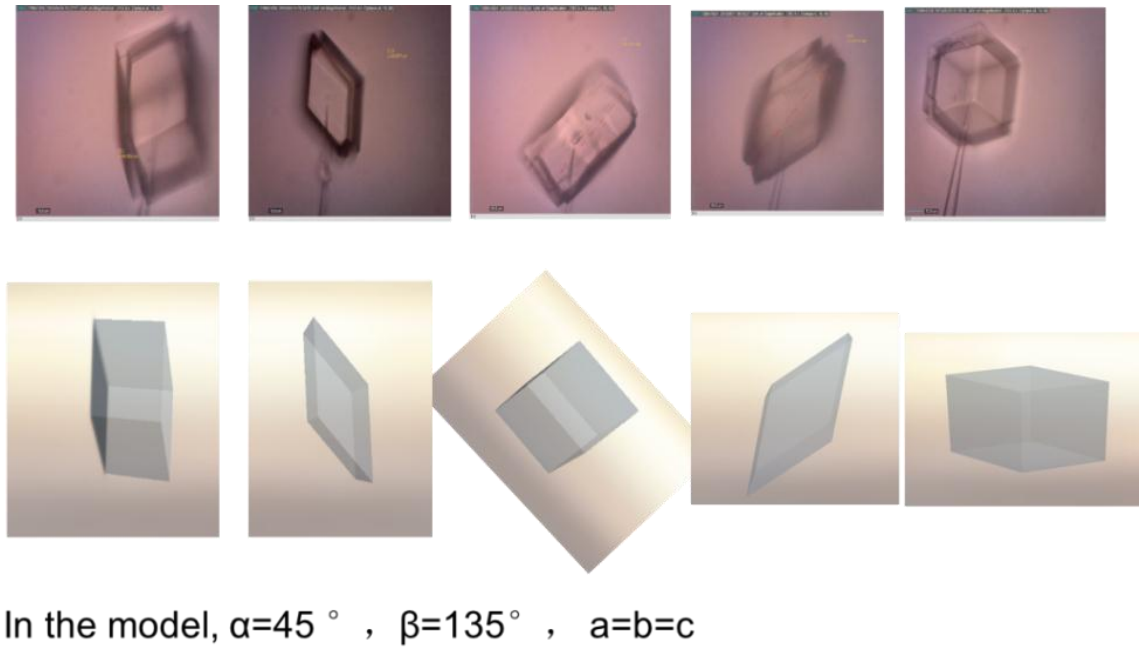

Fig. 4-10 Illustration of a modeled crystal with defined morphology presented at different orientations for the comparison of different crystals grown at the tips directly.

Different views of a crystal viewed from 3-D modeling are shown in Fig. 3-10. Some representative crystals grown on the nanotip from different experiments were

arbitrarily aligned. From the visual comparison, we propose that the crystals grown from the nanopipette tip share the same or similar morphology but have different sizes and orientation at the tip. The model was simulated by Solidworks. It is clear that visual effects could be misleading to argue difference or similarity of a given crystal. For example, for the crystal in rectangle orientation, the longer edge might be composed of two separate edges at an angle as illustrated in the middle picture. The linear edge-charge correlation, i.e. size-volume, discussed in the previous section is not affected by such visual effect given the growth rate along a, b and c direction is the same. Technically, each growth curve was established by measuring the same crystal on the nanotip over time without any physical movement of the whole experiment setup, which ensures a consistent view angle.

4.4.2.3 Reproducibility of crystal growth under applied current waveform

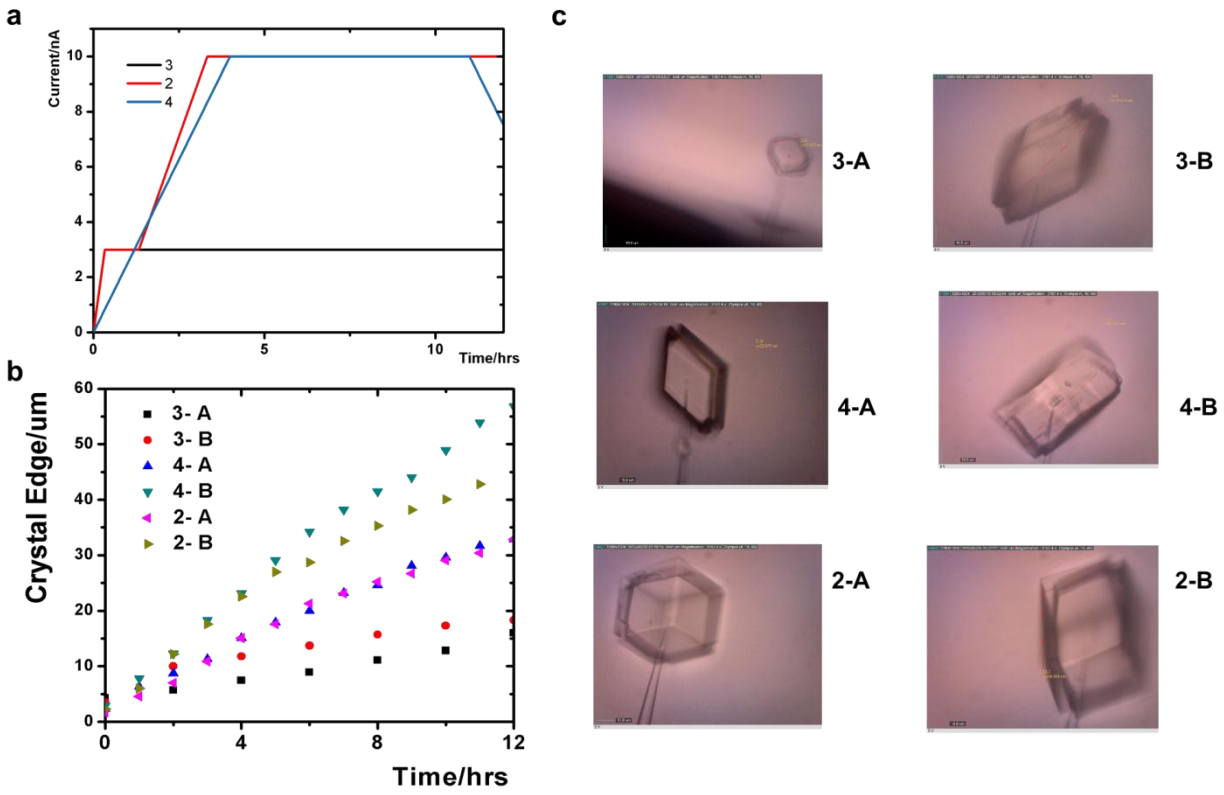

Fig. 4-11 a) Different programmed current clamping and b) corresponding crystal growth rates and c) optical images

To study the crystal growth rate reproducibility under different applied potential programs, two crystals under each program were analyzed. Note that program 2 and 4 has similar charges input rate compared to program 3 but a slightly difference in the initial current clamping condition. From growth rate curve we can see that crystals 3-A and 3-B grow slower compared to other crystals grown under a higher current clamping control, which is consistent with what we expect. The slightly difference in the initial current clamping didn't seem to introduce a observable difference in the crystal growth rate. Regarding to the two slightly deviations #10 and #8, it is because #8 and #10 share similar orientation on the nanopipette tip. For both of them the longer edge of the

rectangle was used to analyze the crystal growth rate, which clearly has an offset and is larger than real edge length. This concept was explained in Fig.4-10.

4.4.3 Control Experiments

4.4.3.1 Step potential as a general approach to screen control parameters

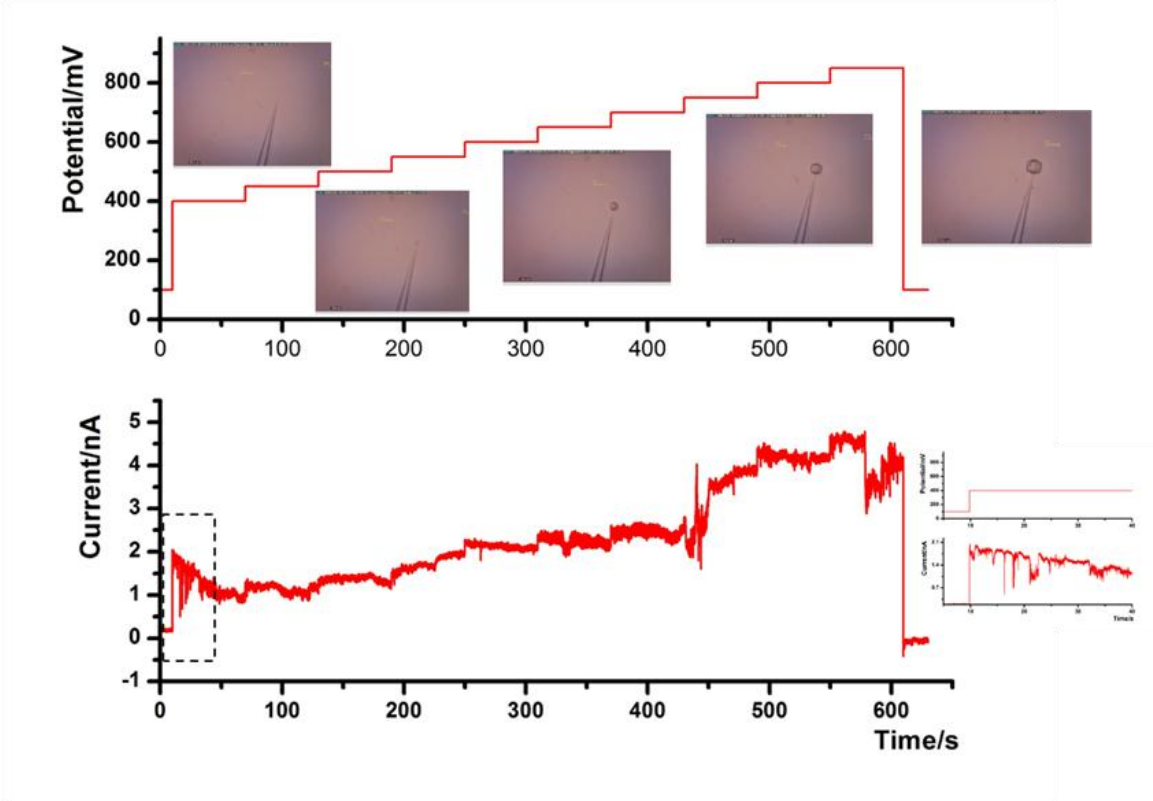

Fig. 4-12 Representative curve of designed applied step potential waveform with corresponding current response and in-situ optical images.

Step potential was applied over time to screen the right potential for nucleation. As indicated in the zoomed in the graph in the i-t curve, some current oscillation was observed after applying 400 mV, after which some small dark spot formed around the nanopipette tip region. This current oscillation might indicate the transport of protein aggregates through the nanopipette tip sensing zone. After a while, this current oscillation

behavior disappeared because all these aggregates have been driven out of the nanopipette sensing zone and accumulate around the nanopipette tip. This 400 mV is the on-site potential that is the minimal potential needed to trigger the nucleation process. For different nanopipettes with different geometry, this on-site potential varies from 300 mV~ 1000 mV. With increasing the potential step, this small aggregate will grow larger and until to a point at which it will transform into a single crystal. This single crystal will continue to grow with a further potential applied. As shown in the optical images, a nice cubic crystal formed and grew right at the nanopipette tip.

4.4.3.2 Exterior protein pH effect

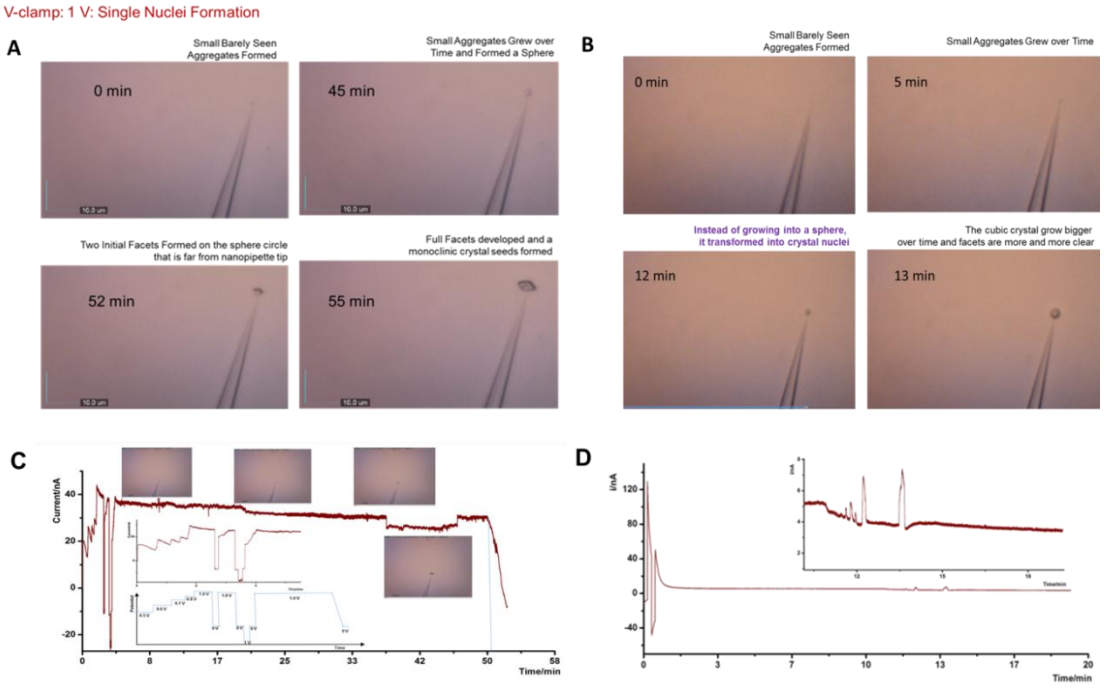

Fig. 4-13 External protein pH effect: A comparison of the nucleation process from two slightly different proteins over time in A) pH 7.9 B) pH 7.5 and nucleation i-t curves in C) pH 7.9 D) pH 7.5.

When the bulk solution is slightly changed, the time it takes to nucleate will be different as shown in Fig.4-13. When the insulin pH is approaching pI like 7.5, it takes shorter time to nucleate, and the pI 5 is around signal limiting region, thus we observed smooth current decrease with some oscillation at the curve, as shown in Fig.4-13 D. However, if we use pH 7.9, it takes around 45 min to transform and the current curve did not show sensitive, smooth current decrease, as shown in Fig.4-13 C. The pI 5 is at the far edge of round nucleus, where the first facet develops and continues to grow from there as shown in Fig.4-13 A.

4.4.3.3 Evaporation Effect:

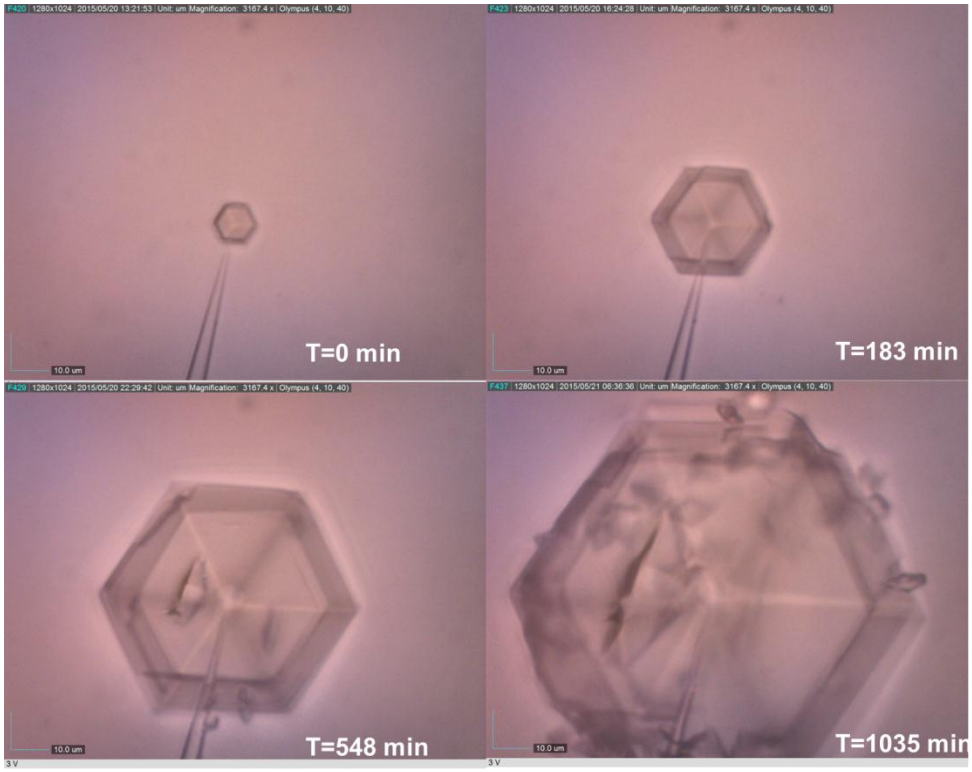

Fig. 4-14 Evaporation effect on crystal growth. Time-lapse pictures of a crystal seed growth process under poor controlled evaporation.

As we can see, at the beginning the developed seed is clear and uniform. However, over time, some nucleus started to nucleate even on top of the grown crystal due to poor evaporation control and finally showers of crystal seeds took over the crystal and formed a poor quality polycrystal. This graph is used to demonstrate the importance of limiting evaporation in the experiment. Although slightly evaporation rate is a good thing to facilitate crystal nucleate and growth, it's very difficult to control the solution evaporation rate. Different from higher transient energy introduced by nanopipette and externally applied potential, the extra nucleus due to evaporation formed on the exterior of the crystal instead of the interior of the crystal.

4.4.3.4 Pipette size effect

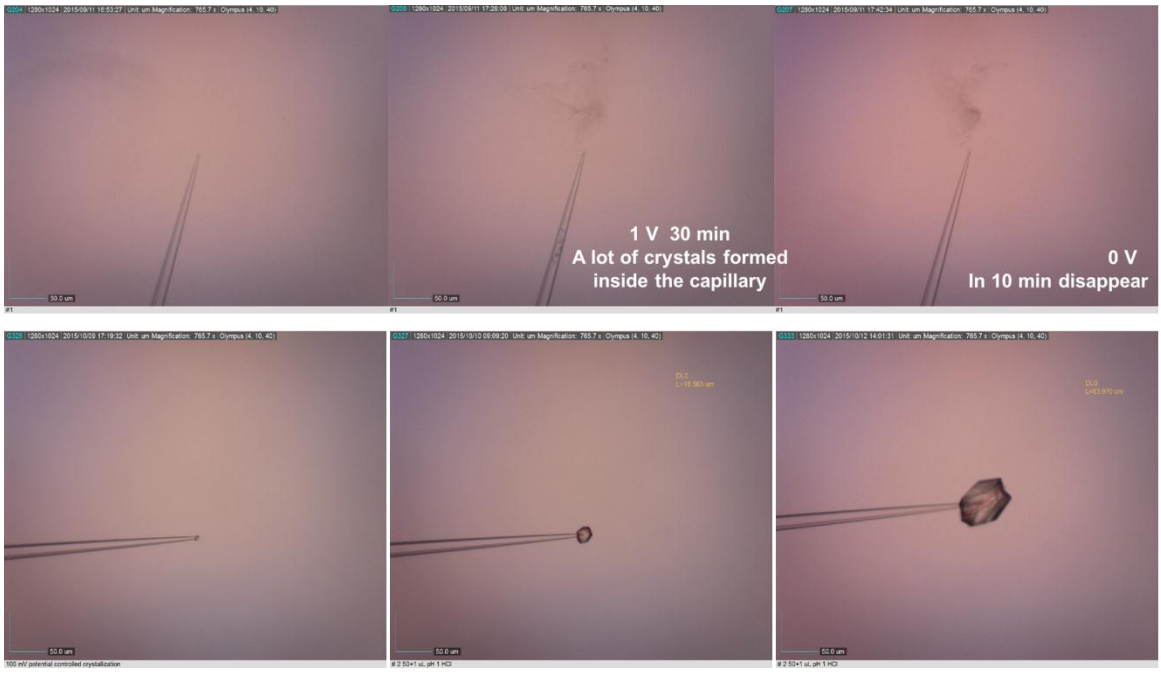

Fig. 4-15 Pipette size effect on crystallization process. The size of nanopipette is 5 um for upper three panels while the nanopipette size is 1 um for the bottom three panels.

For the 5 um nanopipette, after applying 1 V, nothing happened. Over 30 min courses, multiple crystals will form inside the nanopipette tip, and some protein precipitate is floating outside the nanopipette tip. When applied potential stopped, all the crystals disappear, but protein precipitate remains there.

For the 1 um nanopipette, after applying 0.1 V, the crystal formed and grew very fast. It demonstrates for this opening nanopipette; a small potential will be enough to trigger the nucleation process, and a single crystal can be controlled. However, as observed in Fig. 4-15, the crystal quality, is not perfect and hard to control due to relative large opening induced larger acid contact with the crystal inducing fast nucleation and growth.

4.4.3.5 Replacement of interior precipitating solution

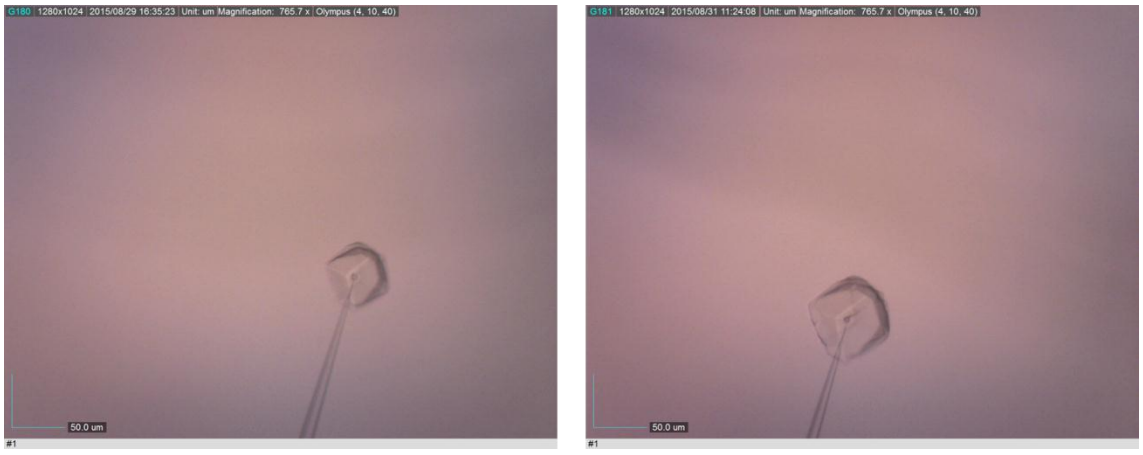

Fig. 4-16 Interior solution effect on crystal quality. Left panel: 1 M HCl inside crystal. Right panel: 1 M HCl was replaced by same sat. insulin.

For this method, the most worrying part is probably the high concentrated acid inside the nanopipette. We observed the fact that at first the crystal quality looked good, but suddenly some slight defects showed up in the center immediately after we stopped applying potential. This is due to the sudden transient movement of acid out to contaminate the protein crystal on the tip. Slowly decreasing applied current until to the point it stopped helped a bit on this but still diffusional of acid over time is still a little bit worrying. So we tried to replace the interior of acid solution with sat. insulin. Note that improper handling might cause some pressure inside the nanopipette and cause more transient acid diffusion, so this process needs care and caution. As shown in the graph, first the crystal growth over time and still a small slight defect showed up in the center. Overall, there is no significant visual damage to the crystal.

4.4.3.6 Technical Problems Trouble-shoot:

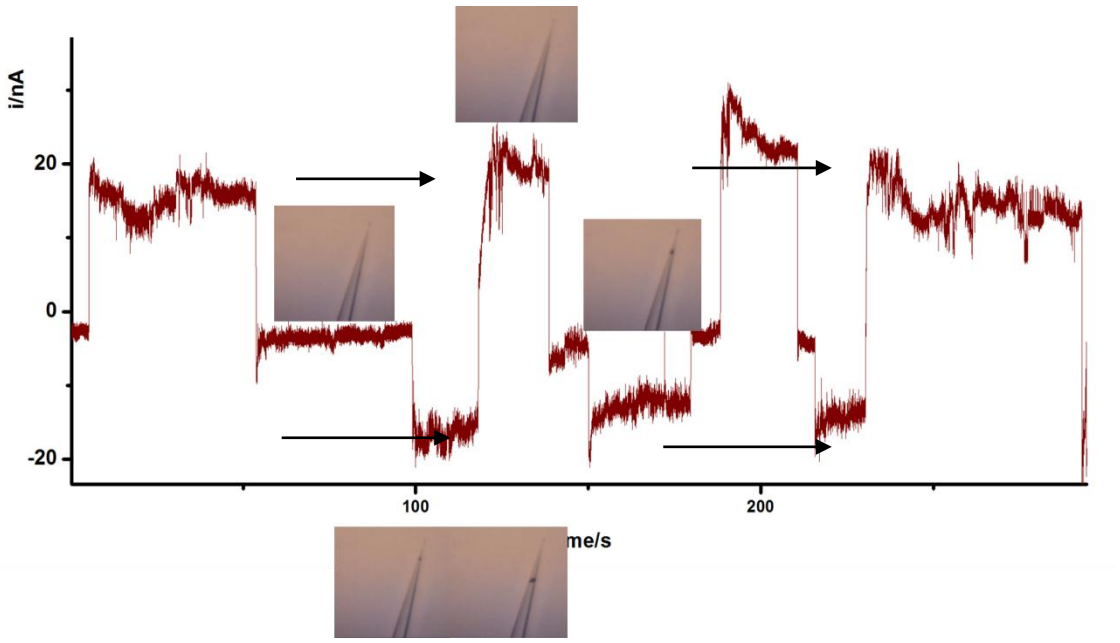

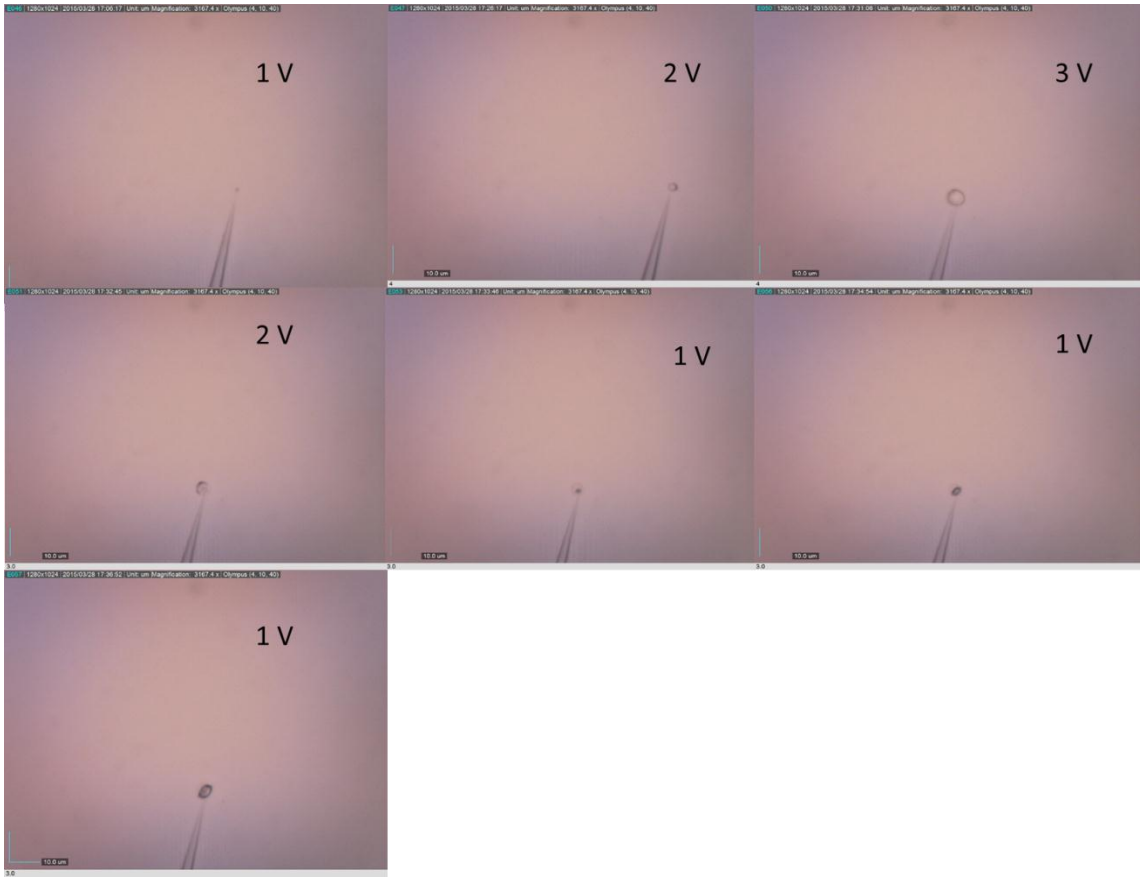

Fig. 4-17 Two representative graphs to demonstrate typical problems observed with the degrading ITO glass.

Although this method is relatively simple in design and works often, sometimes reproducibility is a problem for the insulin solution. Presence of the dark spot is observed; however, formation of the dark spherical ball and transformation into the crystal is not.

After applying 1 V for 1 hr, nothing was observed, including the dark spherical precipitate.

While trouble-shooting, the first task is to investigate the ITO glass and the complete electrical circuit, especially the connections. At times, an insulating layer that

impedes conductivity, where the alligator clip is connected might cover ITO glass surface. This can be easily tested by monitoring the current, with the potential at 1 V. Since the concentration of the precipitant agent is high, the current should not be relatively low, for example if using 1 M HCl the current at 1 V should not be lower than 1 nA for a 5 nm nanopipette. Most of the time protein will be in a buffer, and the buffer has many charge carriers.

If the ITO glass is conductive and the whole circuit does not have connection issues, but there is no formation of the dark spherical nuclei, this indicates bad experimental design or bad experimental conditions. Examples of bad experimental conditions include: nanopipette size, precipitant concentration, or protein solution condition which is not suitable for the seed formation to be at the nanopipette tip, instead in the surrounding solution（precipitate floating）or inside the nanopipette (nanopipette size too big) or the energy might be too low for the ions to transport, meet and crystallize. In this case, try to either 1.) replace the nanopipette if visually the size is not appropriate 2.) increase the applied potential 3.) increase the precipitating agent concentration to input more energy to the system.

If all steps do not work, please check the experimental design or change to a new one.

Black spherical nuclei formed after applying high potential, like 1 V, but they didn't grow large or transform into a crystal.

This is the most common problem encountered. It means, the condition is right, but there are not sufficient protein molecules to be transported around the tip for the aggregate to grow in size. There may be many reasons for this situation.

First, the ITO Glass signal limiting area surface degraded over time due to slightly acid disposer, scratch, or protein absorption

As shown in graph 4-16, from the i-t curve, when the potential was switched, no significant charging or discharging current showed up. It just showed a normal resistive behavior. In addition, the current might be low compared to the normal state but is not necessary low. Also, many oscillating spikes are observed in the curve. From the bottom graph, it's clear that an increased potential will help. When the potential was increased to be as high as 3 V, the real electric field drop on the protein will be sufficient for them to move to the tip. But using too high of a potential will cause the shift of the precipitating solution farther away from the tip and increase the volume. At this point, a decrease of the potential will cause the acid to move back to the tip and required nucleation volume decreases while the protein molecules' mobility is too slow to follow and they molecules will be trapped there at the tip which and enriches the area to promote nucleation. All these features indicate it's highly possible likely the ITO glass has been degraded. The significant partial failure in ITO glass will cause a significant potential drop on the glass surface and affect the protein movement to the nanopipette tip significantly. At this point, switch to a new device.

If these still don't work, check the protein solution. First, check if there are small black seeds floating around, which might be an indication that the solution has already nucleated and formed showers of small crystals or seeds, which consumes the protein

molecules and makes it very difficult to grow larger. Second, double check if this protein solution is in the metastable zone. Because if the protein is not in the metastable zone, there will be a balance of formation and dissolving of the precipitate. As a result, it might just remain as a black precipitate there.

For other protein systems, please double-check if the solution is too viscous because viscosity will significantly decrease the movement of a protein to the tip and affect the protein's nucleation and growth process.

4.5 Conclusion and perspective:

We have demonstrated successful active electrochemical control of insulin single crystal seeds formation and growth by manipulating mass transport through a single nanopipette associated with in situ microscope monitoring of nanopipette tip. First we observed the reversible formation and disappearance of a dark spot right at the nanopipette tip after application of the positive potential. This dark spot might remain at the nanopipette tip without significant growth in hours at lower constant applied electric field. When the dark spot's dimension increases over time at higher constant applied electric field, it first grows from dark spot to dark sphere and then starts to transform and form ordered crystal lattice. Crystal transition from dark sphere to a brighter structure with faces in an optical image and current disturbance can both be observed as an indication for this process. To ensure the seed quality, right after the crystalline structure developed the applied potential is decreased smoothly to zero. Second, to ensure the crystal growth quality and facilitate the growth rate, constant current clamping is used to control the crystal growth process. By programming different currents, we found that the

higher current clamped, the faster the crystal will grow, and there is an upper limit for the clamped current. When the current is clamped too high, the crystal will develop defects and crystal quality will be ruined. Other killing factors were also discussed in the paper.

In general, this method shows a big potential to be applied in crystallizing other more complicated proteins or charged macromolecules based on appropriate experimental design. A precipitate with the charge will be a priority over other precipitating solution, and the protein has to be in the opposite charge state and metastable zone favorable for the follow-up growth. Otherwise, the round precipitate formed at the nanopipette tip will reach a balance forming and dissolving. The biggest advantage and drawback of this method is the production of only one crystal at one time. To solve this problem in the future, multiple nanofluidic devices can be designed, integrated, and employed to grow multiple crystals at the same time for a scale-up purpose.

References

1 Storm, A. J., Chen, J. H., Ling, X. S., Zandbergen, H. W. & Dekker, C. Fabrication of solid-state nanopores with single-nanometre precision. *Nat Mater* **2**, 537-540, doi:http://www.nature.com/nmat/journal/v2/n8/suppinfo/nmat941_S1.html (2003).

2 Li, J. *et al.* Ion-beam sculpting at nanometre length scales. *Nature* **412**, 166-169 (2001).

3 Chen, P. *et al.* Atomic Layer Deposition to Fine-Tune the Surface Properties and Diameters of Fabricated Nanopores. *Nano Letters* **4**, 1333-1337, doi:10.1021/nl0494001 (2004).

4 Menard, L. D. & Ramsey, J. M. Fabrication of Sub-5 nm Nanochannels in Insulating Substrates Using Focused Ion Beam Milling. *Nano Letters* **11**, 512-517, doi:10.1021/nl103369g (2011).

5 Apel, P. Y., Korchev, Y. E., Siwy, Z., Spohr, R. & Yoshida, M. Diode-like single-ion track membrane prepared by electro-stopping. *Nuclear Instruments and Methods in Physics Research Section B: Beam Interactions with Materials and*

Atoms **184**, 337-346, doi:http://dx.doi.org/10.1016/S0168-583X(01)00722-4 (2001).

6 Siwy, Z. & Fuliński, A. Fabrication of a Synthetic Nanopore Ion Pump. *Physical Review Letters* **89**, 198103 (2002).

7 Guo, W. *et al.* Energy Harvesting with Single-Ion-Selective Nanopores: A Concentration-Gradient-Driven Nanofluidic Power Source. *Advanced Functional Materials* **20**, 1339-1344, doi:10.1002/adfm.200902312 (2010).

8 Siwy, Z., Dobrev, D., Neumann, R., Trautmann, C. & Voss, K. Electro-responsive asymmetric nanopores in polyimide with stable ion-current signal. *Appl Phys A* **76**, 781-785, doi:10.1007/s00339-002-1982-7 (2003).

9 Kececi, K., San, N. & Kaya, D. Nanopore detection of double stranded DNA using a track-etched polycarbonate membrane. *Talanta* **144**, 268-274, doi:http://dx.doi.org/10.1016/j.talanta.2015.06.005 (2015).

10 Zhang, B. *et al.* Bench-Top Method for Fabricating Glass-Sealed Nanodisk Electrodes, Glass Nanopore Electrodes, and Glass Nanopore Membranes of Controlled Size. *Analytical Chemistry* **79**, 4778-4787, doi:10.1021/ac070609j (2007).

11 Umehara, S. *et al.* Current Rectification with Poly-l-Lysine-Coated Quartz Nanopipettes. *Nano Letters* **6**, 2486-2492, doi:10.1021/nl061681k (2006).

12 Liu, J. *et al.* Surface Charge Density Determination of Single Conical Nanopores Based on Normalized Ion Current Rectification. *Langmuir* **28**, 1588-1595, doi:10.1021/la203106w (2012).

13 Liu, J. *et al.* Noninvasive Surface Coverage Determination of Chemically Modified Conical Nanopores that Rectify Ion Transport. *Analytical Chemistry* **84**, 6926-6929, doi:10.1021/ac301791e (2012).

14 Liu, J. *et al.* Quantification of Steady-State Ion Transport through Single Conical Nanopores and a Nonuniform Distribution of Surface Charges. *Langmuir* **29**, 8743-8752, doi:10.1021/la4009009 (2013).

15 Sa, N., Lan, W.-J., Shi, W. & Baker, L. A. Rectification of Ion Current in Nanopipettes by External Substrates. *ACS Nano* **7**, 11272-11282, doi:10.1021/nn4050485 (2013).

16 Yeh, L.-H. *et al.* Electrokinetic ion and fluid transport in nanopores functionalized by polyelectrolyte brushes. *Nanoscale* **4**, 5169-5177, doi:10.1039/c2nr31069d (2012).

17 Rice, C. L. & Whitehead, R. Electrokinetic Flow in a Narrow Cylindrical Capillary. *The Journal of Physical Chemistry* **69**, 4017-4024, doi:10.1021/j100895a062 (1965).

18 Pennathur, S. & Santiago, J. G. Electrokinetic Transport in Nanochannels. 2. Experiments. *Analytical Chemistry* **77**, 6782-6789, doi:10.1021/ac0508346 (2005).

19 Wei, C., Bard, A. J. & Feldberg, S. W. Current Rectification at Quartz Nanopipet Electrodes. *Analytical Chemistry* **69**, 4627-4633, doi:10.1021/ac970551g (1997).

20 Cao, L., Guo, W., Wang, Y. & Jiang, L. Concentration-Gradient-Dependent Ion Current Rectification in Charged Conical Nanopores. *Langmuir* **28**, 2194-2199, doi:10.1021/la203837q (2012).

21 Sa, N. & Baker, L. A. Rectification of Nanopores at Surfaces. *Journal of the American Chemical Society* **133**, 10398-10401, doi:10.1021/ja203883q (2011).

22 Feng, J., Liu, J., Wu, B. & Wang, G. Impedance Characteristics of Amine Modified Single Glass Nanopores. *Analytical Chemistry* **82**, 4520-4528, doi:10.1021/ac100440z (2010).

23 Wang, D. *et al.* Transmembrane Potential across Single Conical Nanopores and Resulting Memristive and Memcapacitive Ion Transport. *Journal of the American Chemical Society* **134**, 3651-3654, doi:10.1021/ja211142e (2012).

24 Wang, D. *et al.* Physical origin of dynamic ion transport features through single conical nanopores at different bias frequencies. *Chemical Science* **5**, 1827-1832, doi:10.1039/c3sc52187g (2014).

25 McNally, B. *et al.* Optical Recognition of Converted DNA Nucleotides for Single-Molecule DNA Sequencing Using Nanopore Arrays. *Nano Letters* **10**, 2237-2244, doi:10.1021/nl1012147 (2010).

26 Ai, Y., Liu, J., Zhang, B. & Qian, S. Field Effect Regulation of DNA Translocation through a Nanopore. *Analytical Chemistry* **82**, 8217-8225, doi:10.1021/ac101628e (2010).

27 Min, S. K., Kim, W. Y., Cho, Y. & Kim, K. S. Fast DNA sequencing with a graphene-based nanochannel device. *Nat Nano* **6**, 162-165, doi:http://www.nature.com/nnano/journal/v6/n3/abs/nnano.2010.283.html#supplementary-information (2011).

28 Yusko, E. C. *et al.* Controlling protein translocation through nanopores with bio-inspired fluid walls. *Nat Nano* **6**, 253-260, doi:http://www.nature.com/nnano/journal/v6/n4/abs/nnano.2011.12.html#supplementary-information (2011).

29 Howorka, S. & Siwy, Z. S. Nanopores as protein sensors. *Nat Biotech* **30**, 506-507, doi:10.1038/nbt.2264 (2012).

30 Steinbock, L. J. *et al.* Probing the size of proteins with glass nanopores. *Nanoscale* **6**, 14380-14387, doi:10.1039/c4nr05001k (2014).

31 Makra, I. & Gyurcsányi, R. E. Electrochemical sensing with nanopores: A mini review. *Electrochemistry Communications* **43**, 55-59, doi:http://dx.doi.org/10.1016/j.elecom.2014.03.007 (2014).

32 Miles, B. N. *et al.* Single molecule sensing with solid-state nanopores: novel materials, methods, and applications. *Chemical Society Reviews* **42**, 15-28, doi:10.1039/c2cs35286a (2013).

33 Hu, K. *et al.* Open Carbon Nanopipettes as Resistive-Pulse Sensors, Rectification Sensors, and Electrochemical Nanoprobes. *Analytical Chemistry* **86**, 8897-8901, doi:10.1021/ac5022908 (2014).

34 Xu, X., He, H. & Jin, Y. Facile One-Step Photochemical Fabrication and Characterization of an Ultrathin Gold-Decorated Single Glass Nanopipette. *Analytical Chemistry* **87**, 3216-3221, doi:10.1021/ac5034165 (2015).

35 Kim, J. T. *et al.* Three-Dimensional Writing of Conducting Polymer Nanowire Arrays by Meniscus-Guided Polymerization. *Advanced Materials* **23**, 1968-1970, doi:10.1002/adma.201004528 (2011).

36 Vilozny, B., Actis, P., Seger, R. A. & Pourmand, N. Dynamic Control of Nanoprecipitation in a Nanopipette. *ACS Nano* **5**, 3191-3197, doi:10.1021/nn200320b (2011).

37 Masson, J.-F. *et al.* Plasmonic Nanopipette Biosensor. *Analytical Chemistry* **86**, 8998-9005, doi:10.1021/ac501473c (2014).

38 Laforge, F. O., Carpino, J., Rotenberg, S. A. & Mirkin, M. V. Electrochemical attosyringe. *Proceedings of the National Academy of Sciences* **104**, 11895-11900, doi:10.1073/pnas.0705102104 (2007).

39 Adam Seger, R. *et al.* Voltage controlled nano-injection system for single-cell surgery. *Nanoscale* **4**, 5843-5846, doi:10.1039/c2nr31700a (2012).

40 Saha-Shah, A. *et al.* Nanopipettes: probes for local sample analysis. *Chemical Science* **6**, 3334-3341, doi:10.1039/c5sc00668f (2015).

41 Vilozny, B., Actis, P., Seger, R. A., Vallmajo-Martin, Q. & Pourmand, N. Reversible Cation Response with a Protein-Modified Nanopipette. *Analytical Chemistry* **83**, 6121-6126, doi:10.1021/ac201322v (2011).

42 Sa, N., Fu, Y. & Baker, L. A. Reversible Cobalt Ion Binding to Imidazole-Modified Nanopipettes. *Analytical Chemistry* **82**, 9963-9966, doi:10.1021/ac102619j (2010).

43 Tiwari, P. B. *et al.* Quantitative study of protein-protein interactions by quartz nanopipettes. *Nanoscale* **6**, 10255-10263, doi:10.1039/c4nr02964j (2014).

44 DeBlois, R. W. & Bean, C. P. Counting and Sizing of Submicron Particles by the Resistive Pulse Technique. *Review of Scientific Instruments* **41**, 909-916, doi:doi:http://dx.doi.org/10.1063/1.1684724 (1970).

45 Karhanek, M., Kemp, J. T., Pourmand, N., Davis, R. W. & Webb, C. D. Single DNA Molecule Detection Using Nanopipettes and Nanoparticles. *Nano Letters* **5**, 403-407, doi:10.1021/nl0480464 (2005).

46 Fu, Y., Tokuhisa, H. & Baker, L. A. Nanopore DNA sensors based on dendrimer-modified nanopipettes. *Chemical Communications*, 4877-4879, doi:10.1039/b910511e (2009).

47 Wang, Y., Cai, H. & Mirkin, M. V. Delivery of Single Nanoparticles from Nanopipettes under Resistive-Pulse Control. *ChemElectroChem* **2**, 343-347, doi:10.1002/celc.201402328 (2015).

48 Ivanov, A. P. *et al.* On-Demand Delivery of Single DNA Molecules Using Nanopipets. *ACS Nano* **9**, 3587-3595, doi:10.1021/acsnano.5b00911 (2015).

49 Actis, P. *et al.* Compartmental Genomics in Living Cells Revealed by Single-Cell Nanobiopsy. *ACS Nano* **8**, 546-553, doi:10.1021/nn405097u (2014).

50 McKelvey, K., Kinnear, S. L., Perry, D., Momotenko, D. & Unwin, P. R. Surface Charge Mapping with a Nanopipette. *Journal of the American Chemical Society* **136**, 13735-13744, doi:10.1021/ja506139u (2014).

51 Zhou, M., Yu, Y., Hu, K. & Mirkin, M. V. Nanoelectrochemical Approach To Detecting Short-Lived Intermediates of Electrocatalytic Oxygen Reduction. *Journal of the American Chemical Society* **137**, 6517-6523, doi:10.1021/ja512482n (2015).

52 Li, T., He, X., Yu, P. & Mao, L. A Bioinspired Light-Controlled Ionic Switch Based on Nanopipettes. *Electroanalysis* **27**, 879-883, doi:10.1002/elan.201400661 (2015).

53 Kim, S. J., Ko, S. H., Kang, K. H. & Han, J. Direct seawater desalination by ion concentration polarization. *Nat Nano* **5**, 297-301, doi:10.1038/nnano.2010.34 (2010).

54 Persson, F. & Tegenfeldt, J. O. DNA in nanochannels-directly visualizing genomic information. *Chemical Society Reviews* **39**, 985-999, doi:10.1039/b912918a (2010).

55 Ying, L. *et al.* The scanned nanopipette: a new tool for high resolution bioimaging and controlled deposition of biomolecules. *Physical Chemistry Chemical Physics* **7**, 2859-2866, doi:10.1039/b506743j (2005).

56 Brown, S. Nanobiopsy: Interrogating single cells. *Nat Nano*, doi:10.1038/nnano.2013.307 (2014).

57 Dung, D., Nghia, H., Veiko, V. P., Golubok, A. O. & Yakovlev, E. B. in *The Third International Conference on the Development of Biomedical Engineering in Vietnam* Vol. 27 *IFMBE Proceedings* (eds Vo Van Toi & TruongQuangDang Khoa) Ch. 31, 127-129 (Springer Berlin Heidelberg, 2010).

58 Haywood, D. G., Saha-Shah, A., Baker, L. A. & Jacobson, S. C. Fundamental Studies of Nanofluidics: Nanopores, Nanochannels, and Nanopipets. *Analytical Chemistry* **87**, 172-187, doi:10.1021/ac504180h (2015).

59 White, H. S. & Bund, A. Ion Current Rectification at Nanopores in Glass Membranes. *Langmuir* **24**, 2212-2218 (2008).

60 Wang, J., Zhang, M., Zhai, J. & Jiang, L. Theoretical simulation of the ion current rectification (ICR) in nano-pores based on the Poisson-Nernst-Planck (PNP) model. *Physical Chemistry Chemical Physics* **16**, 23-32, doi:10.1039/c3cp51712h (2014).

61 Luo, L., Holden, D. A. & White, H. S. Negative Differential Electrolyte Resistance in a Solid-State Nanopore Resulting from Electroosmotic Flow Bistability. *ACS Nano* **8**, 3023-3030, doi:10.1021/nn500379j (2014).

62 Li, Y. *et al.* History-dependent ion transport through conical nanopipettes and the implications in energy conversion dynamics at nanoscale interfaces. *Chemical Science* **6**, 588-595, doi:10.1039/c4sc02195a (2015).

63 Bard, A. J. & Faulkner, L. R. *Electrochemical methods : fundamentals and applications*. 2nd edn, (Wiley, 2001).

64 Oja, S. M., Wood, M. & Zhang, B. Nanoscale Electrochemistry. *Anal. Chem.* **85**, 473-486, doi:10.1021/ac3031702 (2013).

65 Schoch, R. B., Han, J. & Renaud, P. Transport phenomena in nanofluidics. *Rev. Mod. Phys.* **80**, 839 (2008).

66 Guo, W. *et al.* Energy Harvesting with Single-Ion-Selective Nanopores: A Concentration-Gradient-Driven Nanofluidic Power Source. *Adv. Funct. Mater.* **20**, 1339-1344, doi:10.1002/adfm.200902312 (2010).

67 Long, J. W., Dunn, B., Rolison, D. R. & White, H. S. Three-Dimensional Battery Architectures. *Chem. Rev.* **104**, 4463-4492, doi:10.1021/cr020740l (2004).

68 Logan, B. E. & Elimelech, M. Membrane-based processes for sustainable power generation using water. *Nature* **488**, 313-319, doi:Doi 10.1038/Nature11477 (2012).

69 Clarke, J. *et al.* Continuous base identification for single-molecule nanopore DNA sequencing. *Nat Nanotechnol* **4**, 265-270, doi:nnano.2009.12 [pii]

10.1038/nnano.2009.12 [doi] (2009).
70 Zwolak, M. & Di Ventra, M. Colloquium: Physical approaches to DNA sequencing and detection. *Rev. Mod. Phys.* **80**, 141-165, doi:10.1103/RevModPhys.80.141 (2008).
71 Branton, D. *et al.* The potential and challenges of nanopore sequencing. *Nat Biotechnol* **26**, 1146-1153, doi:nbt.1495 [pii]
10.1038/nbt.1495 [doi] (2008).
72 Van Driessche, A. E. S. *et al.* The Role and Implications of Bassanite as a Stable Precursor Phase to Gypsum Precipitation. *Science* **336**, 69-72, doi:10.1126/science.1215648 (2012).
73 Dekker, C. Solid-state nanopores. *Nat. Nanotechnol.* **2**, 209-215, doi:10.1038/nnano.2007.27 (2007).
74 Martin, C. R. & Siwy, Z. S. Learning nature's way: Biosensing with synthetic nanopores. *Science* **317**, 331-332, doi:10.1126/science.1146126 (2007).
75 Siwy, Z. S. & Howorka, S. Engineered voltage-responsive nanopores. *Chemical Society Reviews* **39**, 1115-1132, doi:10.1039/b909105j (2010).
76 Daiguji, H. Ion transport in nanofluidic channels. *Chem Soc Rev* **39**, 901-911, doi:10.1039/b820556f [doi] (2010).
77 Krems, M., Pershin, Y. V. & Di Ventra, M. Ionic Memcapacitive Effects in Nanopores. *Nano Lett.* **10**, 2674-2678, doi:10.1021/nl1014734 (2010).
78 Guerrette, J. P. & Zhang, B. Scan-Rate-Dependent Current Rectification of Cone-Shaped Silica Nanopores in Quartz Nanopipettes. *J. Am. Chem. Soc.* **132**, 17088-17091, doi:10.1021/ja1086497 (2010).
79 Momotenko, D. & Girault, H. H. Scan-Rate-Dependent Ion Current Rectification and Rectification Inversion in Charged Conical Nanopores. *J. Am. Chem. Soc.* **133**, 14496-14499, doi:10.1021/ja2048368 (2011).
80 Zhang, H. *et al.* Bioinspired Artificial Single Ion Pump. *J. Am. Chem. Soc.*, doi:10.1021/ja4037669 (2013).
81 Cervera, J., Ramirez, P., Mafe, S. & Stroeve, P. Asymmetric nanopore rectification for ion pumping, electrical power generation, and information processing applications. *Electrochim Acta* **56**, 4504-4511, doi:DOI 10.1016/j.electacta.2011.02.056 (2011).
82 Guo, W., Tian, Y. & Jiang, L. Asymmetric Ion Transport through Ion-Channel-Mimetic Solid-State Nanopores. *Acc Chem Res*, doi:10.1021/ar400024p (2013).
83 Siria, A. *et al.* Giant osmotic energy conversion measured in a single transmembrane boron nitride nanotube. *Nature* **494**, 455-458, doi:http://www.nature.com/nature/journal/v494/n7438/abs/nature11876.html#supplementary-information (2013).
84 Yusko, E. C., An, R. & Mayer, M. Electroosmotic flow can generate ion current rectification in nano- and micropores. *ACS Nano* **4**, 477-487, doi:10.1021/nn9013438 [doi] (2010).
85 Siwy, Z., Kosińska, I. D., Fuliński, A. & Martin, C. R. Asymmetric Diffusion through Synthetic Nanopores. *Physical Review Letters* **94**, 048102 (2005).
86 Kim, D.-K., Duan, C., Chen, Y.-F. & Majumdar, A. Power generation from concentration gradient by reverse electrodialysis in ion-selective nanochannels.

Microfluidics and Nanofluidics **9**, 1215-1224, doi:10.1007/s10404-010-0641-0 (2010).

87 Guan, W. & Reed, M. A. Electric Field Modulation of the Membrane Potential in Solid-State Ion Channels. *Nano Lett.* **12**, 6441-6447, doi:10.1021/nl303820a (2012).

88 van der Heyden, F. H. J., Bonthuis, D. J., Stein, D., Meyer, C. & Dekker, C. Electrokinetic Energy Conversion Efficiency in Nanofluidic Channels. *Nano Lett.* **6**, 2232-2237, doi:10.1021/nl061524l (2006).

89 Kubeil, C. & Bund, A. The Role of Nanopore Geometry for the Rectification of Ionic Currents. *J. Phys. Chem. C* **115**, 7866-7873, doi:10.1021/jp111377h (2011).

90 Woermann, D. Electrochemical transport properties of a cone-shaped nanopore: high and low electrical conductivity states depending on the sign of an applied electrical potential difference. *PCCP* **5**, 1853-1858 (2003).

91 Siwy, Z. & Fulinski, A. Fabrication of a synthetic nanopore ion pump. *Phys. Rev. Lett.* **89**, doi:10.1103/PhysRevLett.89.198103 (2002).

92 Wang, D. *et al.* Physical origin of dynamic ion transport features through single conical nanopores at different bias frequencies. *Chemical Science* **DOI: 10.1039/C3SC52187G**, doi:10.1039/c3sc52187g (2014).

93 Jorne, J. Transference Number Approaching Unity in Nanocomposite Electrolytes. *Nano Lett.* **6**, 2973-2976, doi:10.1021/nl062182m (2006).

94 Liu, J. *et al.* Surface charge density determination of single conical nanopores based on normalized ion current rectification. *Langmuir* **28**, 1588-1595, doi:10.1021/la203106w (2012).

95 Cervera, J., Schiedt, B., Neumann, R., Mafe, S. & Ramirez, P. Ionic conduction, rectification, and selectivity in single conical nanopores. *J. Chem. Phys.* **124**, 104706 (2006).

96 Siria, A. *et al.* Giant osmotic energy conversion measured in a single transmembrane boron nitride nanotube. *Nature* **494**, 455-458, doi:10.1038/nature11876 (2013).

97 BERNAL, J. & CROWFOOT, D. X-Ray Photographs of Crystalline Pepsin. *Nature* **133**, doi:10.1038/133794b0 (1934).

98 Hansen, C. L., Skordalakes, E., Berger, J. M. & Quake, S. R. A robust and scalable microfluidic metering method that allows protein crystal growth by free interface diffusion. *Proceedings of the National Academy of Sciences* **99**, 16531-16536, doi:10.1073/pnas.262485199 (2002).

99 Chen, D. L. & Ismagilov, R. F. Microfluidic cartridges preloaded with nanoliter plugs of reagents: an alternative to 96-well plates for screening. *Current Opinion in Chemical Biology* **10**, 226-231, doi:http://dx.doi.org/10.1016/j.cbpa.2006.04.004 (2006).

100 Zheng, B., Gerdts, C. J. & Ismagilov, R. F. Using nanoliter plugs in microfluidics to facilitate and understand protein crystallization. *Current Opinion in Structural Biology* **15**, 548-555, doi:http://dx.doi.org/10.1016/j.sbi.2005.08.009 (2005).

101 Hong, J., Edel, J. B. & deMello, A. J. Micro- and nanofluidic systems for high-throughput biological screening. *Drug Discovery Today* **14**, 134-146, doi:http://dx.doi.org/10.1016/j.drudis.2008.10.001 (2009).

102 Zhu, Y. *et al.* Nanoliter-Scale Protein Crystallization and Screening with a Microfluidic Droplet Robot. *Sci. Rep.* **4**, doi:10.1038/srep05046
http://www.nature.com/srep/2014/140523/srep05046/abs/srep05046.html#supplementary-information (2014).
103 Asherie, N. Protein crystallization and phase diagrams. *Methods* **34**, 266-272, doi:http://dx.doi.org/10.1016/j.ymeth.2004.03.028 (2004).
104 Ielasi, F. S. *et al.* Dip-Pen Nanolithography-Assisted Protein Crystallization. *Journal of the American Chemical Society* **137**, 154-157, doi:10.1021/ja512141k (2015).
105 Khurshid, S., Govada, L., El-Sharif, H. F., Reddy, S. M. & Chayen, N. E. Automating the application of smart materials for protein crystallization. *Acta Crystallographica Section D: Biological Crystallography* **71**, 534-540, doi:10.1107/s1399004714027643 (2015).
106 Liu W, W. D., Wang C, Abola E, Cherezov V. Femtosecond crystallography of membrane proteins in the lipidic cubic phase. *e. Phil. Trans. R. Soc. B* **369** (2014).
107 Landau, E. M. & Rosenbusch, J. P. Lipidic cubic phases: A novel concept for the crystallization of membrane proteins. *Proceedings of the National Academy of Sciences* **93**, 14532-14535 (1996).
108 Khurshid, S., Saridakis, E., Govada, L. & Chayen, N. E. Porous nucleating agents for protein crystallization. *Nat. Protocols* **9**, 1621-1633, doi:10.1038/nprot.2014.109
http://www.nature.com/nprot/journal/v9/n7/abs/nprot.2014.109.html#supplementary-information (2014).
109 Chapman, H. N. Femtosecond X-ray protein nanocrystallography. *Nature* **470**, 73-77 (2011).
110 Johansson, L. C. Lipidic phase membrane protein serial femtosecond crystallography. *Nature Methods* **9**, 263-265 (2012).
111 Barends, T. R. M. *et al.* De novo protein crystal structure determination from X-ray free-electron laser data. *Nature* **505**, 244-247, doi:10.1038/nature12773
http://www.nature.com/nature/journal/v505/n7482/abs/nature12773.html#supplementary-information (2014).
112 Kern, J. Room temperature femtosecond X-ray diffraction of photosystem II microcrystals. *Proc. Natl Acad. Sci. USA* **109**, 9721-9726 (2012).
113 Wakamatsu, T. Method and apparatus for characterization of electric field-induced aggregation in pre-crystalline protein solutions. *Review of Scientific Instruments* **86**, 015112, doi:doi:http://dx.doi.org/10.1063/1.4906328 (2015).
114 Nanev, C. N. & Penkova, A. Nucleation and growth of lysozyme crystals under external electric field. *Colloids and Surfaces A: Physicochemical and Engineering Aspects* **209**, 139-145, doi:http://dx.doi.org/10.1016/S0927-7757(02)00175-9 (2002).
115 Taleb, M. *et al.* Crystallization of proteins under an external electric field. *Journal of Crystal Growth* **200**, 575-582, doi:http://dx.doi.org/10.1016/S0022-0248(98)01409-2 (1999).
116 Nieto-Mendoza, E., Frontana-Uribe, B. A., Sazaki, G. & Moreno, A. Investigations on electromigration phenomena for protein crystallization using crystal growth cells with multiple electrodes: effect of the potential control.

Journal of Crystal Growth **275**, e1437-e1446, doi:http://dx.doi.org/10.1016/j.jcrysgro.2004.11.233 (2005).

117 Hou, D. & Chang, H.-C. ac field enhanced protein crystallization. *Applied Physics Letters* **92**, 223902, doi:doi:http://dx.doi.org/10.1063/1.2938887 (2008).

118 Gil-Alvaradejo, G. *et al.* Novel Protein Crystal Growth Electrochemical Cell For Applications In X-ray Diffraction and Atomic Force Microscopy. *Crystal Growth & Design* **11**, 3917-3922, doi:10.1021/cg200485v (2011).

119 Yin, D.-C. Protein crystallization in a magnetic field. *Progress in Crystal Growth and Characterization of Materials* **61**, 1-26, doi:http://dx.doi.org/10.1016/j.pcrysgrow.2015.03.001 (2015).

120 Kakinouchi, K. *et al.* Effect of ultrasonic irradiation on protein crystallization. *Journal of Crystal Growth* **292**, 437-440, doi:http://dx.doi.org/10.1016/j.jcrysgro.2006.04.051 (2006).

121 Sazaki, G. Crystal quality enhancement by magnetic fields. *Progress in Biophysics and Molecular Biology* **101**, 45-55, doi:http://dx.doi.org/10.1016/j.pbiomolbio.2009.12.003 (2009).

122 Sazaki, G., Moreno, A. & Nakajima, K. Novel coupling effects of the magnetic and electric fields on protein crystallization. *Journal of Crystal Growth* **262**, 499-502, doi:http://dx.doi.org/10.1016/j.jcrysgro.2003.09.050 (2004).

123 Nanev, C. N. & Penkova, A. Nucleation of lysozyme crystals under external electric and ultrasonic fields. *Journal of Crystal Growth* **232**, 285-293, doi:http://dx.doi.org/10.1016/S0022-0248(01)01169-1 (2001).